Preparation and characterisation of ceramic and thin film Zn(_2)SnO(_4)

Abdulaziz A.SH. Al-Shahrani

PREPARATION AND CHARACTERISATION OF CERAMIC AND THIN FILM Zn_2SnO_4

by

ABDULAZIZ A. SH. AL-SHAHRANI, BSc., MSc.

Presented in Candidature for the Degree of
Doctor of Philosophy in the
UNIVERSITY OF DURHAM

OCTOBER 1993

In the name of Allah, the Beneficent, the Merciful.

To my family

ABSTRACT

Ceramic zinc stannate, Zn_2SnO_4, was prepared from $1SnO_2$:2ZnO mixture using powders of the highest commercially available purity. The solid state reaction between the ZnO and the SnO_2, thought to be an evaporation-recondensation mechanism, was found to start at $\sim$ 900°C (12 hours heating, rate 5°C min^{-1}). However, the reaction did not go to completion in the timescale of the experiment unless the temperature was raised to$\sim$1300°C. In this case mono-phase, polycrystalline Zn_2SnO_4 was produced, as confirmed by X-ray diffraction (XRD), scanning electron microscopy and energy dispersive X-ray analysis (EDAX). Further evidence for these reaction temperatures was obtained from thermal analysis experiments.

As-sintered, Zn_2SnO_4 was insulating ($\sigma \sim 10^{-9}\ \Omega^{-1}\ cm^{-1}$) although it could be made conductive, by a reduction heat-treatment. This entailed refiring the sintered pellets of Zn_2SnO_4 in an atmosphere of mixture gas (25% H_2 + 75% N_2) at $\sim$ 450°C for 14 hours (heating rate of 10°C min^{-1}). This reduced the conductivity to values of $\sigma \sim 1 \times 10^{-2}\ \Omega^{-1}\ cm^{-1}$. XRD failed to reveal any changes in the phase of the material after the reduction treatment.

Several dopants were investigated, the most successful of which was In, using a vapour phase method. Doping with In this way gave a significant change in the colour from white to dark grey together with a reduction in electrical resistivity, without recourse to further heating treatments. No change in the usual phase of the Zn_2SnO_4 was detected. Doping with group V oxides, such as Nb_2O_5, V_2O_5 etc, produced changes in the colour from white to dark grey, but no reduction in the resistivity, unless further heating treatments were carried out in reducing ambients. When high concentrations of Nb were introduced an additional phase, possibly $Nb_2Sn_2O_7$ was observed by XRD.

Thin film Zn_2SnO_4 was prepared by Electron Beam Evaporation using Zn_2SnO_4 sintered powder as the evaporant material. The thin films were deposited onto glass substrates, at a range of substrate temperatures between room temperature and 250°C. XRD was used to confirm the formation of Zn_2SnO_4, and provide estimates for the grain size, which varied from 20 to 25 nm. RHEED studies indicated that the grain size increased as the substrate temperature was increased. SEM revealed that the thin films were flat and uniform, with no cracks. The optical transmission of the thin films was about 88% for films deposited at 200°C, but decreased significantly as the substrate temperature was decreased. The spectral dependence of complex refractive index (n&k) suggested that true thin film formation did not take place until the substrate temperature exceeded $\sim$ 150°C, and that the material was apparently a direct gap semiconductor with a band gap energy of $\sim$1.95 eV.

It was found that the main carrier transportation mechanism for doped, un-doped, and thin films of Zn_2SnO_4 was variable range hopping, with a temperature dependence of the form $\exp(To/T)^{1/4}$. This result was consistent with Hall effect measurements, where high, temperature independent carrier concentrations of about $10^{17}\ cm^{-3}$ were obtained, along with low values of carrier mobility ($\sim$ 1 $cm^2\ v^{-1}\ sec^{-1}$) that obeyed the same temperature dependence as the conductivity, $[\exp(To/T)^{1/4}]$.

DECLARATION

I declare that the work reported in this thesis, unless otherwise stated, was carried out by the candidate, that it has not previously been submitted for any degree and it is not currently being submitted for any other degree.

Dr. A. W. Brinkman
Supervisor

Abdulaziz Al-Shahrani
Candidate

ACKNOWLEDGEMENTS

I would like to take this opportunity to thank the many people who have helped in the production of this thesis, especially my supervisor, Dr. A. W. Brinkman, to whom I wish to express my appreciation and gratitude for the valuable guidance and helpful encouragement.

I am also indebted to Dr. T. Hashemi for many constructive discussions and suggestions. I would also like to thank Dr. K. Durose for his instruction and help in the RHEED study, Mr R Hardy for his help in the XRD study, Dr. John Lewis for his help in the photospectroscopy study, and Dr. H M Al-Allak for his many useful discussions. I would also like to express appreciation to Elmwood Sensors Ltd. and Netzsch Mastermix Ltd. for carrying out the thermal analysis.

One must also remember with sadness the support and suggestions given to all of us in the II-VI semiconductors and Ceramics group by the late Professor J Woods, whose sudden death was a great loss to science.

I wish to extend my thanks to the technical staff of the department, especially to Mr N.F. Thompson for his friendly and technical support, and to all members of the Engineering workshop, and of the computer centre and the library staff, who were at all times helpful and supportive.

I would like, also, to express my appreciation to the Saudi Arabian Educational Attache and King Saud University, for an award of a research studentship and for providing financial support over my research period. Special thanks should go to Mr. Abdullah Al-Nasir, The Saudi Arabian Attache in the U.K., for his friendly encouragement for me and all Saudi students in U.K..

On a more personal note I wish to express my gratitude to my parents for their many sacrifices and constant encouragement over the years, and to my brothers and friends for their support and kindness. Finally, special thanks go to my wife, for her understanding, patience, kindness and support during our time in Durham.

TABLE OF CONTENTS

CHAPTER I
INTRODUCTION

1.1 - Introduction :

Polycrystalline ceramics are compounds of electropositive and electronegative elements of the periodic table. Most ceramics are oxides, and are essentially different from metals and organic compounds in their chemical bonding, and as a result in their physical and chemical properties.

In the present context a ceramic material will be taken to be one composed of a compact of small particles that have been sintered together, usually at high temperature. Under such conditions the individual particles "grow" into each other forming a very strong structure. For a given group of elements, there are frequently numerous configurations that will form a ceramic, and accordingly an equally wide variety of resulting material properties. Nevertheless, there are some common features of ceramic materials, and these are : (i) tolerance to high temperatures, (ii) low or semiconducting electrical conductivity with often magnetic and dielectric properties, and (iii) considerable strength giving a high resistance to deformation or fracture. These properties are sometimes advantageous and sometimes not.

1.2 - Traditional Ceramics :

Traditionally ceramics are associated primarily with clay products, silicate glasses, and cement. Pottery using clay has been practised both as an art form and as a craft for the manufacture of household utensils from the earliest civilizations. The high stability of ceramic materials has meant that such artefacts survive for many centuries and provide important material for the archaeologist. Similarly, silicate glass manufacturing is an equally ancient art.

Generally most of these traditional ceramics were produced without concern for, or much understanding of, the mineral preparation of the ceramic and related raw materials. These ceramics could be adequately defined as silicate compounds, a

description originally proposed for the American Ceramic Society in 1899 [1.1].

1.3 - New Ceramics and Their Applications :

The term, new ceramic or fine ceramic, began to appear during the last 20 years and is typically applied to specialist ceramics synthesized using highly refined starting materials, with rigorously controlled composition, and strictly regulated forming and sintering conditions[1.2]. They are of particular interest due to their unique or outstanding properties, and have been developed in order to fulfil a particular need, such as for example, greater resistance to temperature, improved mechanical properties, special electrical properties, etc [1.3-1.9]. These ceramics have become most important for future high technology industry [1.10,1.11].

The *new* or *fine* ceramics are generally divided into two categories; *structural* ceramics and *functional* ceramics. The former are of interest primarily for their good mechanical properties, particularly at high temperature, and generally compose the nitrides, carbides, borides and silicides of metals. For example the structural ceramic sialon (SiAlN) was developed for use in mechanical bearings. The functional ceramics are of interest principally for their electrical, magnetic and optical properties and are composed mainly of the metal oxides. A summary of the areas in which functional ceramics have found application is given in table (1.1)

The present study has been concerned exclusively with the functional ceramic, zinc stannate (Zn_2SnO_4). This compound, which has not been greatly researched before, has interesting electrical properties and potential applications for battery, relay contacts and thin film electrochromic displays.

Table (1.1) : Electronic ceramics function, uses, and representative materials.

Function	Application		Materials
Insulation	IC Substrates		Al_2O_3, $MgAl_2O_4$, BeO
Electric Conductivity	Resistive Heat Generators		ZrO_2, $MoSi_2$, $LaCrO_3$, SiC, Zr Hf-borides
	Solar Electric Generators		
	Electrode		
Piezoelectro--nics	Ignition junction	Automatic lighter	$Pb(Zr, Ti)O_3$
	Piezoelectric Filters	FM/TV	ZnO, $LiNbO_3$
	Surface wave devices		
	Piezoelectric oscillators	Clocks	Quartz, $LiNbO_3$
Semiconduc--tivity	Thermistor	Thermometers	Fe-Co-Mn, Si-O, $BaTiO_3$
	Wireless Semiconduct.	Varistor	ZnO-Bi_2O_3, SiC
	Gas-Absorbing Semiconductor.	Gas-Sensor	SnO_2, ZnO, Zn_2SnO_4
Magnetism	Hard Magnets	Ferrite Magnets	(Ba, Sr) 0.6 Fe_2O_3
	Soft Magnets	Transformers	(Zn, M) Fe_2O_4(M=Mn, Co, Ni)
		Memory junction	Garnet-type Ferrites
Inductance	Low Frequency use	Capacitance	$BaTiO_3$+SnO_2+Bi_2O_3
Ionic Electric Conduction	Batteries		β-Al_2O_3, ZrO_2 (+CaO, Y_2O_3)

1.4 - Zn_2SnO_4 Properties and Applications :

Zinc stannate [1.12], Zn_2SnO_4, may be formed by firing a mixture of SnO_2 and ZnO, with molar ratio of 1:2 [1.13] at a high temperature for a several hours. It is white in colour, but turns dark grey when heated in a reducing ambient. It is an n-type semiconductor [1.15], and normally crystallines in the inverse spinel structure (more detail can be found in chapter III) [1.16], with a lattice parameter a = 8.65 Å [1.4,1.6,1.7,1.11]. Some of the reported or proposed applications of Zn_2SnO_4 are listed in table (1.2).

Table (1.2) : Some Zn_2SnO_4 Applications.

Application	Additives	Year	Reference
Moisture Detector	None	1977, 1980	[14],[15]
Stable Gas Sensor	Al, Cr, Y	1984	[16]
Electrical Contacts	Ag	1983	[17]
Switching Gear	Ag	1991	[5]
Gas Sensor(H, Ch_4,H_2O)	None	1987	[20]
Trans. Electrode	None	1992	[25]

The first reference to Zn_2SnO_4 was in 1930 by Nelson Taylor who reported that Zn_2SnO_4 can be prepared by heating a mixture of $2ZnO:1SnO_2$ [1.17], at 1050°C for 18 hours. The compound formed was of cubic spinel type with lattice constant of a = 8.65 ± .005 Å . This was confirmed by Barth and Posnjak (1932) [1.19] and later by Verweg and Heilmann (1947) [1.20] who reported that Zn_2SnO_4 had the arrangement $Zn_8(Sn_8Zn_8)O_{32}$, a cubic spinel structure type with a large unit cell containing 8Sn, 16Zn, and 32 Oxygen atoms. Independently Frevel (1942) [1.21] measured the lattice constants of 705 cubic substances including Zn_2SnO_4 , using chemical analysis by the Debye-Scherrer-Hull method, and reported a lattice constant

of 8.63 Å for Zn_2SnO_4.

Further research by Tazaki and Kuwabara (1951) [1.18] led to the conclusion that Zn_2SnO_4 could not be obtained at a temperature lower than 900°C with a heating time of about 60 min. (using atmospheric pressure), and also found the structure type was cubic spinel.

An alternative procedure for forming Zn_2SnO_4 was reported by Kostolov and Morechevskaya (1958) [1.22] who found that Zn_2SnO_4 could be formed by mixing Zinc oxide with tin oxide in a proportion corresponding to the formula $ZnO:SnO_2$, and then holding the mixture of the two oxides at a temperature of $800°C < T < 1300°C$ for 5-20 min.. They also concluded that zinc oxide began to interact with tin oxide above 800°C and confirmed the resulting compound by X-ray analysis. However, Fillipova et al (1960) concluded that Zn_2SnO_4 was best formed using the 2:1 ratio of $ZnO:SnO_2$, at a temperature of 1200°C for 8 hours. They also found the structure to be cubic spinel with lattice parameter of 8.64 Å,

More recently, Gupta and Mathur (1968) [1.23], have prepared Zn_2SnO_4 by mixing $2ZnO:1SnO_2$, and then heating at 900°C for 50 hours and again at 1100°C for 40 hours . From this it was clear that the compound would not form unless $T >$ 1000°C. Yoshida R and Yoshida Y (1976) [1.24], also reported that a suitable temperature for forming Zn_2SnO_4 was about 1200°C and used X-ray diffractometry to confirm the compound, and obtained an estimate for the lattice constant of between $a = 8.67$ to 8.68 Å. Zuyao (1987) [1.15], formed zinc stannate by a solid state reaction at 800°C, and it was found that the compound was cubic spinel type. A higher temperature of 1300°C was used by Shimada (1976) [1.25] to prepare zinc stannate by calcining a stoichiometric mixture of zinc oxide and tin oxide at a more rapid rate for only 4 hours. Interestingly Huang (1984) [1.26], reported that zinc stannate was formed in the reverberator furnace dust recovered from a tin smelting process. The formation of Zn_2SnO_4 from ZnO and SnO_2 was observed at a temperature higher than 1000°C, with a yield that increased rapidly with increasing reaction temperature. They

discovered that the SiO_2 tended to lower the yield of Zn_2SnO_4 because it combined with ZnO preferentially.

Another method for preparing Zn_2SnO_4 was described by William Pickin (1986) in a UK Patent application [1.27] , which showed that Zn_2SnO_4 films could be formed from $ZnCl_2$ and $SnCl_2$ in roughly equal proportions using flame deposition. This was further investigated by Fujita (1987) [1.28] who prepared zinc stannate by using $SnCl_4$, $ZnCl_2$, and $(CH_2)_6N_4$, at a temperature of about 700°C, to produce a mixture of ZnO, SnO_2, and Zn_2SnO_4. The presence of several phases may have been due to the relatively low temperature of sintering (as described above, other studies have suggested that the sintering temperature should be more than 1000°C to form compound by the solid state reaction). Another route to forming the compound was found by Wark et al. (1990) [1.29], and involved the metal alkoxide $[ZnSn(OEt)_6]$. Hydrolytic condensation of this compound formed an as yet unidentified crystalline phase together with amorphous material . Heating resulted in the crystallization of Zn_2SnO_4 and SnO_2. A temperature of 600°C was used. Yet another procedure was reported by Glot et al. (1991) [1.30]. They obtained semiconducting SnO_2 and dielectric Zn_2SnO_4 as a result of mixing SnO_2-ZnO-Bi_2O_3 together in a molar ratio of 80 mol.% SnO_2, 20 mol.% ZnO and 2 wt.% Bi_2O_3, and sintering at 1520°C. Hashemi et al (1990) [1.14], have reported more detail about the sintering behaviour of zinc stannate. Using **XRD** they found that zinc stannate was monophase and polycrystalline . A detailed study of morphology and surface composition suggested that the diffusion - evaporation mechanism was responsible for SnO_2 / ZnO sintering

The first reported application of Zn_2SnO_4 was by Terada and Nitta (1977) [1.31], (1980) [1.30] , who used Zn_2SnO_4 as a detector of moisture. Another application was demonstrated by Sumitomo Aluminum Smelting Co. (1984) [1.33] , where a stable combustible - gas sensor was obtained by heating a $SnZn_2O_4$-M_2O_3 (M = Al, Cr, Y) mixture at 600°C to 1400°C. Xinghui (1987) [1.34] also reported that Zn_2SnO_4 was obtained by sintering $Zn[Sn(OH)_6]$ between 500°C - 800°C. They used

it as a semiconducting gas sensing material for detecting H_2, CH_4, and water.

Zn_2SnO_4 was also used as electrical contacts by mixing it with silver as shown in a Patent by Sumitomo Electric Industries (1983) [1.35], and in the paper by Illingsworth J , Hashemi T , Al-Shahrani A and Brinkman A W, (1991) [1.36].

Apart from Pickin [1.27], the only other thin film study was that reported by Enoki H. et al. (1992) [1.37], who formed Zn_2SnO_4 as a thin film using **RF** magnetron sputtering. where the deposited films showed a spinel type with a different crystal structure of hexagonal ZnO. The Zn_2SnO_4 films showed more than 80% transmission over the visible range with a lower wavelength absorption edge of less than 320 nm.

From these reports and results, it appears that Zn_2SnO_4 can be readily formed by a solid state reaction if the temperature T > 1000°C. **XRD** results indicate that this gives monophase, cubic spinel type material.

1.5 - Present Work Aims :

The aim of this study was to assess the formation of Zn_2SnO_4 in bulk form and as thin films. Chapter II introduces the relevant scientific background in Ceramics sintering types and related phenomena. Chapter III outlines details of the experimental set-up used for sintering and reduction processes.

The experimental results obtained during the last three years of this study are presented in chapters IV to VII; chapter IV describing the sintering and reduction processes, a structural study is also included in this chapter, as well as the thermal studies, which were used to support the description of the sintering mechanism. Chapter V details the electrical properties of the un-doped samples, in particular the variation of resistivity and polarity type as a result of changing the reduction temperature. Impedance studies have been included in this chapter using a.c. measurements to give some information about bulk and grain boundary behaviour. Current-Voltage measurements were made using pulsed voltages for bulk samples to test the contacts for ohmic behaviour. Chapter VI concerns structural, and d.c. and

a.c. electrical studies of doped-Zn_2SnO_4 samples. These were doped in various ways with different materials, including Nb_2O_5, Ta_2O_5, $TaCl_5$, $InCl_3.3H_2O$, and In. Diodes based on $Au/Zn_2SnO_4.In/In.Ga$ structures were also prepared and the I-V and C-V characteristics obtained and analyzed. Chapter VII discusses Zn_2SnO_4-thin film formation, and outlines the optimum preparation conditions. Structural electrical and optical transmission characteristics of the thin films were measured and are included.

Chapter VIII concludes and summarises the experimental findings indicting the major objectives achieved whilst providing suggestions for future work in the field of Zn_2SnO_4 ceramics.

1.6 - References

[1.1] - Kingery W.D., Bowen H.K., Uhlmann D.R."Introduction. To Ceramics", John Wiley & Sons, (1976).

[1.2] - Noboru I. (Ed.), "Introtuction To Fine Ceramics", John Wiley & Sons,(1987).

[1.3] - Eddy D., IEEE Trans. **TV-23**, 125, (1974).

[1.4] - McGeehin P., Hooper A., J. Mater. Sci., **12**, 1-27, (1977).

[1.5] - Fog A, Buck R.P., Sensors and Actuators, **5**, 137, (1984).

[1.6] - Saburi O., J. Am. Ceram. Soc., **44**, 54-63, (1964).

[1.7] - Levinson L. M.(Ed.), "Electron Ceramics", New York: Marcel Dekker,(1988).

[1.8] - Herbert J.M., "Ferroelectric Transducer and Sensors.", Gordon and Breach, (1982).

[1.9] - Herbert J.M., "Ceramic Dielectrics and Capacitors", Gordon & Breach,(1985).

[1.10] - Newnham R.E., Rep. Prog. Phys., **52**, 123-156, (1989).

[1.11] - Moulson A.J., Herbert J.M., "Electroceramics", Chapman and Hall, (1990).

[1.12] - Poix P., Michel A., C.r. hebd. seanc Acad. Sci. Paris **225**, 2446, (1962).

[1.13] - Filippova N. A., Savina E. V., and Korosteleva V. A..Russian J. Inorganic Chemistry, Vol.**5**, No.7, 691 (1960).

[1.14] - Hashemi T., Al-Allak H.M., Illingsworth J., Brinkman A.W., and Woods J., J. Mater. Sci. Lett., **9**, 776, (1990).

[1.15] - Zuyao C., Ying J., Zude Z., and Yitai Q., J. China Univ. Science and Technology, Vol.**17**, No. 3, 343, (1987).

[1.16] - Wickham D.G., Dwight K., The Phys. Chem. Solid, 20, 316, (1961).

[1.17] - Tylor N. W., Z. Physikal. Chem., **9**, 241, (1930).

[1.18] - Tazaki H., and Kuwabara, J. Sci. Hiroshima Univ., **15**, 133, (1951).

[1.19] - Barth T. F. W., and Posnjak, Zeits f. Krist, **82**, 325, (1932).

[1.20] - Verwey E. J. W., and Heilmann E. L., J. Chem. Phys., Vol **15**, No 4, 174, (1947).

[1.21] - Frevel L. K., Industrial and Engineering Chemistry, Vol. **14**, No. 9, 687,

(1942).

[1.22] - Kostolov V. V., Morachevskaya V. S. and Gipronikel V. Nonferrous Metals, Vol.**31**, No.10, Moscow, 39 (1958).

[1.23] - Gupta M. P., and Mathur H. B., J. Phys. Chem. Solid, Vol. **29**, 1479, (1968).

[1.24] - Yoshida R., Yoshida Y., Yamal I., Kodaira K, and Matsushita T, J. Crytal Growth, **36**, 181, (1976).

[1.25] - Shimada S., Kodaira K, and Matsushita, Chem. Lett., 235 (1976).

[1.26] - Hung S., Sumita S., Morinaga K., and Ynagase T, Nippon Kogyo Kaishi, 100(1162), 1145,(1984).

[1.27] - Pickin W., UK Patent Application, **GB 2162861A**.

[1.28] - Fujita K., Kota K., Mitsuzawa S, Japan. Ceram. Soc. Assoc., **96** [1], 6,(1988).

[1.29] - Wark T. A., Gulliver E. A., Jones L. C., Hampden-Smith M. J., Rheingold A. I., and Huffman J. C., Mat. Res. Soc. Symp. Vol. **180**, 61, (1990).

[1.30] - Glot A. B., Proshkin Y. N., Nadzhafzade A. M., Ceramics today - Tomorrow's ceramic, Elsevier Science Publishers B. V., (1991).

[1.31] - Terada J., Nitta T., and Ise Y., Kokai Tokkyo Koho, **JP 80 51**, 345, (1980).

[1.32] - Nitta T., and Hayakawa S., Kokai Tokkyo Koho, **JP 77, 36**, 789, (1977).

[1.33] - Sumitomo Aluminum Smelting, Kokai Tokkyo Koho, **JP 59 54**, 954, (1984).

[1.34] - Xinghui, (Yannan Univ.), Shoumingshu CN 86, **106**, 681, (1987).

[1.35] - Sumitomo Electric Industries, Kokai Tokkyo Koho, **JP 83 35**, 71, (1983).

[1.36] - Illingsworth J., Hashemi T, Al-Shahrani A., and Brinkman A W., Brit. Ceram. proc. **49**, Special ceramics **9**, London, 241, (1990)

[1.37] - Enoki H. et al., Phys Stat. Sol. (a) **129**, 181 (1992).

CHAPTER II

SCIENTIFIC BACKGROUND

2.1 - Introduction :

Polycrystalline ceramics are materials in which neighbouring grains are in close intimate contact with each other, yielding structures that are durable and strong. The range of compounds that can be produced in ceramic form is enormous and as a result there is a correspondingly large variety of properties available for use. Ceramic materials cannot be easily obtained and high processing temperatures are normally required. When ceramic materials are formed from a mixture of constituent powders which are then fired, there is a certain temperature at which the raw materials begin to react, requiring a certain time to do so. In most cases this is accompanied by some shrinkage, resulting in densification, and sometimes this is associated with a colour change as well. This process is usually termed "sintering".

Ceramic processing, both for crystalline and non crystalline sintering is carried out by compacting precursor powder and then firing at a temperature sufficient to develop the desired useful properties. Denser structures will be produced when crystallites join to one another at the grain boundaries which then become intimate. Sometimes this may consist of a crystalline or vitreous second phase. This change happens as a result of decomposition or phase transfer [2.1]. High temperatures usually cause (a) a decrease in the porosity, (b) a change in the pore shape, and (c) an increase in the grain size.

A second phase is always present during ceramic sintering and in almost all ceramic products prepared by sintering. Residual porosity remains due to the interparticle spaces present in the initial powder compact.

Sintering processes can be divided into three broad categories, (i) solid state sintering, (ii) liquid phase sintering, and (iii) gas phase sintering. These cases may not be necessarily mutually exclusive, and usually two or more of them work together in most cases [2.2].

The sintering mechanism can be explained in terms of a model in which two equal spheres (grains) are altered by a transfer of material between them during the firing processes. This transfer can occur by diffusion, when the thermal energy causes a migration of atoms or ions from one sphere to the other via the lattice vacancies that exist in the material. The difference in densities of lattice vacancies, provides the driving force for material transfer, from the area of lower concentration to that of higher concentration. Where this occurs then the density of vacancies near the attachment line between the spheres becomes greater, creating a strong concentration gradient between the equilibrium areas.

The material transfer may take place via a number of different routes, and sintering processes can be classified accordingly. As an example :

(i) in the case of solid state sintering, the mechanisms are : (a) volume diffusion, (b) grain boundary diffusion , (c) surface diffusion, and (d) evaporation-condensation (discuss in detail in chapter IV);

(ii) in the case of liquid phase sintering, material transfer during the sintering process is facilitated by the intervention of a reactive liquid;

(iii) gas phase sintering is more commonly called chemical vapour deposition [2.2] and will be not discussed further here.

2.2 - Principles of Sintering :

2.2.1 - Solid State Sintering :

When sintering takes place by evaporation-condensation, the driving force that gives rise to densification is the free-energy change associated with a decrease in surface area and the consequent reduction in the surface free energy following the elimination of solid-vapour interfaces. This usually takes place with the coincidental formation of new, but lower-energy solid-solid interfaces. The net decrease in free energy occurring on sintering a 1-micron particle size material corresponds to an energy decrease of about 4.2 Joule g^{-1} [2.3]. The material transfer between grains is

affected by the pressure difference and changes in free energy across a curved surface [2.3].

Evaporation-condensation is not one of the more common mechanisms of material transformation in solid state reactions. During this sintering process material transfer takes place as a result of differences in surface curvature of the grains, and the consequent differences in the vapour partial pressure at various parts of the system. Evaporation-condensation sintering is the simplest process to treat quantitatively.

If this sintering process is the only dominant one in the system, then the distance between centres of spherical particles is not affected by the transfer of material from the particle surface to the interparticle neck, created between two neighbouring particles. This means that vapour-phase-material transfer does not affect shrinkage, because, although long heating may result in a considerable increase in interface contact area, the distance between particle centres remains essentially the same [2.3]. Clearly vapour-phase-material transfer requires a temperature sufficiently high for the vapour pressure to be appreciable [2.2], and for micron-sized particles, vapour pressures of the order of 10^{-4}-10^{-5} atmosphere are necessary for significant material transfer to occur by this mechanism.

The rate of increase of bonding area between particles (see figure (2.1)) can be calculated by equating the material transfer rate to the surface of the lens between the grains with the increase in its volume. According to the Thomson-Freundlich (Kelvin) equation [2.3], the vapour pressure over the small negative radius of curvature is decreased because of the surface energy as follows :

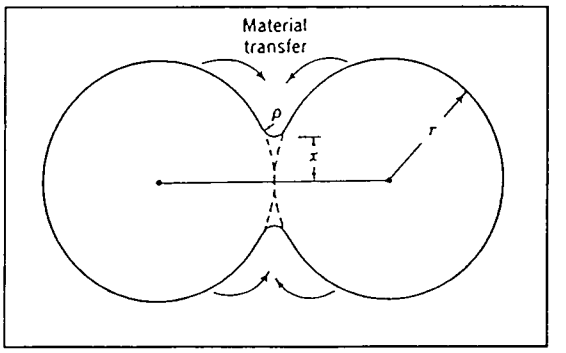

Figure (2.1) : Sintering by evaporisation - condensation [ref. 2].

$$\ln \frac{p_1}{p_o} = \frac{\gamma M}{dRT}\left(\frac{1}{\rho} + \frac{1}{x}\right) \qquad (2.1)$$

where p_1 is the vapour pressure over the small radius of curvature, γ is the surface or interfacial tension, M is the molecular weight of the vapour, and d is the density. In this case the neck radius (x) is much larger than the radius of curvature at the surface, ρ, and the pressure difference p_o-p_1 is small. Consequently, to a good approximation, $\ln\left(\frac{p_1}{p_o}\right)$ is equal to $\frac{\Delta p}{p_o}$, and we can write:

$$\Delta p = \frac{\gamma M p_o}{d\rho RT} \qquad (2.2)$$

where Δp is the difference between the vapour pressure above the region of small negative radius of curvature and the saturated vapour in equilibrium over the nearly flat particle surfaces. The rate of condensation is proportional to the difference in equilibrium and atmospheric vapour pressure and is given by the Langmuir equation to a good approximation as [2.3] :

$$\Delta m = \alpha \Delta p \left[\frac{M}{2\pi RT}\right]^{1/2} \quad g\ cm^{-2}\ s^{-1} \qquad (2.3)$$

where α is an accommodation coefficient which is nearly unity. Then the rate of condensation should be equal to the volume increase. that is;

$$\frac{\Delta m A}{d} = \frac{dv}{dt} \quad cm^3\ s^{-1} \qquad (2.4)$$

The radius of curvature of the two grains at the contact points is approximately $\frac{x^2}{2r}$

(for $\frac{x}{r} < 0.3$); the lens area between spheres is approximately equal to $\frac{\pi^2 x^3}{r}$ the

volume bounded by the lenticular surface is approximately $\frac{\pi x^4}{2r}$ that is ;

$$\rho = \frac{x^2}{2r}; \quad A = \frac{\pi^2 x^3}{2r}; \quad v = \frac{\pi x^4}{2r} \qquad (2.5)$$

Substituting values for Δm in equation (2.3), A and v in equation (2.5) into equation (2.4) and integrating, then a relationship for the rate of growth of the bond area between particles can be obtained of the form :

$$\frac{x}{r} = \left(\frac{3\sqrt{\pi}\,\gamma M^{3/2} p_o}{\sqrt{2} R^{3/2} T^{3/2} d^2} \right)^{1/3} r^{-2/3}\, t^{1/3} \qquad (2.6)$$

This equation gives the relationship between the diameter of the contact area between particles and the variables influencing its rate of growth.

Evaporation-condensation may be readily compared with the diffusion mechanism (see figure (2.2) mechanism 5), since calculation of the kinetics of this process is exactly analogous to the determination of the rate of sintering by the evaporation-condensation process. The rate at which material is discharged at the surface area is equated to the increase in the volume of material transferred, but the geometry is slightly different :

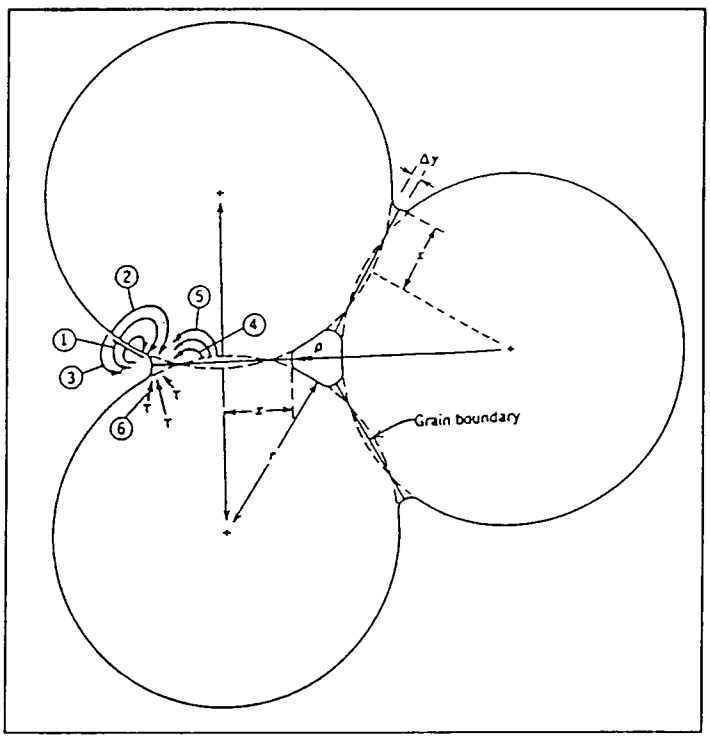

Figure (2.2) : Matter transport by diffusion mechanism 5, during the initial stage of sintering [ref 2].

$$\rho = \frac{x^2}{4r}; \quad A = \frac{\pi^2 x^3}{2r}; \quad v = \frac{\pi x^4}{4r} \qquad (2.7)$$

To visualize the process it is easiest to consider the rate of migration of vacancies. Considering that there are differences in vapour pressure between the surface of high negative curvature and the nearly flat surfaces, then there is a difference in vacancy concentration :

$$\Delta c = c - c_o = \frac{\gamma a^3 c_o}{kT\rho} \qquad (2.8)$$

where a^3 is the atomic volume of the diffusing vacancy, k is the Boltzmann constant, c is the concentration of vacancies, γ is the boundary energy, and Δc is the excess concentration over the concentration on a plane surface c_0.

The flux of vacancies diffusing away from the area per unit time per unit circumferential length under this concentration gradient can be determined graphically. It is given by :

$$J = 4D_v \Delta c \qquad (2.9)$$

where D_v is the diffusion coefficient for vacancies, D_v will be equal to $D^*/a^3 c_o$, where D^* is the self-diffusion coefficient. Combining (2.8) and (2.9) with a continuity equation similar to (2.4), we obtain the result :

$$\frac{x}{r} = \left(\frac{40\gamma a^3 D^*}{kT}\right)^{1/5} r^{-3/5} t^{1/5} \qquad (2.10)$$

With diffusion , in addition to the increase in contact area between particles, there is an approach of particle centres and a corresponding reduction in sample size. The rate of this approach is given by $\frac{d}{dt}\left(\frac{x^2}{2r}\right)$. Substituting from equation (2.4), we obtain :

$$\frac{\Delta V}{V_o} = \frac{3\Delta L}{L_o} = 3\left(\frac{20\gamma a^3 D^*}{\sqrt{2}kT}\right)^{2/5} r^{-6/5} t^{2/5} \qquad (2.11)$$

These results indicate that the growth of bond formation between particles increases as the one-fifth power of time (a result which has been experimentally observed for a number of metal and ceramic systems), [2.3], and that the shrinkage of a compact densified by this process should be proportional to the two-fifths power of time.

The parameter $\frac{x}{r}$ is a measure of the pore shape and size, and will increase if r decreases (i.e. shrinkage) or if x increases (i.e. pore size decreases). Comparison of equations (2.6) (evaporation-condensation) and (2.10) (diffusion) shows that $\frac{x}{r}$ is slightly less sensitive to changes in r in the diffusion case, although overall the change in r is of course greater. More important is the time dependence, and at first glance equation (2.6) suggests that evaporation-condensation is a stronger function of time. The temperature dependence of the diffusion process appears superficially to be less strong than for the evaporation-condensation process. However, this ignores the temperature dependence implicit in the diffusion coefficient D^*, since D^* is a thermally activated parameter [2.3] of the form :

$$D^* \propto \exp\left(\frac{\Delta E}{kT}\right) \qquad (2.12)$$

The temperature dependence of the solid state process may well be pronounced depending on the activation energy ΔE. Hence, in practice temperature may be (and usually is) an important controlling parameter for sintering in the case of solid state diffusion. For evaporation-condensation, $\frac{x}{r} \propto T^{1/2}$ and sintering rate is generally less strongly dependent on the temperature.

In conclusion, the previous equations, and similar relationships for the alternate matter transport processes which we shall not derive, are important mainly for the insight they provide on the variables which must be controlled in order to obtain

reproducible processing and densification. It is seen that the sintering rate steadily decreases with time, so that merely sintering for longer periods to obtain improved properties is impracticable. Therefore, time is not a major or critical variable for process control. Conversely, control of particle size is very important, since the sintering rate is roughly proportional to the inverse of the particle size [2.3], emphasizing the crucial role of milling/mixing in the preparative process.

2.2.2 - Liquid Phase Sintering :

Liquid phase sintering is a sintering process facilitated by the intervention of a reactive liquid [2.2]. This process is used for materials which are difficult to sinter, such as Si_3N_4 and SiC [2.2], where the wetting of the solid particles by the liquid at high temperatures and the solubility of the solid in the liquid are very important.

Liquid-phase sintering involves the removal of ions or atoms from surfaces of higher energy and depositing them on surfaces of lower energy [2.4] (see figure (2.3)). The highest-energy surfaces are those with small radii of convex curvature [2.2,2.4], the lowest-energy surface are those with small radii of concave curvature, large radii surfaces and plane surface are intermediate [2.2,2.4].

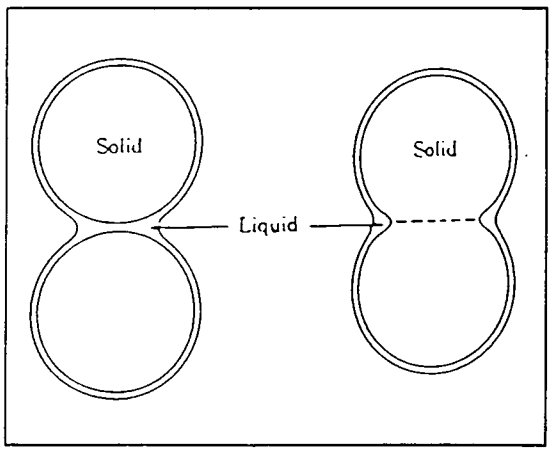

Figure (2.3) : Schematic of liquid-phase sintering [ref 3].

It is found that the rate of densification by liquid phase sintering increases as the liquid viscosity decreases at high temperature. Densification is also affected by the liquid's surface tension and by the initial shear stress required to effect deformation [2.4]. In the case of liquid phase sintering, material transfer from pore surface s to the grain boundaries is more rapid where a process of solution and precipitation can occur through the medium of a liquid than

in the case of diffusion through the solid along grain boundaries [2.1].

2.2.3 - Grain Growth :

This is the process by which the average grain size of strainfree or nearly strainfree material increases continuously during heat treatment without change in the grain size distribution, there is a constant rate of grain growth for the new strainfree grains. The grain size is, $d = U(t-t_o)$, where U is the growth rate (cm s^{-1}), t is the time, and t_0 is the induction period [2.3]. The importance of controlling grain growth as an integral part of controlling sintering phenomena cannot be overestimated, when grain growth occurs, many pores become isolated from grain boundaries, and the diffusion distance between pores and a grain boundary becomes large, and the rate of sintering decreases [2.3]. Consequently, the grain growth processes must be actively prevented in order to obtain complete densification. Usually densification continues by a diffusion process until about 10% porosity is reached; at this point rapid grain growth occurs by secondary recrystallization (the process by which a few large grains are nucleated and grow at the expense of finer grains), and the rate of densification is sharply reduced. In order to increase the densification, secondary recrystallization should be prevented. Control can be achieved, by adding certain additives to slow down the boundary migration to a point at which it is possible to obtain pore elimination [2.3]. Extensive grain growth may also result at high sintering temperatures.

Isothermal grain growth proceeds under the driving forces of interfacial energy minimization, where the various type of surfaces may be classified as interfaces. These include external crystal/vapour surfaces, interphase surfaces (e.g., solid/liquid boundaries), and grain boundaries. The existence of interfacial energies has several consequences which are of importance in the realm of ceramic material processing : (i) sintering can occur. (ii) microstructures are altered, and (iii) properties are affected [2.4]. Atoms along the interface with a smaller radius of curvature (smaller grains) are

less stable than the atoms at the boundary of a long grain. Therefore, the small grain is dissolved by the liquid, and the atoms precipitate onto the surface of the larger grains. Single-phase ceramics also exhibit grain growth [2.4].

Grain growth also takes place in parallel with densification and is energetically favoured by the reduction in the area of grain boundaries. This is because the crystal lattice has a lower free energy than the highly defective grain boundary region and the ratio of boundary area to volume for large grains is smaller than that for small grains [2.1]. Grain growth may be restrained by the presence of a liquid phase [2.3].

2.3 - The Cubic Spinel Type Structure :

Metal oxides are known to exist in a variety of structure types (e.g. rock salt, wurtzite, zinc blend, ..etc, for more detail see ref [2.3]), however, in the case of Zn_2SnO_4 the structure is cubic spinel and therefore, only this structure will be discussed here. The cubic spinel modification, is common in oxides which take the general formula XY_2O_4, such as magnesium aluminate, $MgAl_2O_4$, and Zn_2SnO_4, where the oxygen ions are arranged in a face-centred-cubic close packing arrangement, as shown in figure (2.4). The spinel structure can take on two forms :

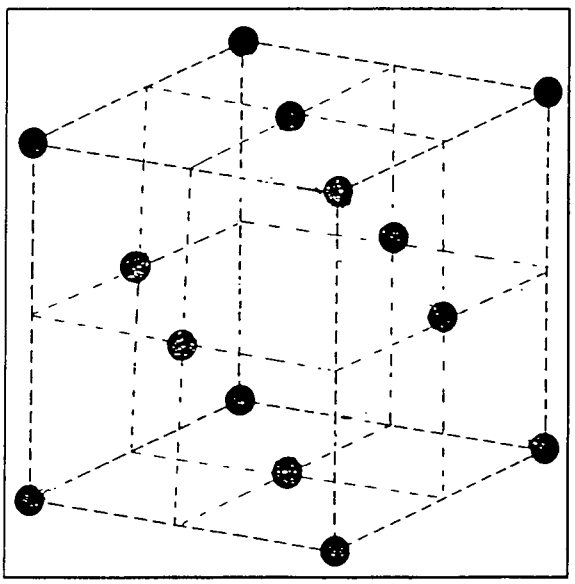

Figure (2.4) : A face-centred cubic lattice.

a) The "normal" spinel structure which is generally found in ternary oxides involving divalent (X^{2+}) and trivalent (Y^{3+}) cations. The divalent cations generally occupy the tetrahedral sites and the trivalent cations occupy the octahedral sites. This may be represented by the notation $X^{2+}[Y_2^{3+}]O_4$, (the cations inside the brackets

occupy octahedral sites and those outside the brackets are in tetrahedral sites) and are

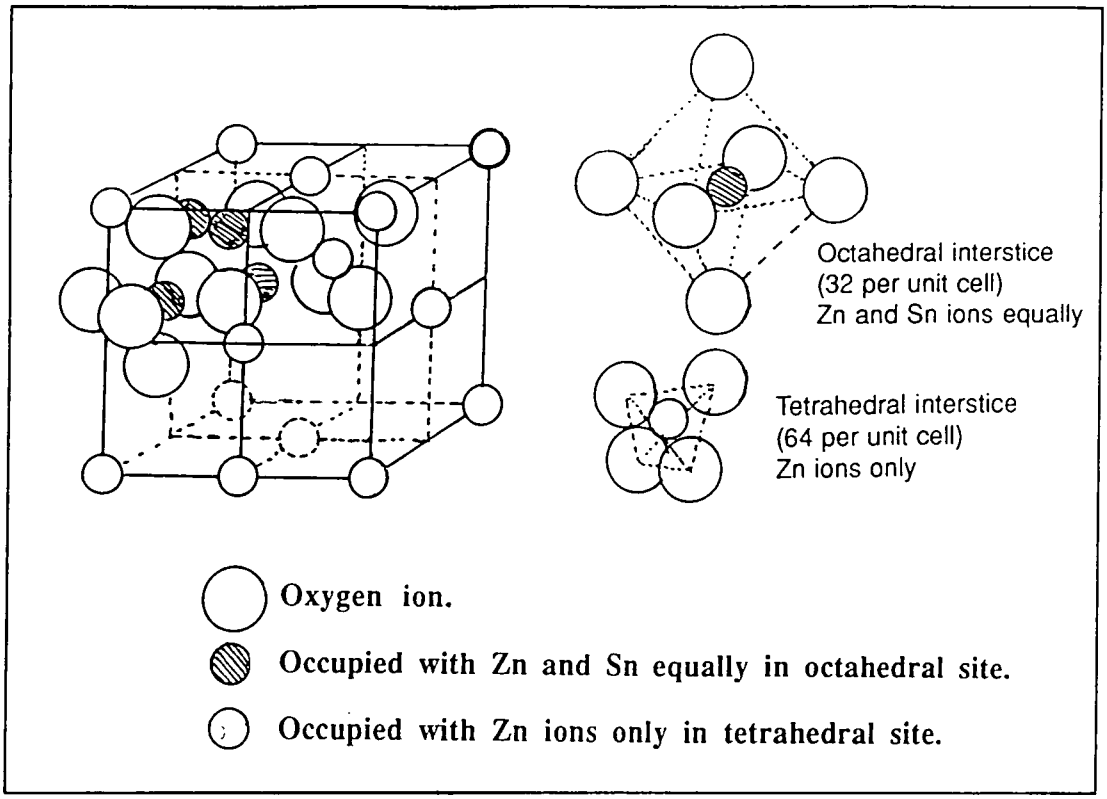

Figure (2.5) : Arrangement of Zn_2SnO_4 atoms (inverse spinel structure type) [ref. 2].

frequently referred to as {2-3} spinels. Example of this structure include $MgAl_2O_4$, and $ZnAl_2O_4$. In principle ternary oxides involving tetravalent and divalent cations , or {4-2}, may also crystallise in the normal spinel structure, i.e. $X^{4+}[Y_2^{2+}]O_4$ [2.5,2.6], but no examples are listed in the literature.

b) The {4-2} spinel oxides generally adopt the "inverse" spinel structure, $Y^{2+}[X^{4+}Y^{2+}]O_4$ [2.6], where Y^{2+} ions occupy the tetrahedral sites while the octahedral sites are occupied by equal numbers of X^{4+} and Y^{2+} ions. Zinc stannate is thought to take this form, i.e. $Zn[SnZn]O_4$ [2.3,2.5,2.6]. The arrangement of the ions for Zn_2SnO_4 can be seen in figures (2.5),(2.6). The inverse spinel structure is also adopted by some {3-2} spinels, such as $NiAl_2O_4$, with the cation distribution given as $Y^{3+}[X^{2+}Y^{3+}]O_4$

[2.6].

In {4-2} spinel structures (such as Zn_2SnO_4) the unit cell consists of 32 oxygen ions, 8 tetravalent (i.e. Sn) cations and 16 divalent (i.e. Zn) ions. As discussed earlier the oxygen ions lie on an f.c.c. sub-lattice, which consists of close-packed planes stacked in an ..a,b,c,a,b,c,..[2.7] arrangement. The cations are distributed within the interstices of the oxygen sub-lattice, of which there are two types figure (2.5):

- 64 tetrahedral interstices, where the cation is surrounded by $4O^{2-}$ ions;
- 32 octahedral interstices, where the cation is surrounded by $6O^{2-}$ ions.

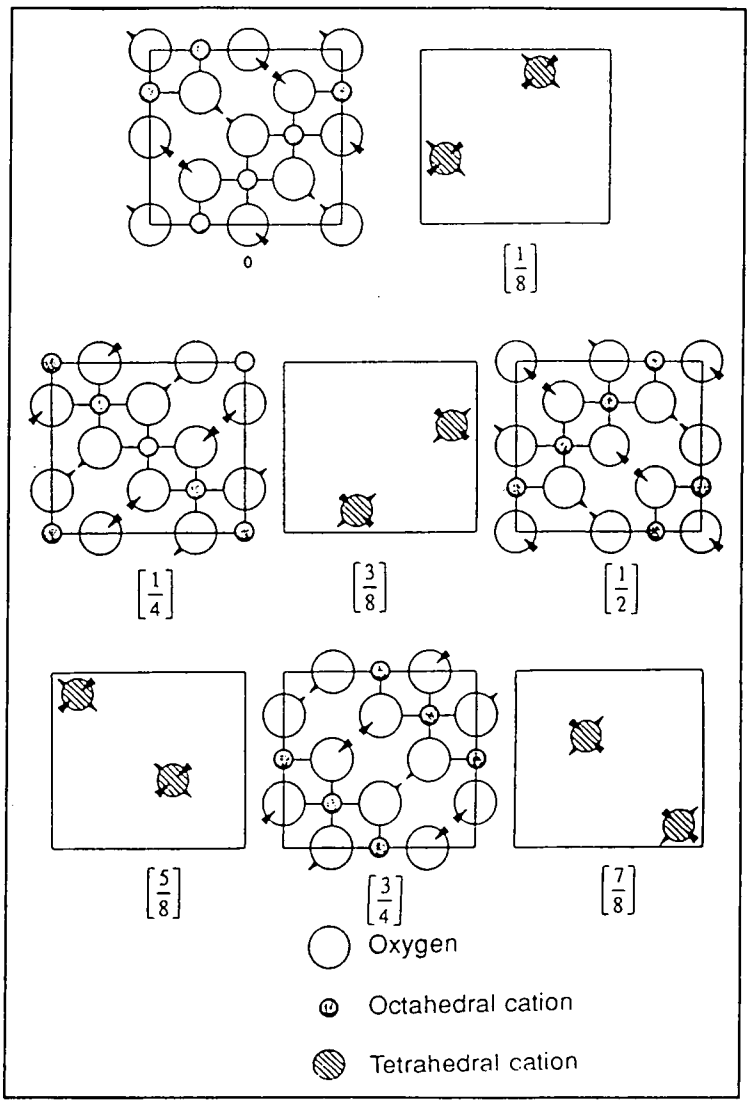

Figure (2.6) : Inverse spinel structure type Layers of atoms parallel to (001) [ref. 2].

There are, as a result, 96, potential cation sites within the unit cell, but only 8 tetrahedral and 16 octahedral sites are actually occupied, therefore 72 sites are vacant.

The normal and inverse spinel structures discussed above are "idealized" structures in which the 24 cations are not distributed randomly over the 96 possible

sites, but instead occupy specific positions within the unit cell. In practice, the cation distribution will not conform to the ideal completely, due to the influence of point defects, impurities etc. Clearly, the extent to which a given crystal structure is stoichiometric will depend on the preparation conditions, purity etc., and there appear to be no general rules governing this.

In the present work, it will be assumed that Zn_2SnO_4 crystallines in the cubic inverse spinel structure and structural data, e.g. x-ray diffraction spectra, will be analysed under this assumption.

2.4 - References:

[2.1] - Moulson A. J. and Herbert J. M.,'Electroceramics', (Chapman and Hall, London, (1990).

[2.2] - Ichinose N.,'Introduction to Fine Ceramics',(John Wiley and Sons, New York,1987).

[2.3] - Kingery W. D., Bowen H. K. and Uhlmann D. R.,'Introduction to Ceramics', (John Wiley and Sons, New York, 1976).

[2.4] - Van Vlack L. H.,'Physical Ceramics for Engineers', (Addison-Wesley Publishing Company, Inc., Ed. Norton F. H., p194, p269, 1964).

[2.5] - Grimes R. W., Anderson A. B., and Heuer A. H., J. Amer. Chem. Soc., **111**, 2168, (1989).

[2.6] - Verwey E. J. W. and Heilmann E. L., J. Chem. Phys, **15**, 174, (1947).

[2.7] - Kittel C.,"Introduction to solid state physics.", John Willey & Sons, Forth Edition, page 28, (1971).

CHAPTER III

EXPERIMENTAL TECHNIQUES :

3.1 - Introduction :

This chapter is devoted to a discription of the techniques employed in the formation of Zn_2SnO_4 (bulk and thin film), and hence the chapter will describe stage by stage, beginning with the mixing of raw materials to the final stages of formation; it is concerned with ways of mixing and firing (material preparation) and thin film growth. In addition to materials preparation, many attempts were also made to control the resistivity (reducing treatements , and doping) and these are described. Characterisation techniques are classified according to their application in the current study. For example, scanning electron microscopy (SEM) with EDAX and X-ray diffraction techniques were used for structural characterisation (section 3.6), while I-V and C-V were used in the metal-semiconductor characterisation. A.c. impedance measurements, d.c. conductivity measurements and Hall coefficient measurements were used in the electrical characterisation of bulk and thin film material. These experiments are all well established and the reader is referred, for more details, to relevant textbooks and review articles whenever appropriate.

Semiconducting zinc stannate ceramic pellets were prepared by a solid state reaction of the constituent oxide powders, following a conventional ceramic processing route. The as-fired samples were then often subjected to further reduction and doping procedures, in order to control the electrical conductivity of the material. Thin film zinc stannate was also deposited onto glass and examined using the scanning electron microscope and energy dispersive x-ray analysis, and x-ray diffraction to determine their morphology, microstructure and composition. Electric and dielectric measurements were carried out to investigate the electrical properties of the material, to determine the best conditions for sintering, reducing and doping, and to find how the conductivity behaved with temperature. The ohmic behaviour of the contacts, was investigated by measuring the current as the voltage was increased. Conductivity,

mobility, carrier concentration, and Hall coefficient were measured as functions of temperature from liquid nitrogen temperature to room temperature. A.c. impedance measurements at room temperature were used in attempts to separate the resistance attributable to the grain bulk from that due to grain boundary or hopping processes. Finally, Schottky contacts were formed and used to make C-V and I-V measurements.

The following sections of this chapter describe the experimental techniques used in the preparation of samples and their subsequent microstructural and electrical characterization. Methods of analysis of these results are described in later chapters, where they are more relevant to the discussion.

3.2 - Sample Preparation - Powder Processing :

Zinc stannate semiconducting ceramics were prepared using commercially available SnO_2 and ZnO mixed in the molar ratio $1SnO_2 : 2ZnO$. The process is shown schematically in figure (3.1). The powders were weighed and either mixed dry in a glass pestle and mortar, or ball milled together in a polyethylene jar, (where the mixing media were agate balls and deionized water) for 12 hours. The resulting slurry was filtered and dried to give a powder cake which was then crushed to a fine powder in a glass pestle and mortar. The resulting powder after crushing was remixed and small pellets 13mm in diameter and $\sim$ 1mm thick were pressed under a load of 2.4 tons/m^2, and then put into a muffle furnace to be sintered.

Any contamination from the jar in which the powders were mixed was not expected to be serious since, it was made of polyethylene, which is completely combustible. Although the mixing balls were agate, a very hard form of SiO_2, Si was observed in the compound through EDAX. After each stage all equipment was thoroughly washed with deionized water to ensure cleanliness and the powders, before and after mixing, were covered to reduce contamination.

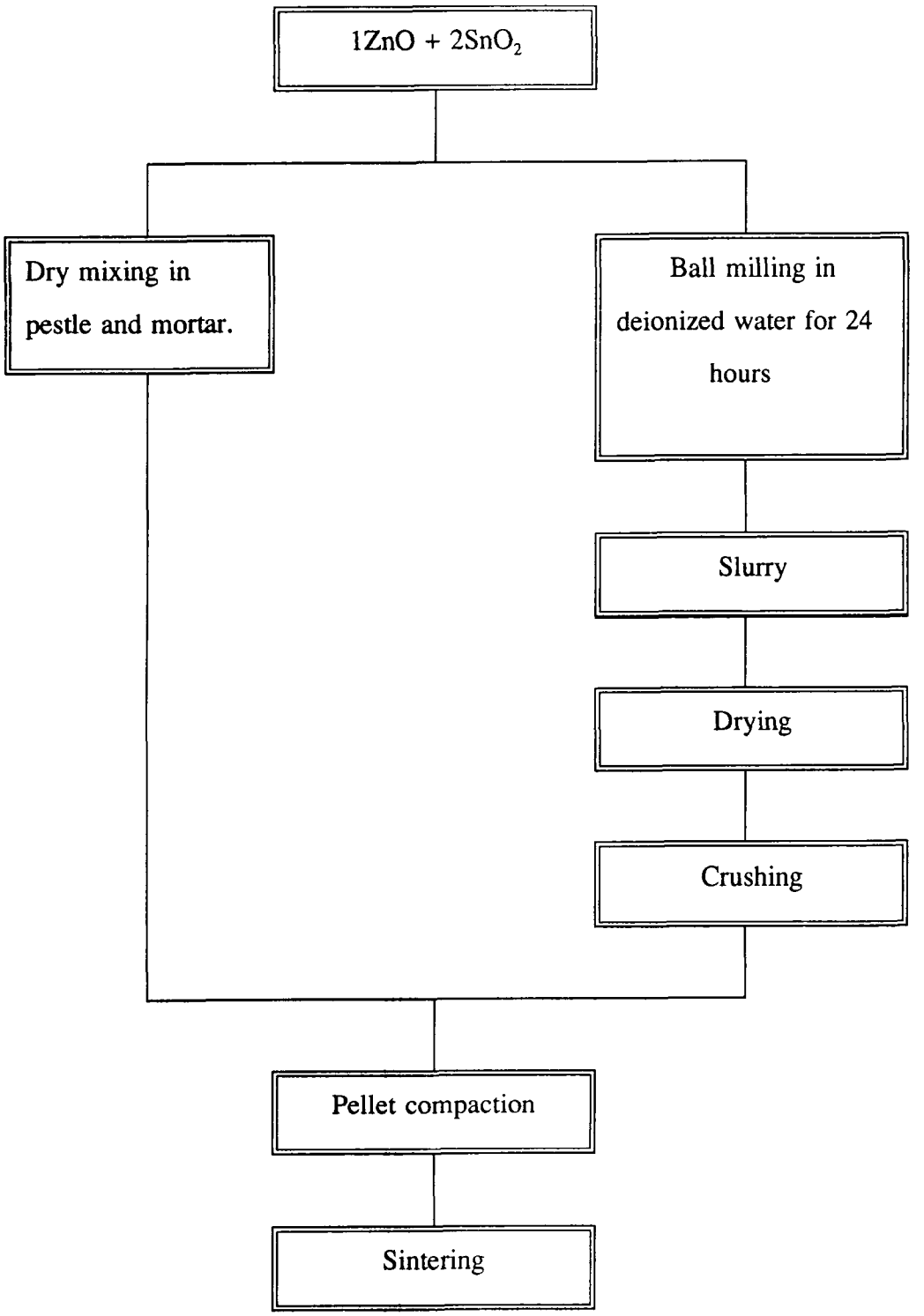

Figure (3.1) : Mixed oxide route for Zn_2SnO_4 processing.

3.3 - Sample Preparation - Sintering :

Sintering was carried out using either a Vecstar VH2 1600°C muffle furnace or a Lenton Thermal Designs 1600°C tube furnace. Figure (3.2) shows a typical sintering cycle, showing each stage of the sintering process. The entire cycle was carried out in air and samples were placed on zirconia plates to avoid contamination from the furnace walls.

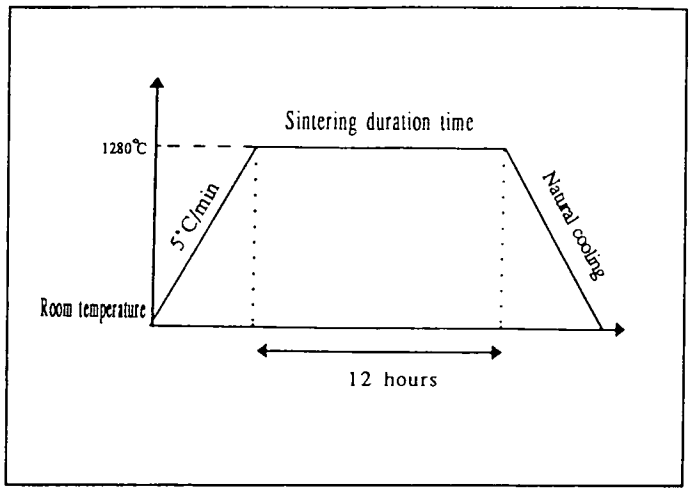

Figure (3.2) : Typical heating profile for the sintering cycle.

3.4 - Sample Preparation - Reduction :

Reduction treatments typically took place at 400-450°C for 14 hours, with a typical heating rate of 10°C min^{-1}, in a Lenton Thermal Designs 1600°C tube furnace. The furnace had been adapted to allow the atmosphere to be controlled. This reduction process was carried out using a mixture of 25% H_2 + 75% N_2 flowing through the furnace at a rate up to 450 cm^3 min^{-1}. Figure (3.3) shows the typical reducing cycle of temperature versus time.

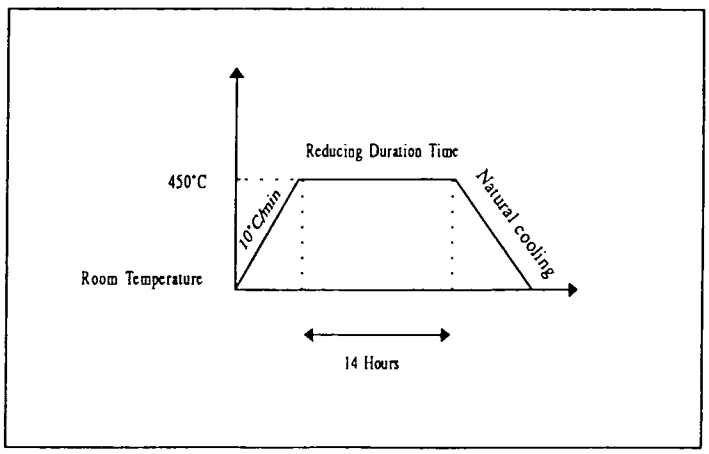

Figure (3.3) : Typical profile of T versus time for the reducing treatment.

3.5 - Zinc Stannate Thin Film Preparation :

Thin films of zinc stannate were prepared from a Zn_2SnO_4 target by Electron Beam Evaporation. A schematic diagram of the apparatus is shown in figure (3.4). An electron beam of sufficient intensity was emitted thermionically from a molybdenum filament (cathode), accelelarated and focused onto the evaporant material (Zn_2SnO_4

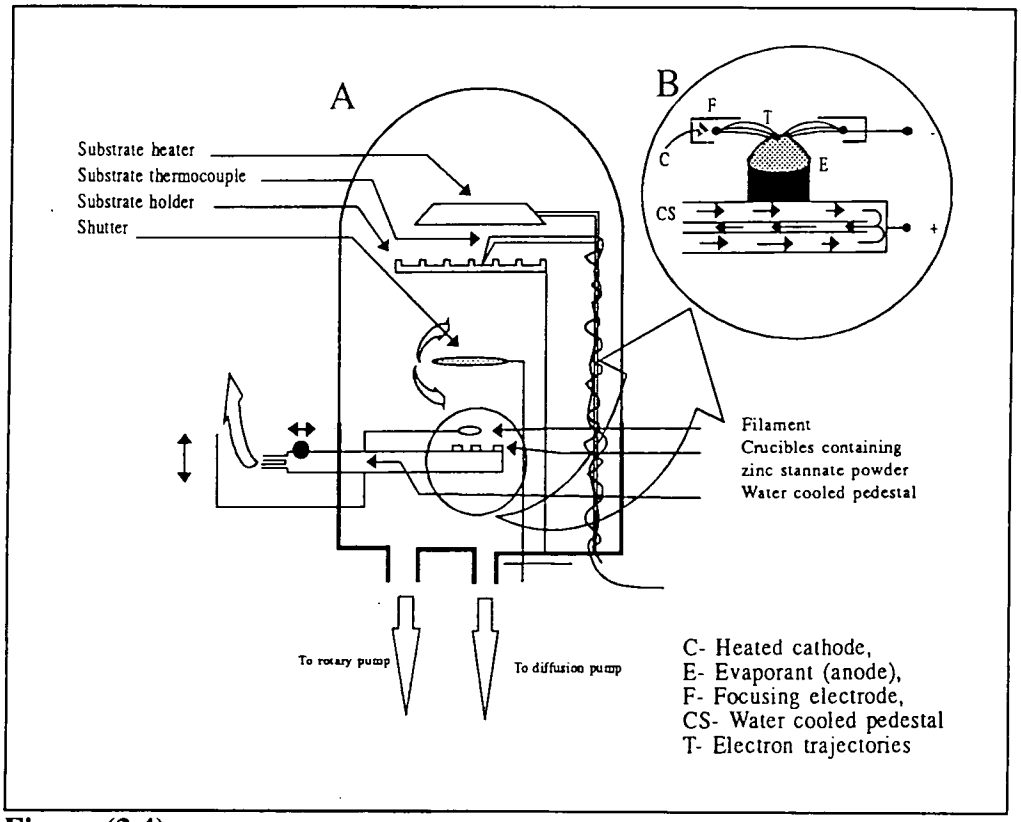

Figure (3.4) : a)-Schematic diagram of the Electron Beam Evaporator, b)- Schematic diagram of the Electron Beam Source.

powder). The applied voltage on the cage was about 2.5 kV. The focused electrons heated the evaporant powder at the site of incidence to the temperature required for evaporation. The method enables very high temperatures to be attained and to evaporate materials which would otherwise be evaporated only with difficulty or could not be evaporated at all. An additional advantage of the method is the prevention of contamination of the evaporation source material : The beam heats only the evaporant whereas the target holder is usually cooled. At the same time no particles emitted from

the heated filament can reach the substrate [3.1]

3.6 - Microstructural Characterisation :

3.6.1 - Scanning Electron Microscopy (SEM):

Scanning Electron Microscopy (SEM) techniques are well suited for the micro-characterisation of semiconductors, since they provide high spatial resolution and the simultaneous availability of a variety of modes and forms of contrast [3.2]. The construction, modes of operation, and uses of the SEM are described in detail in the textbooks by Goldstein et al [3.3,3.4] and Holt et al [3.5].

Samples were examined using a Cambridge Instruments S600 scanning electron microscope (SEM), in secondary electron emission mode. In the SEM an electron beam $\sim$ 100Å in diameter is scanned across an area of the sample under investigation. A small proportion of the beam is reflected elastically from the surface (backscattered electrons). The rest undergo inelastic collision, resulting in the generation of secondary electrons which are able to escape from up to 500Å below the surface. It is these secondary electrons which are used in routine topographic imaging.

The surfaces of samples which were examined using SEM in either the as-fired state, (where the sample was removed from the furnace and immediately set onto an aluminium stub, taking care to keep the top surface uppermost), or reduced and/or doped. The polished surface method (using emery paper and successively fine grades of alumina grit until the region of the sample to be examined is reached) is the one most commonly used in the study of ceramic microstructures. There are, however, a number of associated problems, where grains which have been pulled away may give the sample the appearance of being more porous than it actually was. In addition the average grain size is difficult to determine, since there is no certainty that the grains have been cut across their diameters.

The purpose of examining samples with the SEM throughout this work was to observe the microstructure of each sample and then to obtain an estimate for the

average grain size, and an indication of shape and distribution. In addition, the

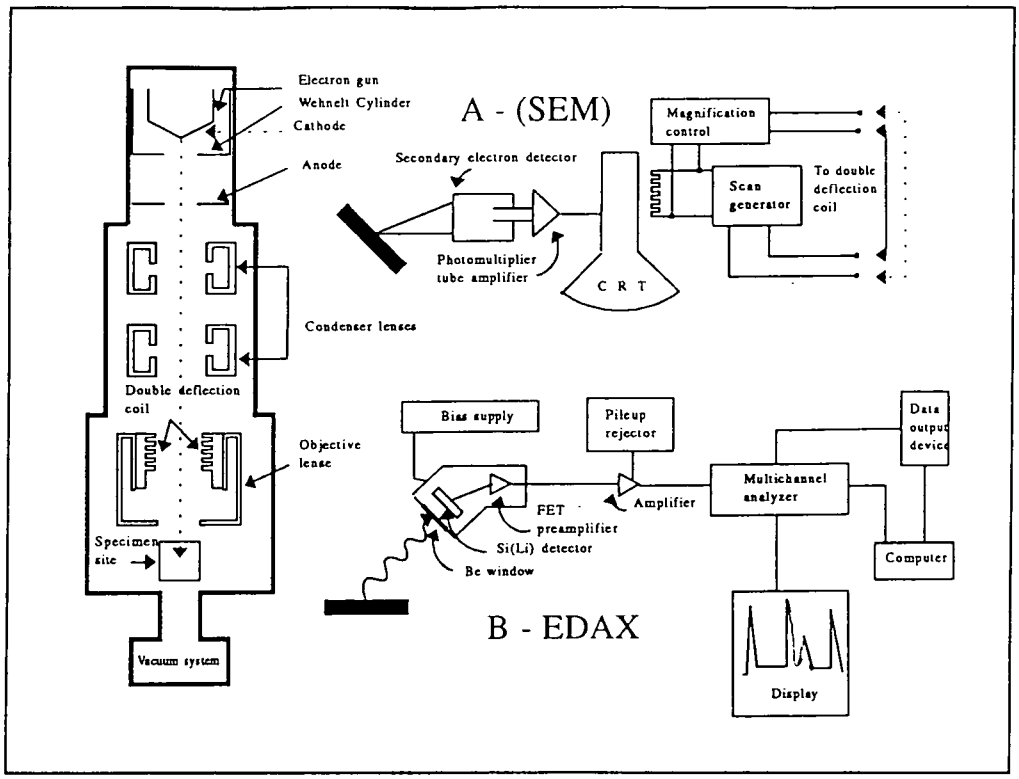

Figure (3.5) : Schematic diagram of the scanning electron microscope: a)- Secondary electron mode, b)- EDAX mode.

presence of any second phase on the surface was detected and observed. Hence, most of the microscopy was performed using as-fired and reduced surfaces. Figure (3.5) shows the diagram of the SEM and EDAX systems.

3.6.2 - Energy Dispersive X-ray Analysis :

A Link Systems 860 Energy Dispersive X-ray (EDAX) analyser, fitted to the Cambridge Instruments S600 microscope, was used to determine the elemental composition of samples [3.6]. X-ray microanalysis is possible in the SEM as a result of the formation of characteristic x-rays from the sample when it is bombarded by the electron beam. The primary electrons eject core (and other) electrons (secondary electrons) and subsequent relaxations from higher energy levels into the empty states are accompanied by the emission of x-rays. For example, when the electron has been

ejected from the K orbital, electrons from the L, M and higher shells may relax into the K shell. Those which do so from the L orbital emit Kα x-rays. The process is described by Moseley's law, $(\nu)^{1/2} = C\ (Z - \sigma)$ where C is a constant, Z is the atomic number and σ is a screening factor. Evidently elemental analysis is possible if the energy of the x-ray can be measured [3.6]. Furthermore, the electron beam of the SEM ($\sim$ 10 nm in width) may be positioned onto features of the samples, observed using secondary electron imaging, enabling analysis of surface features.

The EDAX analyser comprised a liquid nitrogen cooled, lithium-drifted silicon reverse biassed p-n junction. The x-rays fall onto the depletion region of the junction, where energy transfer takes place to form electron-hole pairs. Since only 3.8eV is required on average to make each pair, which is much less than the energy of the x-rays, a large number of pairs are generated. The magnitude of the resulting pulse of electrical current is then proportional to the energy of the x-ray. The number of current pulses and their magnitudes are sorted using a multichannel analyser, and displayed on a screen as charts of number of counts versus energy. The spectrum may then be compared with those stored in a computer memory, for elemental identification. From $(\nu)^{1/2} = C\ (Z - \sigma)$ it can be seen that the frequency of the characteristic x-rays decreased as the square of the atomic number and since long wavelength x-rays are more strongly absorbed in most media, lighter elements are less easily detected by EDAX. Elements having atomic number less than 11 (Na) could not be detected with this analyser. In addition, the signal/noise ratio of the detection system was $\sim$ 50, which imposed a detection limit on any element of $\sim$2%.

EDAX was used to find the composition of grains and to identify any intergranular phases. Other features on the surface, e.g. dust particles or spots of impurities, were also examined using this technique. It was not possible, however, to detect any differences in dopant concentration at grain boundaries as a result of the detection limit.

3.6.3 - X-ray Diffractometry :

X-ray diffraction (XRD) spectra were obtained with a Philips Diffractometer, using Cobalt radiation (Cokα) of wavelength 1.790Å together with an iron filter. Sintered pellets were crushed and the powder sprinkled onto double side tape fixed to glass slides. The XRD spectrum was typically obtained with a goniometer scanning rate of one degree per minute. Planes able to satisfy the Bragg condition, will give rise to diffraction peaks in the spectrum and these may be used in equation (3.1) to determine the lattice planes :

$$2d\sin\theta = n\lambda \qquad (3.1)$$

where d = inter-planer spacing, θ = diffraction angle, λ = wavelength and n is an integer corresponding to the order of diffraction. Since Zn_2SnO_4 is cubic then the lattice constant (a) can be obtained from :

$$\frac{1}{d^2}=\frac{h^2+l^2+k^2}{a^2} \qquad (3.2)$$

where hkl are the Miller indices of the plane. A similar procedure was used for the thin films, where the layers were stripped off from the glass substrate and then sprinkled onto double sided tape as described above.

3.6.4 - RHEED Studies :

Reflection High Energy Electron Diffraction (RHEED) involved the diffraction of an electron beam at grazing incidence. The technique, therefore only samples surface layers. Figure (3.6A) shows the form of a diffraction pattern observed for a polycrystalline sample (e.g. ZnO [3.7,3.8]), where no preferred orientation is present. The pattern consists of a set of continuous concentric semi-circles. The next type of a pattern (figure (3.6B)) demonstrates the existence of preferred order as indicated by the build up of intensity in short arcs rather than complete semicircles. Figure (3.6C)

is an idealised pattern taken from a material with a highly preferred order. Crystallinity was assessed by the examination and comparison of one spectrum with

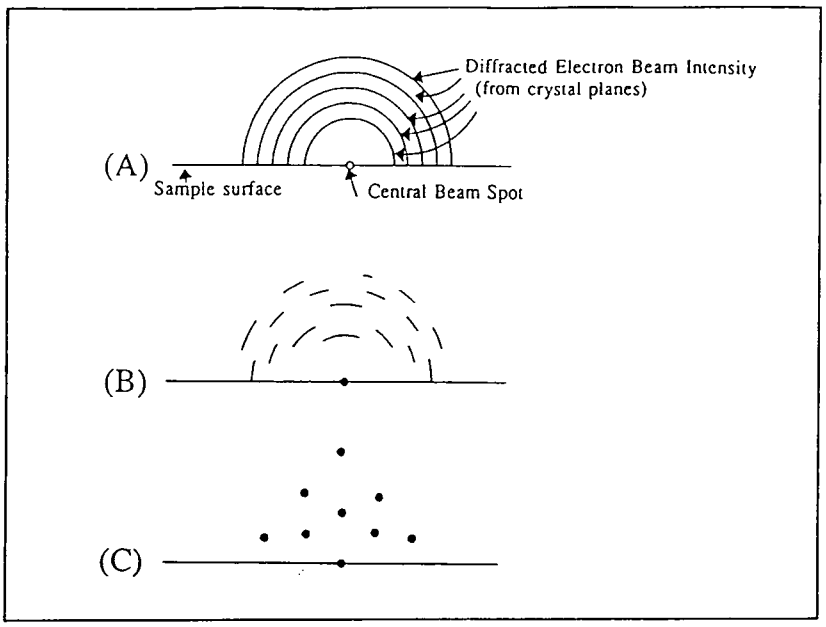

Figure (3.6) : RHEED patterns; a) randomly oriented polycrystalline sample, b) Ploycrystalline sample with preferred order, c) Single crystal sample.

another to identify relative changes in the structure. RHEED studies were carried out in a modified JEM 120 transmission electron microscope (TEM). This technique was used to assess the crystallinity and the degree of preferred orientation of the crystallites. This technique samples the first few monolayers of the film, is non-destructive and characterisation takes only a few minutes.

3.7 - Electrical Characterisation Techniques :

3.7.1 - Bulk sample characterisation :

3.7.1a - Contact testing method (bulk I-V) :

The purpose of these measurements was to investigate the degree to which the contacts were ohmic. Figure (3.7) shows the arrangement of the apparatus for these experiments. Single short pulses ($\sim$ 1.5ms) of the set voltage were applied across the sample, which was placed in series with a resistance of known value. The

voltages across the resistor and the sample were measured using a digital storage oscilloscope and used to calculate the current through the circuit and thus the

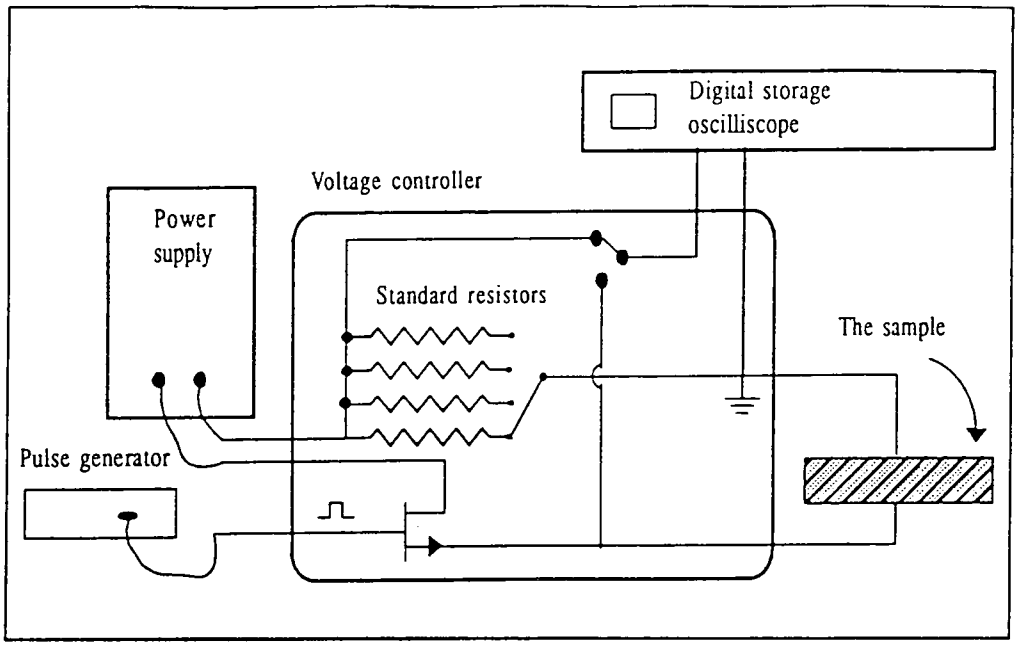

Figure (3.7) : Apparatus for Current-Voltage measurements.

resistivity of the sample under the applied electric field. Pulses were used to avoid Joule heating effects.

3.7.1b - Conductivity Measurement Techniques :

A - Four point probe method :

A simple arrangement for resistivity measurement is the four-point-probe method shown in figure (3.8), where the probes are arranged as parallel straight lines with length (t) separated by a known distance (L). The current (I) flows between outer probes while the voltage (V) is measured between the inner probes. The sample should be of thickness (d) . The resistivity can be obtained from the equation :

$$\rho = \left[\frac{V}{I}\right] \times \frac{d \times t}{L} \qquad (3.3)$$

In practice, current flow will probably be nonuniform and the measured resistivity will

therefore be an average value over the sample area. A Keithley 617 programmable Electrometer was used as a current supply, and a Keithley A195 multimeter was used to measure the voltage. An Oxford Instruments cryostat was used to measure the resistivity at low temperature using liquid nitrogen, while the temperature was controlled by an Oxford Instruments Intelligent Temperature Controller ITC4. The system was controlled by an Archimedes computer, and the measurements were made in the temperature range of 80K < T < 300K.

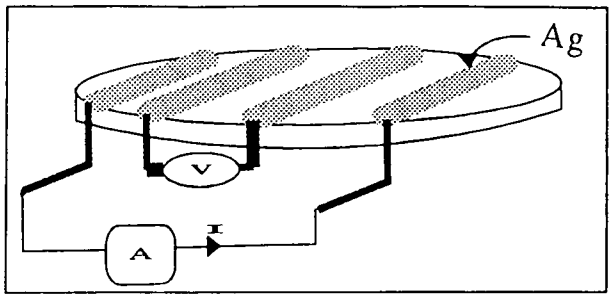

Figure (3.8) : Four-Probe-Method for conductivity measurements.

B - Van der Pauw Methed :

Van der Pauw showed that the resistivity and Hall voltage could be measured for any flat sample of arbitrary shape using four ohmic contacts (arbitrarily labelled 1,2,3 and 4) in figure (3.9) [3.9]. The effects of the exact shape of the sample on the measured results are minimised so long as the assumptions on which the calculation is based are maintained. These include; uniform thickness of the sample and negligably small contacts positioned anywhere at the periphery of the sample.

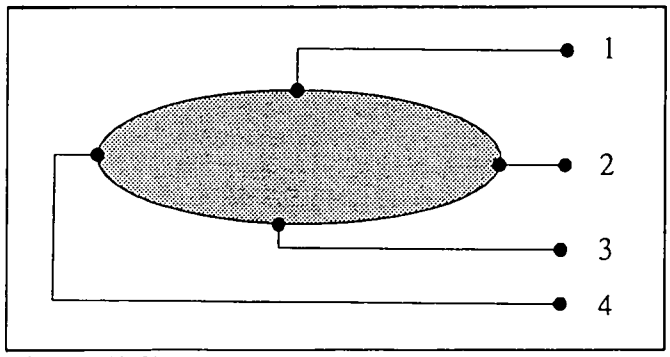

Figure (3.9) : Four probe method, (Van der pauw method) for the resistivity measurements and Hall coefficient.

Experimentally, four In/Ga contacts were applied to the sample substrate after polishing. Measurements were made of the resistance between consecutive pairs of contacts ($R_{12,34}$, $R_{23,41}$, $R_{34,12}$, and $R_{41,23}$, where the first and second pair of subscripts

refer to current and voltage terminals respectively). The resistivity is then given by the formula :

$$\rho = \frac{\pi d}{ln2}\left[\frac{R_{12,34}+R_{23,41}}{2}\right] f\left(\frac{R_{12,34}}{R_{23,41}}\right) \qquad (3.4)$$

where d is the sample thickness, and f is a correction function, full details of which can be found in reference [3.9]. This method of determining the resistivity and Hall coefficient eliminated the effects of offset potentials and provided some averaging. The measured data were smoothed using a least squares fit approach and current scans were performed in both forward and reverse directions to provide further averaging. In addition, the current - voltage data were plotted to ensure that the contacts to the sample were ohmic. This method was also used for measurements of the conductivity of the thin films.

3.7.1c - Hall Effect Measurements :

A) - Five-Probe-Method :

Rectangular bars normally with dimensions of 9 x 3 x 1 mm^3 were cut from the circular pellets. After reducing and cleaning the samples, In/Ga alloy was used to form a small area ohmic contact. The electrical contacts were connected to the sample with fine copper wires (which were fixed onto the sample holder), using quick drying silver paste. Figure (3.10), shows the contact arrangements for the voltage measurements. A potentiometer was included in the circuit to allow for offsets in the measured Hall voltage. Before

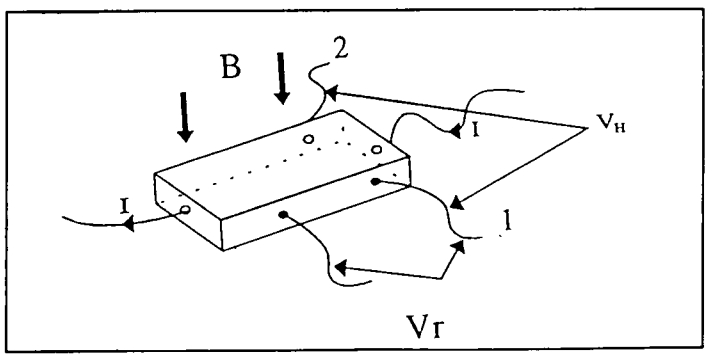

Figure (3.10) : Five-Probe-Method for Hall measurements.

applying the magnetic field,the potentiometer was adjusted so that no voltage appeared across terminals 1 and 2. This ensured that terminals 1 and 2 are on the same equipotential surface. When a magnetic field was applied the Hall voltage was developed across terminals 1 - 2. The magnetic field was then reversed, the Hall voltage remeasured, and the average of the two was taken to cancel out any effects due to misalignment of the contacts. These measurements were also made in the temperature range 80°K < T < 300°K using an Oxford Instruments (model DN1704) cryostat and ITC4 temperature controller. The average Hall voltage can be used to obtain the Hall coefficient (R_H) in the following formula :

$$R_H = \frac{V_y d}{B_z I_x} \qquad (3.5)$$

where V_y is the voltage set up between probes in the y-direction and is known as the Hall voltage, and d is the sample thickness.

B) - Van-der-Pauw-Method :

The Hall coefficient is determined from the change in resistance $R_{12,34}$ or $R_{23,41}$ (see figure 3.9) with a change in the magnetic field perpendicular to the plane of the sample ΔB [3.9]:

$$R_H = \frac{d\Delta R_{12,34}}{\Delta B} \qquad (3.6)$$

The system was automated, using an Archimedes computer, together with a constant current source, an overall controller, and a magnet and power supply. The microcomputer controlled a constant current source, the magnet power supply and a bank of reed relays designed to configure the system for each of the required measurements. There were four resistivity and two Hall configurations. Voltages were measured using a Keithley digital multimeter and communicated to the computer over an IEEE bus. The sample was placed in a cryostat which could be evacuated down to $\sim 10^{-5}$ mbar and cooled to liquid nitrogen temperatures. Manual measurements were

also made independently of computer control. R_H can be used to obtaine the carrier concentration (n) according to the formula :

$$R_H = \frac{1}{nq} \qquad (3.7)$$

where q is the electronic charge.

From equation (3.7) and (3.4) the Hall mobility (μ_H) can be determined as :

$$R_H \sigma = \mu_H \qquad (3.8)$$

Where σ is the electrical conductivity ($\sigma = 1/\rho$).

3.7.1d - Conductivity Type Testing Techniques :

A) - Seebeck Effect:

The diffusion of the mobile carriers (either holes in p-type or electrons in n-type) from higher temperature regions, to lower temperature regions can be used to determine whether a sample is n-type or p-type. If an area of a semiconducting wafer is heated locally, as shown in figure (3.11), the majority carriers diffuse away from the hot region. A voltage is then produced between the hot and cold probes, and can be used to determine the conductivity-type of the sample. If the sample is n-type the hot probe voltage will be positive with respect to the cold probe. The opposite is true for a p-type sample.

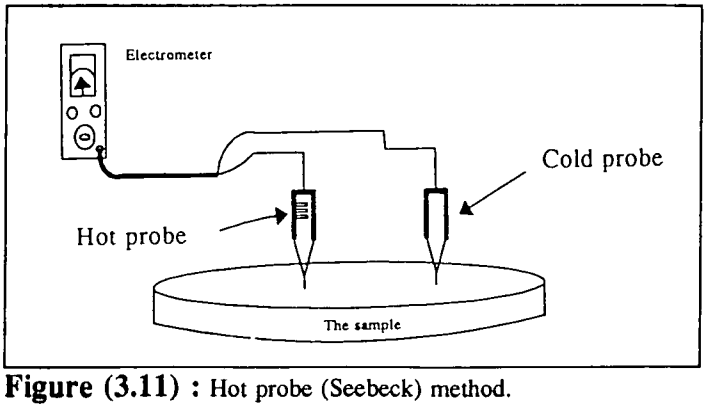

Figure (3.11) : Hot probe (Seebeck) method.

B) - Hall Coefficient :

The conductivity type can be obtained from the sign of the Hall Coefficient providing the geometry is known. Using a five-probe-method, with the current in the wafer flowing from top to bottom (figure (3.12) shows the n-type sample situation), while the magnetic field direction is from the front to the rear, the voltage will be positive on the right hand side for an n-type sample. It will be the opposite for p-type samples (i.e. the voltage will be negative on the right hand side). This is a consequence of carrier motion under crossed electric and magnetic fields fulfilling the Lorentz force equation.

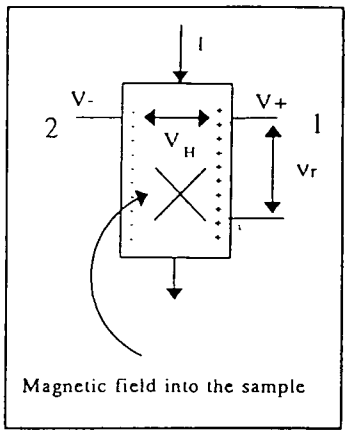

Figure (3.12) : Five point Hall method.

3.7.1e - A.c. Impedance Measurements :

Ac impedance measurements were carried out at room temperature and at frequencies up to 5 MHz using a Hewlett-Packard HP 4342A Q-meter, from which the R C, and L equivalent parameters for the sample can be calculated. For the purpose of the impedance measurements, however, a parallel connection of resistance and capacitance was required, since the parallel equivalent values could be measured using the Q-meter. The series equivalent values were then calculated from the parallel results in the usual way.

The parallel impedance is given by :

$$Z_p = \frac{R_p}{1+j\omega C_p R_p} = \frac{R_p(1-j\omega C_p R_p)}{1+\omega^2 C_p^2 R_p^2} \qquad (3.9)$$

where $\omega = 2\pi f$ and f is the frequency of the applied ac voltage. C_p and R_p are the parallel circuit equivalent resistance and capacitance, respectively.

The series impedance is given by :

$$Z_S = R_S + \frac{1}{j\omega C_S} \qquad (3.10)$$

where R_s and C_s are the series circuit equivalent resistance and capacitance respectively.

Then since Z_p must clearly be equal to Z_s as they both describe the same sample;

$$R_s = \frac{R_p}{1+(\omega C_p R_p)^2} \quad , \quad C_s = \frac{1+(\omega C_p R_p)^2}{\omega^2 C_p R_p^2} \qquad (3.11)$$

Figure (3.13) shows a schematic diagram of the parallel resistance - capacitance connection of the Q-meter. This operates on the principle of resonance

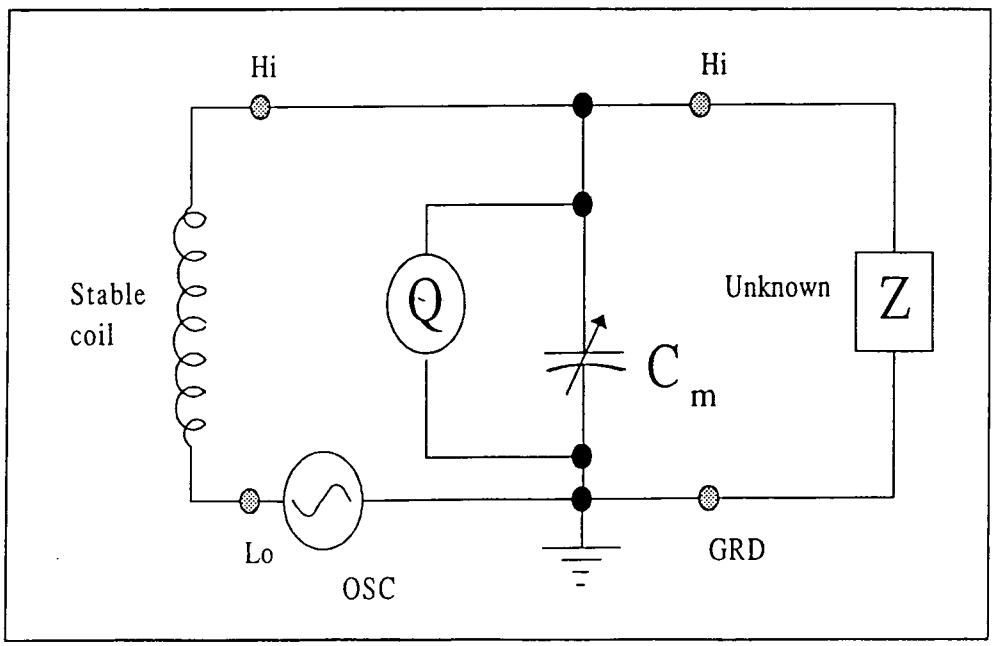

Figure (3.13) : Equivalent circuit for the Q-meter.

in parallel between the coil inductance, L, and the Q-meter(variable capacitance C_m), or the inductance and sample. Measurements were taken in the following way : firstly the Q and C_m values of the meter alone, in series with the inductor, were obtained by shorting across the sample and tuning the variable capacitor, C_m, to give a maximum

deflection on the meter. The sample was then included in the circuit, and C_m was adjusted again, to obtain resonance. If C_1 and Q_1 are the values of capacitance and Q of the meter alone and C_2 and Q_2 are those when the sample was included, the equivalent parallel resistance, R_P, and Q of the sample may be obtained using the equations :

$$Q=\frac{Q_1Q_2(C_2-C_1)}{\Delta QC_1} \qquad (3.12)$$

$$R_P=\frac{Q_1Q_2}{\omega C_1\Delta Q} \qquad (3.13)$$

where $\Delta Q = Q_1 - Q_2$

$$X_P = \frac{1}{\omega(C_2-C_2)} \qquad (3.14)$$

R_S and X_S are then obtained from equations :

$$R_S=\frac{R_P}{(1+Q^2)} \quad , \quad X_S = X_P \frac{Q^2}{1+Q^2}$$

For optimum operation of the Q-meter it was necessary to find as large as possible a value for (C_1-C_2) in order to obtain an accurate value for Q. As a result, measurements of Q were subject to inaccuracies at low frequencies because values of (C_1-C_2) were generally small, particularly with conducting (i.e. reduced) samples .

3.7.2 - Schottky diode studies:

3.7.2a - Temperature Dependent (I-V) Measurements :

Detailed point-by-point measurements of I-V characteristics as a function of temperature were carried out using a Keithley multimeter (model A195) (which provided a high impedance for voltage measurements and a low impedance

for current measurements). The bias voltage was derived from a calibrated DC supply (Time Electronics Ltd. Model 2003). The sample was maintained at the desired temperature using an Oxford Instruments DN1704 static He gas exchange gas liquid nitrogen cryostat controlled by an Oxford Instruments ITC4 temperature controller. Temperature was measured by a platinum resistance thermometer placed close to the sample while a second Pt resistance thermometer was used for temperature control. The measurements were taken between 77K and room temperature.

3.7.2b - Temperature Dependant C-V Measurements :

Capacitance - Voltage characteristics were measured manually using a Boonton 72B Capacitance meter, which operates at 1 MHz, with the sample mounted in the same cryostat as the I-V measurements. The DC bias was provided by a calibrated voltage source (Time Electronics Ltd Model 2003). Measurements were made at selected temperatures between 77K and room temperature. Steady state was assured by leaving the sample for at least a minute at each temperature (i.e. when no further change in the displayed values was seen) before taking the desired reading.

3.7.3 - Optical Transmission Measurements :

The optical transmission of thin film samples was obtained using a Perkin Elmer Lambda 19 spectrophotometer in the wavelength range 300 nm $\leq \lambda \leq$ 2500 nm. The Lambda 19 spectrophotometer has an all-reflecting, double - monochromator optical system, employing holographic gratings in each monochromator. Figure (3.14) shows the schematic for the optical system.

Two radiation sources, a deuterium lamp (DL) and a halogen lamp (HL), cover the working wavelength range of the spectrophotometer, and are selected automatically. The radiation is first passed through a double monochromator, to provide a highly collimated monochromatic beam. This is then devided into reference and sample beams, and the latter is passed through the sample. Transmission /

absorption in the sample is then measurred by comparing the sample and reference beams, thus any fluctuation in the beam intensities is automatically cancelled out.

The resulting transmission spectrum is displayed on a computer screen and may be downloaded to a digital plotter, if a permanant record is desired.

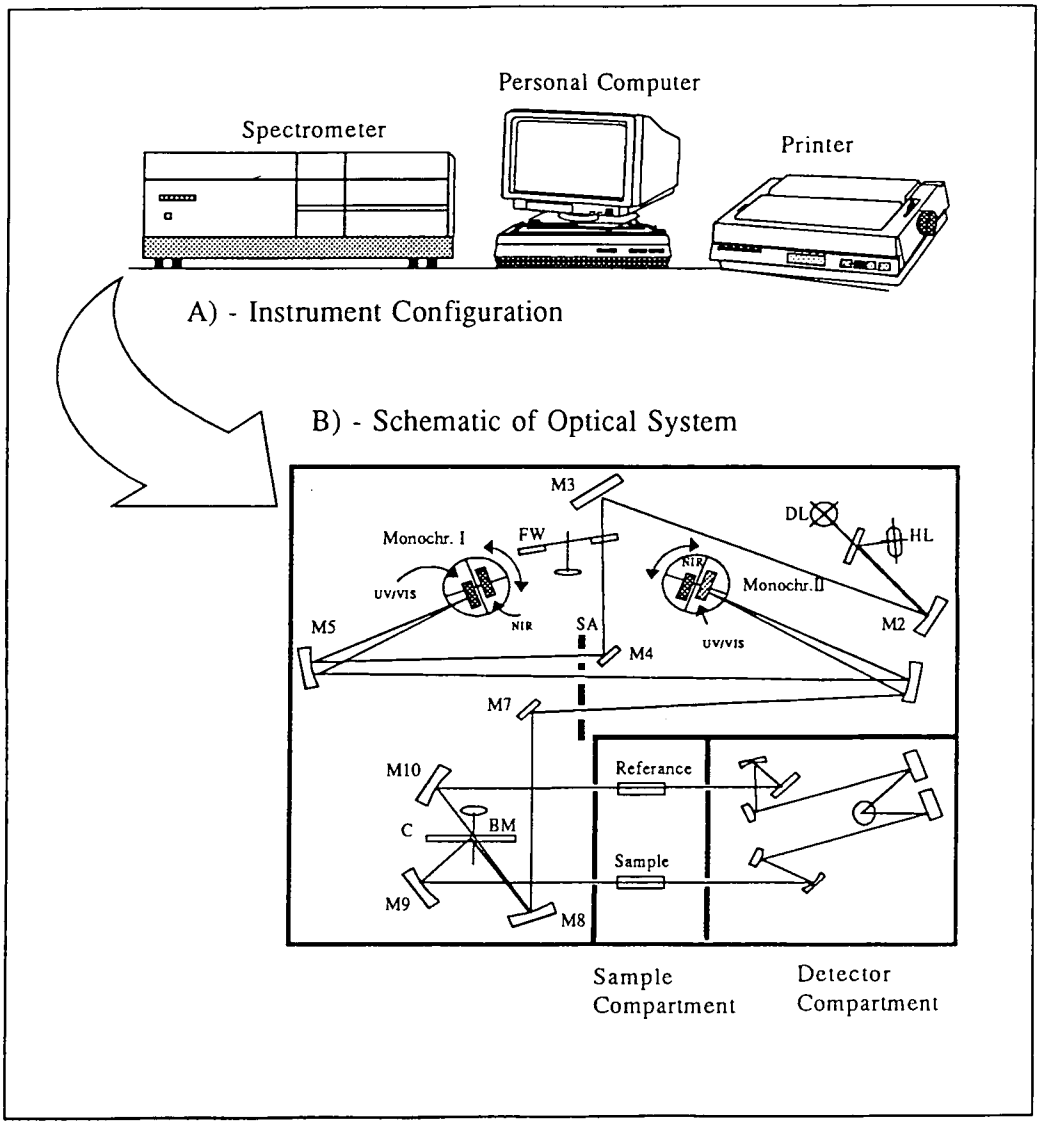

Figure (3.14) : Schematic of spectrophotometer system.

3.8 - References :

[3.1] - Eckertova L., "Physics of Thin Films" (second edition), Plenum Publishing Corporation and SNTL - Publishers of Technical Literature, Prague,43,(1986).

[3.2] - Holt D.B., Yacobi B.G.,"SEM Microcharactrization of Semiconductors", Academic Press, New York, (1989).

[3.3] - Goldstein J.I., Yakowitz H.Y., Newbury D.E., Lifshin E., Colby J. W., and Coleman,"Practical Electron Microscopy", Plenum Press, New York, (1975).

[3.4] - Goldstein J.I., Newbury D.E., Echlin P., Joy D. C., Fiori C. and Lifshin E.,"Scanning Electron Microscopy and X-ray Microanalysis", Plenum Press, New York, (1981).

[3.5] - Holt D.B., Muir M.D., Grant P. R. and Boswarva I. M.,"Quantitative Scanning Electron Microscopy", Academic Press, London, (1974).

[3.6] - Grundy P.J., and Jones G.A.,"Electron Microscopy in the study of Materials", Edward Arnold, London, (1976).

[3.7] - Russell G.J., Prog. Cryst. Growth Chara., **5**, 291 (1983).

[3.8] - Scherer A., Inal O.T., Thin Solid Films, **119**, 413, (1984).

[3.9] - Van Der Pauw L.J., Philips Research Reports, 13, 1 (1958).

Chapter IV

Undoped zinc stannate bulk material

4.1 - Introduction :

Ceramic di-zinc stannate, Zn_2SnO_4, as-sintered is an insulating material having an electrical conductivity of the order of 10^{-9} Ω^{-1} cm^{-1}. After a suitable heat-treatment in a reducing atmosphere, the conductivity increases dramatically towards 10^2 Ω^{-1} cm^{-1} and the colour changes from white to dark grey. The conducting material has been assessed for possible use for composite contacts [4.1], because of its good stability and conductivity.

In order to determine the conditions for the formation of the compound a series of sintering trials had first to be carried out. These were then followed by a sequence of heat treatments in a reducing ambient to investigate the relationship between the reduction process and the conductivity. Additional information was obtained from a limited number of thermal gravimetry (TG), differential scanning calorimetry and (DSC) experiments.

This chapter describes the preparation of as-fired and reduced zinc stannate, Zn_2SnO_4, and the results of the thermal analysis .

4.2 - Detailed Experimental Procedure :

4.2.1 - Sintering trials :

The zinc stannate, Zn_2SnO_4, was made from the solid state reaction at elevated temperature, between tin (IV) oxide, (SnO_2), and zinc oxide, (ZnO), as described in chapter III.

ZnO and SnO_2 powders of the highest commercially available purity were mixed in the ratio 2ZnO : 1SnO_2 either by ball milling or by pestle and mortar. The mixed powders were then heated in the temperature range, 1200°C < T < 1300°C, in

air, to form the compound, Zn_2SnO_4. Several heating rates between 60°C h^{-1} and 600°C h^{-1} were used, in order to determine the effects on the sintering behaviour. All samples were cooled down to room temperature at the natural cooling rate of the furnace, after it had been switched off. They were then examined by SEM and EDAX to assess sample porosity, grain size and composition. Powdered samples were examined using XRD to determine whether the material was monophase.

4.2.2 - Reduction Trials :

The zinc stannate samples were reduced by re-firing sintered samples in 25% H_2 / 75% N_2 atmosphere. A series of such reduction trials was conducted in which the samples were heated to temperatures in the range, 440°C ≤ T ≤ 450°C, for 14 hours. The reduced samples were then examined again by SEM and EDAX to determine whether there had been any change in the sample porosity, grain size and/or composition. Powdered samples were also examined using XRD to confirm that the material was still monophase and to ensure that the compound had not been reduced to the elemental metals. The resistivity - temperature characteristics were then measured to determine the optimum reduction heating temperature and time.

4.2.3 - Thermal analysis :

Thermal gravimetry (**TG**) and differential scanning calorimetry (**DSC**) measurements of an intimate stoichiometric mixture of zinc oxide and tin oxide were carried out in air up to 1400°C using a muffle furnace, in order to determine the reaction temperature. Sintered zinc stannate was then heated to 800°C in a mixture of 10% H_2 / 90% N_2 to find the temperature of reduction, i.e. the temperature at which a significant amount of oxygen was lost. Finally, reduced zinc stannate was re-heated in air to establish when the material was re-oxidized. All samples were heated and cooled at a rate of 10°C min^{-1}.

4.2.4 - Structure and Morphology :

The aim of examining samples with SEM throughout this work was to observe the microstructure of each sample, and then to obtain the average grain size. In addition, SEM observations were used to detect the presence of any second phase on the surface. Hence, most of the microscopy was performed using as-fired surfaces.

4.2.5 - Structure studies :

X-ray powder diffraction was used to investigate and confirm the formation of Zn_2SnO_4. Powder samples produced from crushed pellets were taken at every stage of both formation and reduction of the compound and assessed by XRD.

4.3 - Materials Processing :

4.3.1 - Sintering Trials :

All as-fired samples were uniformly white in colour, and well sintered pellets were strong and difficult to break. Typical XRD spectra from samples sintered at temperatures of 800°C, 1000°C and 1200°C are shown in figure (4.1) For comparison the XRD spectrum obtained from a sample of mixed (but unsintered) powders of SnO_2 and ZnO has also been included. Lines unique to Zn_2SnO_4 can just be discerned in the trace from the sample sintered at 800°C (note the {111} line at $2\theta \simeq 22°$). While these Zn_2SnO_4 lines are much more prominent in the XRD spectrum from the 1000°C sintered sample, lines due to unreacted ZnO (e.g. at $2\theta \simeq 37°$) and SnO_2 (e.g. $2\theta \simeq 32°$) are still present. It is only in samples sintered at the higher temperature of 1200°C that no evidence of unreacted SnO_2 and ZnO can be found. These results suggest that while the reaction to form Zn_2SnO_4 appeared to start at temperatures as low as 800°C it was only when the temperature was raised to 1200°C that the reaction went to completion in the timescale of the experiment (12 hours). The absence of other additional lines in this spectrum confirmed that the material was single phase.

The variation in the intensity ratio of ($I_{Zn_2SnO_4<311>}/I_{ZnO(2\theta=42.4°)}$) with sintering temperature

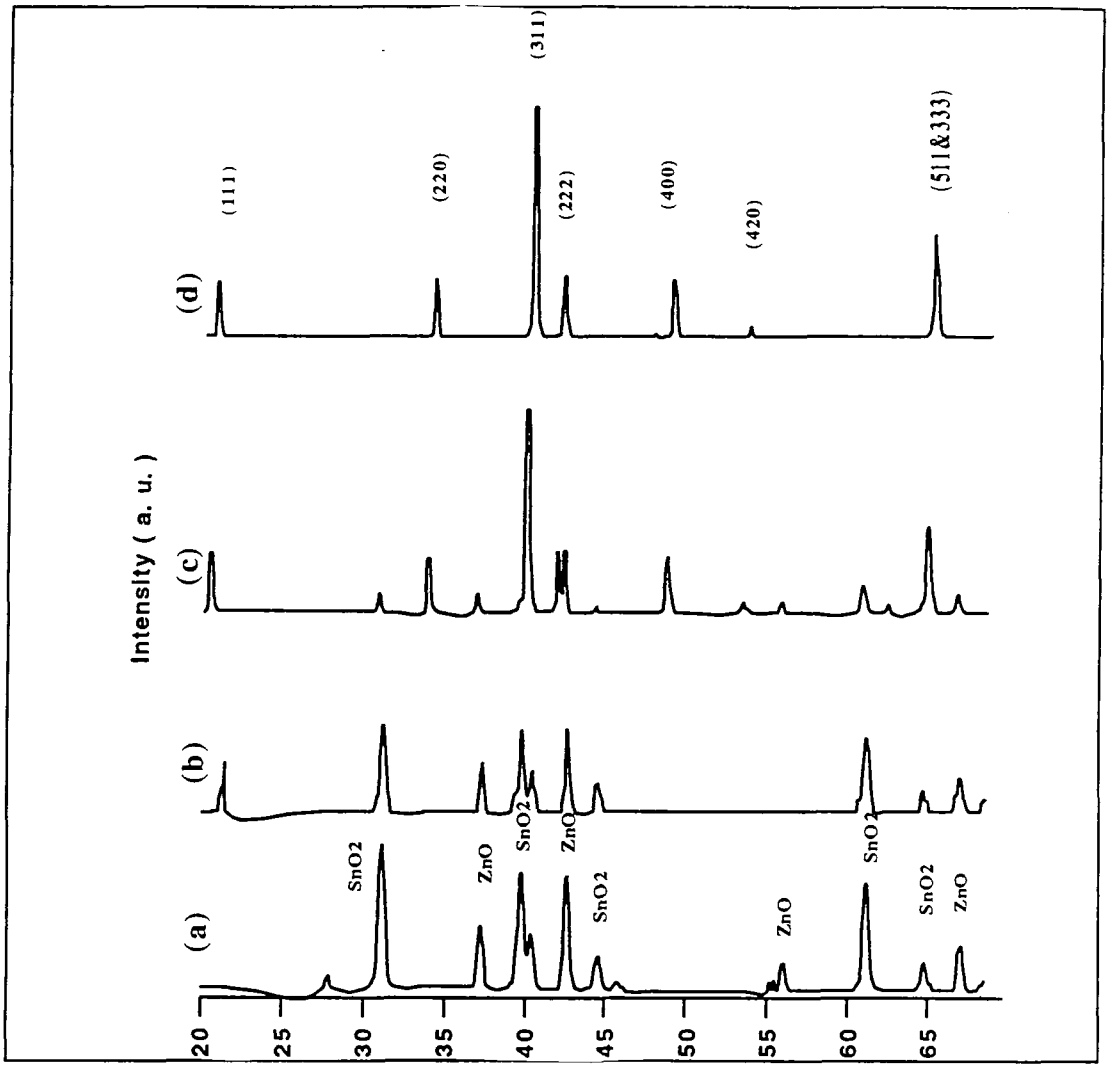

Figure (4.1) : X-ray diffraction patterns for zinc stannate : (a) starting material, (b) fired at 800°C, (c) fired at 1000°C, (d) fired at 1280°C.

is given in figure (4.2) and shows how the reaction progressed with temperature. This indicates clearly that significant compound formation started at ~ 1000°C. The XRD data from Zn_2SnO_4 are summarised in table (4.1), together with values taken from Filippova [4.2] for reference. The principal diffraction occurs from the {311} planes due to the face centred cubic with spinel structure of the material. Analysis of the X-ray data gave an estimate for the lattice parameter of Zn_2SnO_4 of a = 8.65 ± 0.006 Å. This compares favourably with other published values as shown

in table (4.2), confirming the integrity of the compound.

Table (4.1): Summary of X-Ray Diffraction Data for Zn_2SnO_4.

No.	Int.	d Å	h k l	d Å ref.[2]
1	21	4.99	1 1 1	5.01
2	22	3.05	2 2 0	3.03
3	100	2.61	3 1 1	2.59
4	21	2.50	2 2 2	2.49
5	25	2.16	4 0 0	2.17
6	2	1.76	4 2 2	1.76
7	32	1.66	5 1 1	1.65
8	34	1.53	4 4 0	1.51
Lattice constant a = 8.65 ± 0.006 Å				
Rad. CoKα with λ = 1.7902 Å , Fe filter				

Note : 2 ZnO : 1 SnO_2 fired at 1280°C for 12 hours.

Table (4.2) : Some published lattice constants for Zn_2SnO_4.

No.	Author(year)	lattice. con.	ref
1	Taylor (1930)	8.65±0.005Å	4.4
2	Frevel (1942)	8.63Å	4.5
3	Filippova(1960)	8.64Å	4.3
4	Yoshida(1976)	8.67 to 8.68Å	4.6
Present work a = 8.65 ± 0.006 Å			

The morphology of sintered samples was found to vary little with the sintering temperature for Ts ≤ 1300°C (see figure 4.3). Typically samples had grains ranging from 1μm to 15 μm in size. There was some evidence for the presence of a very small amount of glassy phase which had segregated to the surface in some samples where it appeared mostly in the spaces between grains. The glassy phase was revealed to be rich in zinc by EDAX.

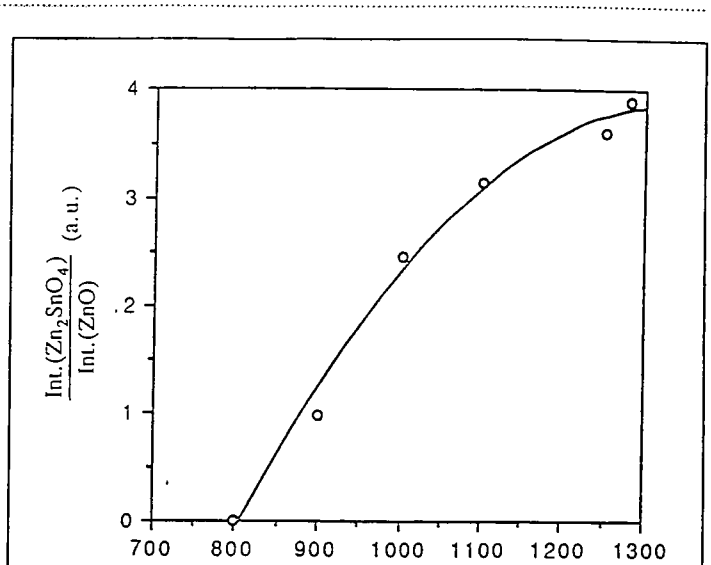

Figure (4.2) : The variation of Zn_2SnO_4/ZnO X-ray peak intensity ratio versus the firing temperature.

Heating rates seemed to be unimportant over the range tested. Comparing figures (4.3) (heating rate = 10°C min^{-1}) with figure 4.4 (heating rate = 5°C min^{-1}) shows there was little if any change in grain size or shape, although there was an increase in the size and density of intergranular pores in samples heated more rapidly. However, when samples were

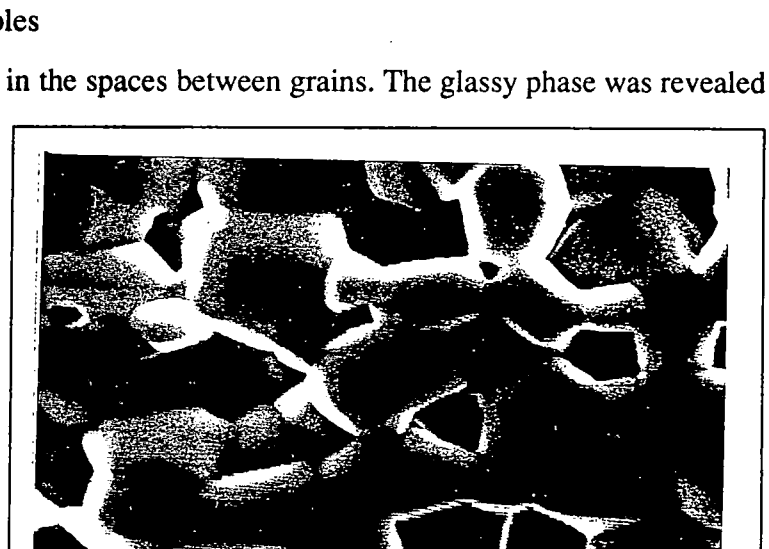

Figure (4.3) : Photograph showing grain sizes and pores for a sample heated at a rate ≥ 10°C min^{-1} to 1280°C.

sintered at temperatures ≥ 1450°C, black deposits become visible on the surfaces of grains, as shown in figure (4.5) When examined with EDAX figure (4.6), the deposits were found to be tin, indicating that some of the zinc had evaporated leaving tin on the surface. This suggests that at temperatures greater than 1450°C either the ternary Zn_2SnO_4 or the component binary oxides start to dissociate. The high vapour pressure of Zn would mean that little if any free Zn would remain on the surface of the sample at such elevated temperatures, explaining why only Sn is observed. Detailed comparison, using EDAX, of the composition of grain boundaries with the general surface, showed the grain boundaries were rich in zinc. This is evident from the EDAX spectra in figure (4.7), which shows a reduction in the

Figure (4.4) : Photograph showing grain sizes and pores, for a sample heated at a rate of 5°C min^{-1} to 1280°C.

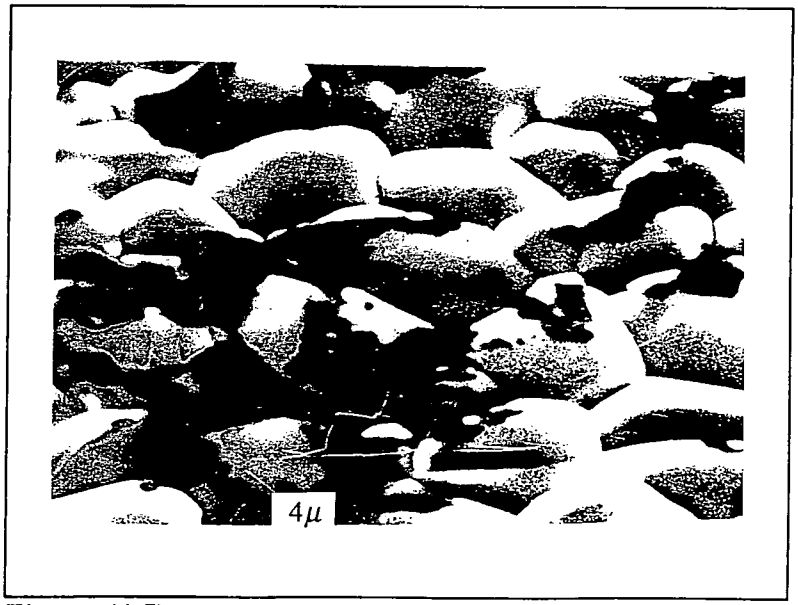

Figure (4.5) : Photograph showing strange deposits on the surface of a sample fired at T > 1300°C (for 12 hours).

Sn : Zn peak height ratio of about 50% in the grain boundary area. This was an interesting result which provided an insight into the mechanism of sintering and will be discussed more fully in the discussion section (4.4).

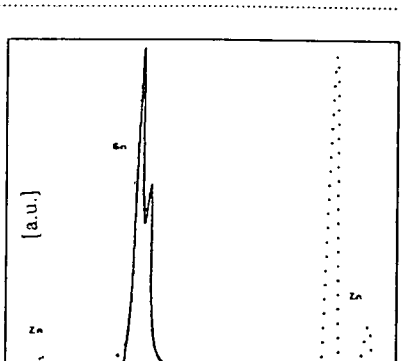

Figure (4.6) : EDAX spectra taken from sintered samples heated : (a) (solid line) To T > 1300°C, (b) (dotted line) T = 1280°C.

4.3.2 - Reduction Trials :

The zinc stannate samples were reduced by re-firing sintered samples in an atmosphere of 25% H_2 / 75% N_2. After a series of heat treatment trials it was found that a temperature of 440°C ≤ T ≤ 450°C for 14 hours was the optimum. These conditions avoided reduction of the compound to the metallic state as confirmed by the XRD in figure (4.8) which shows the XRD spectrum from a reduced (14 hours at 440°C) sample. Comparison with XRD spectra from the reduced and unreduced compound, show that the material had not undergone any change of phase or composition. Heating samples in reducing atmosphere to higher temperatures led to the reduction of some of the surface material to the metallic state. This is illustrated in figure (4.9) which shows that when the temperature was increased to 500°C, the surface of the sample became covered in metallic droplets with a small diameter of (~ 50 μm), shown by EDAX to be tin, while the surface beneath the droplet was found to be rich in zinc. A sequence of reduction trials was carried out at temperatures in the range 370°C - 600°C. The resulting pellets are shown in the photograph of figure (4.10). As grown, the samples were white, but gradually darkened

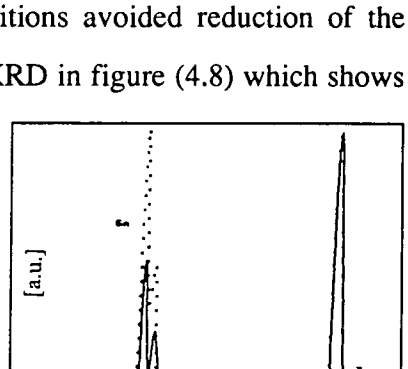

Figure (4.7) : EDAX spectra taken from a typical sintered sample : (a) (solid line) a typical pore, (b) (dotted line) general area scan. The sample was sintered at 1280°C for 12 hours.

as the temperature of reduction was increased to a dark charcoal grey when reduced at 440°C. At 550°C the metallic droplets become visible to the unaided eye and were

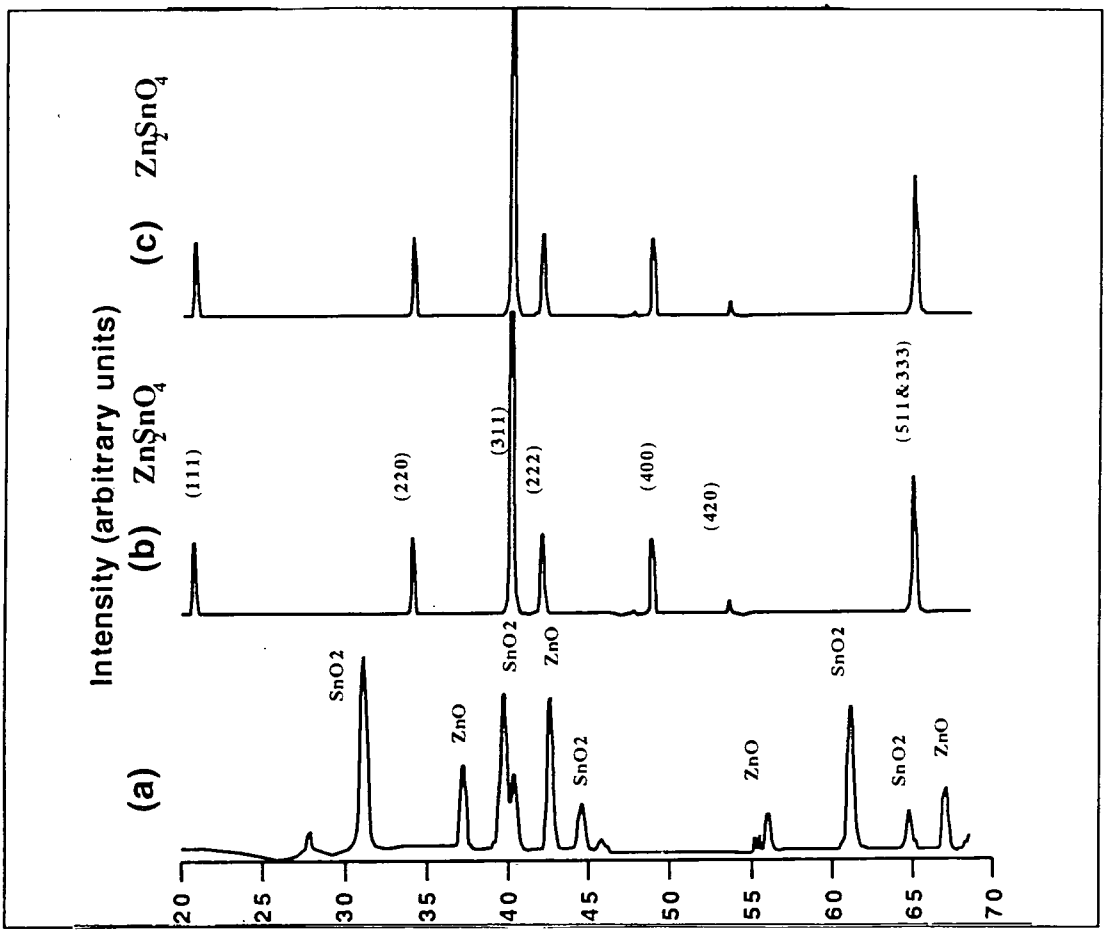

Figure (4.8) : X-ray diffraction patterns for zinc stannate : (a) starting material, (b) as-fired, (c) reduced sample.

accompanied by a corresponding reduction in the physical size of the sample. It was found that the samples lost 0.016 grams in weight as a result of heating to 500°C in a reducing atmosphere for 14 hours, and 0.001 grams for a sample heated to 350°C for the same time, which it has been assumed was due to loss of O_2 only. A graph showing the molar ratio of O_2 loss with reciprocal reducing temperature is shown in figure (4.11). This clearly shows thermally activated behaviour with an activation energy E_a of 82.4 kJ mol^{-1}. It is not clear how typical this value of the activation energy is for such ceramic oxides, but it is an indication of the degree to which

reduction/oxidation processing may be carried out in this material. The activation energy is sufficiently large to ensure room temperature stability and reduced samples will not reoxidise in air at that temperature. Indeed the DSC/TG (thermal analysis) measurements (discussed below) suggest that re-oxidation only occured at relatively high temperatures (T≥500°C) in air.

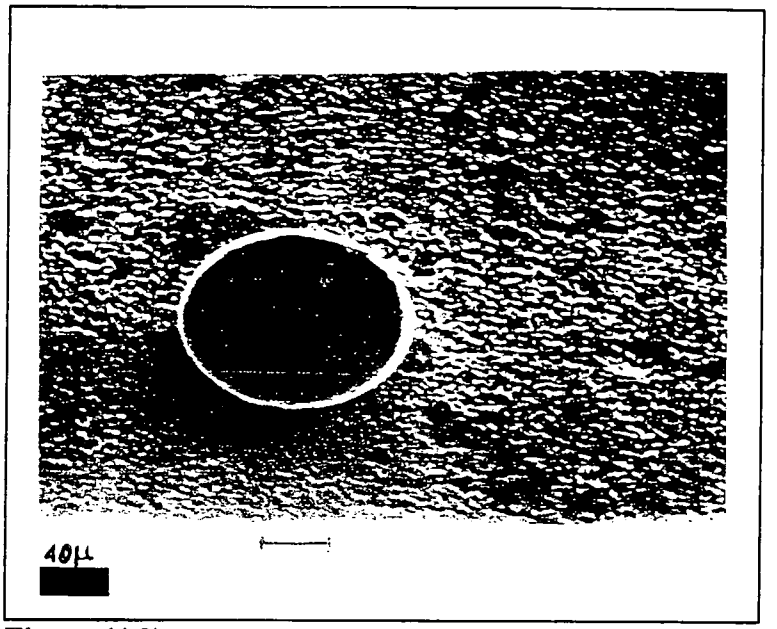

Figure (4.9) : Photograph showing a metallic droplet on the surface of a sample annealed at T > 500°C for 14 hours.

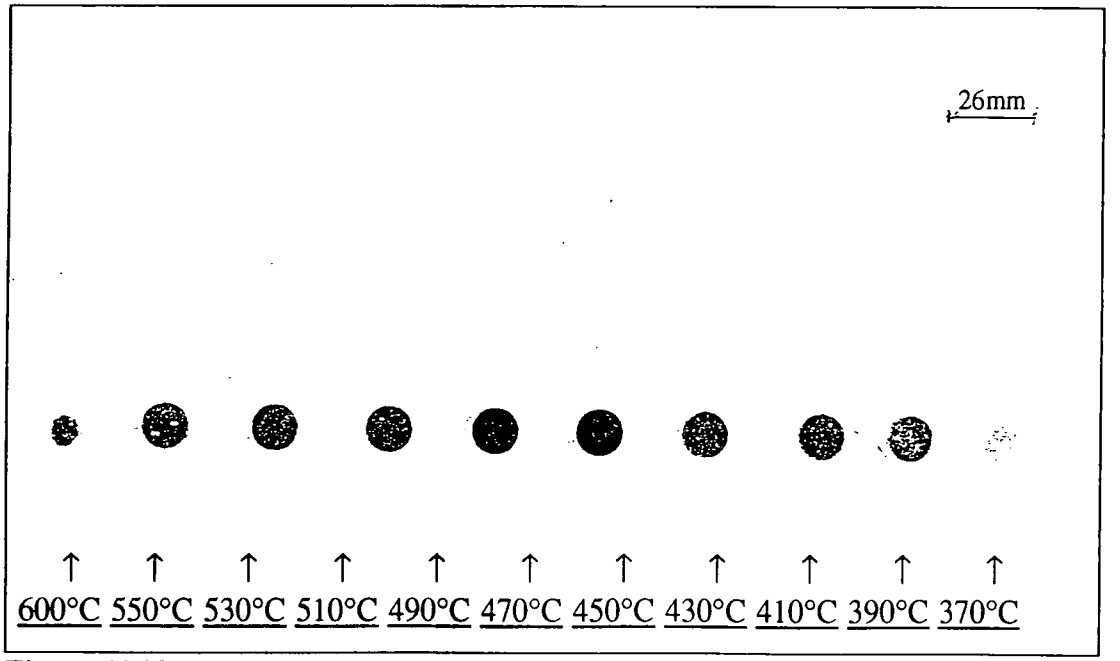

Figure (4.10) : Photograph showing the colour changes with increasing reduction temperature. Metallic droplets appear on the surface at 550°C.

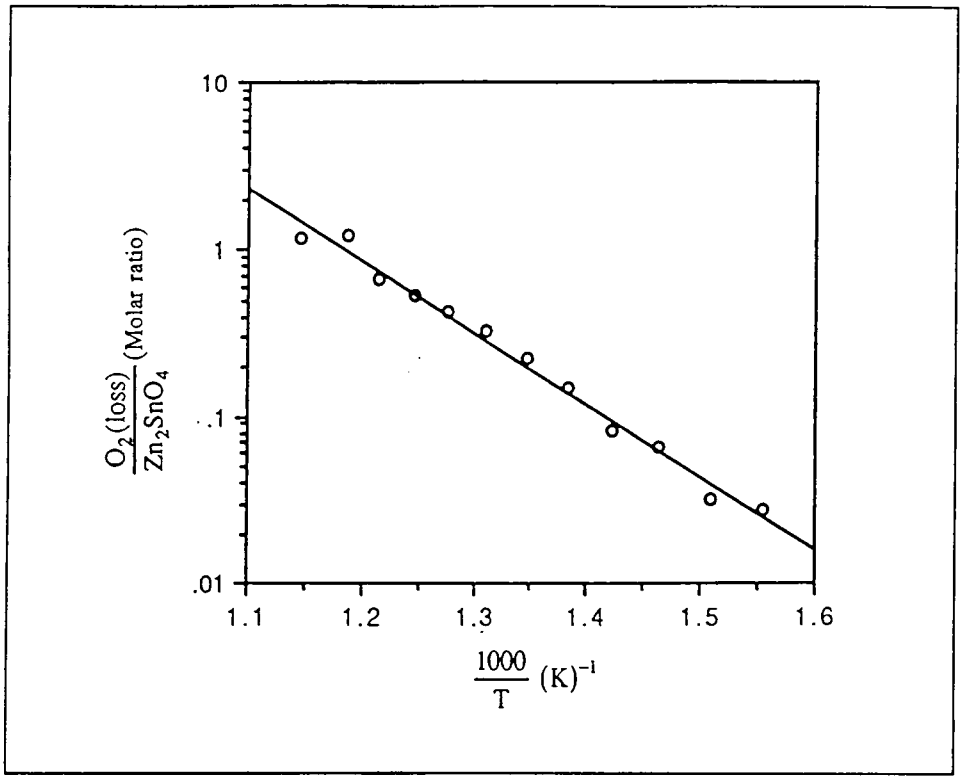

Figure (4.11): The amount of O_2 loss during reduction of Zn_2SnO_4 versus the heating temperature.

4.3.3 - Thermal Analysis :

The **TG** and **DSC** characteristics for a mixture of 2ZnO : $1SnO_2$ heated in air to a temperature of 1400°C are shown in figure (4.12). The **DSC** curve has a small broad peak at ~ 450°C - 550°C probably due to the burning away of carbon-containing impurities, and a narrower peak at 1058°C , indicative of compound formation. The **TG** results show a small weight loss at ~ 450°C, although significant weight reduction does not begin until the temperature is above 1150°C when preferential loss of zinc oxide starts to take place. This is in agreement with the results of the sintering trials (4.2).

Figure (4.13) shows the **TG** and **DSC** curves for the sintered material under heat-treatment up to 800°C in the reducing atmosphere. The **TG** curve shows significant weight loss occurring above 600°C, when the loss of oxygen accompanying reduction

to the metal becomes substantial. The **DSC** curve , on the other hand is featureless, demonstrating that no reaction or phase change had taken place. Note that these trials were carried out in 10% H_2 / 90% N_2, whereas most reduction trials (section 4.3.2) were undertaken in (25-30)% H_2 / (70-75)% N_2. SEM examination of samples that had been annealed in 30% H_2 / 70% N_2 atmosphere, revealed that they were reduced to their metallic states at the lower temperature of 500°C as a result of the higher concentration of H_2 (section 4.3.2). Re-oxidation of samples which had been previously annealed at 440°C in 30% H_2 / 70% N_2 was found to take place at 500°C , as shown by **TG** , DSC and **DTG** results in figures (4.14 , 4.15). These curves show a small feature at ~ 220°C and a much larger feature at ~ 550°C which is probably associated with re-oxidation of the reduced sample and was accompanied by a change of colour from black to white. The origin of the features at 220°C and

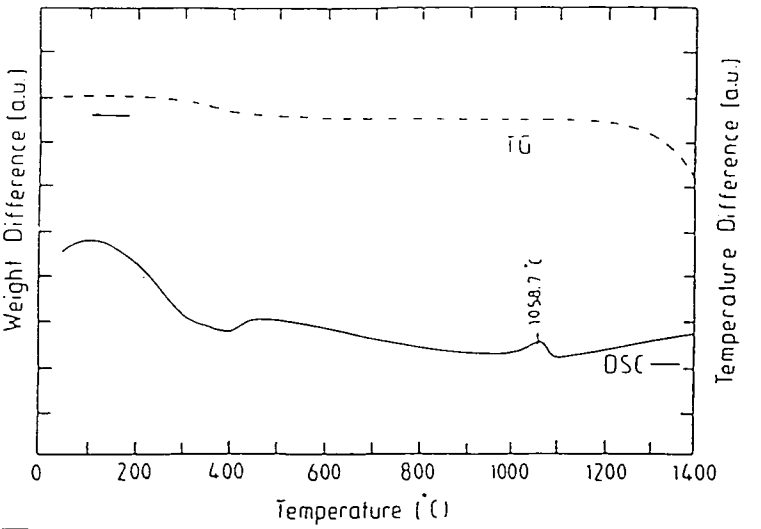

Figure (4.12) : Thermal gravimetry (TG) and differential scanning calorimetry (DSC) for a 2ZnO : SnO_2 mixture, heated in air.

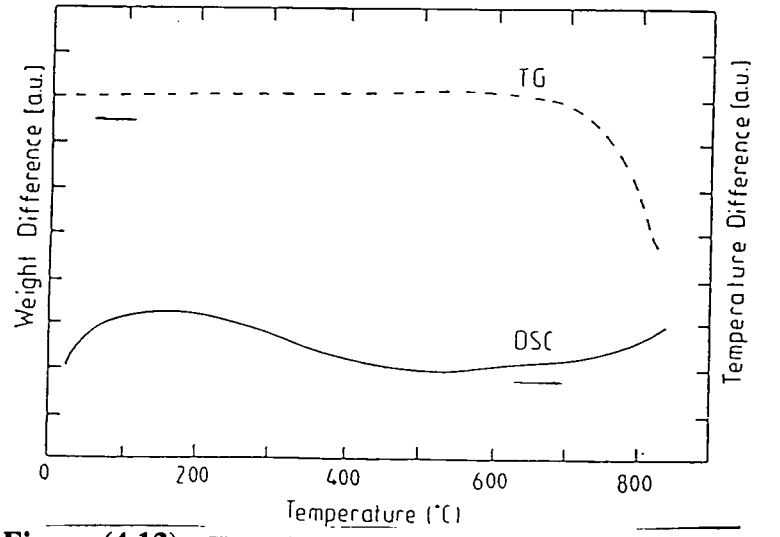

Figure (4.13) : Thermal gravimetery (TG) and differential scanning calorimetry (DSC) for as-fired Zn_2SnO_4, heated in 10% H_2 / 90% N_2.

350°C is not known, but may also be associated with changes in the oxidation state of the compound.

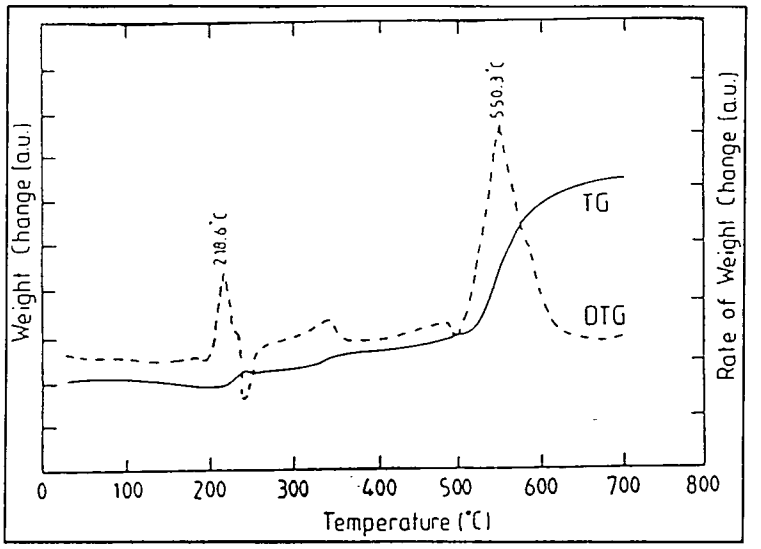

Figure (4.14) : Thermal gravimetery (**TG**) and differential thermal gravimetry (**DTG**) for reduced Zn_2SnO_4, heated in air.

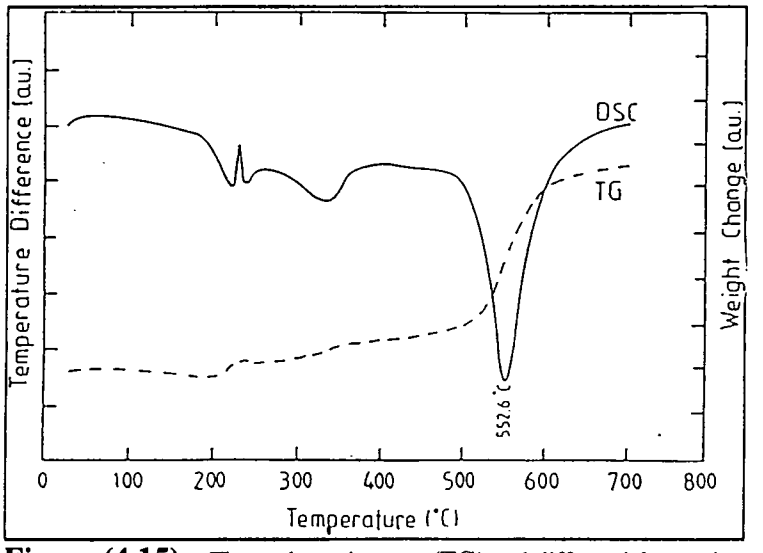

Figure (4.15) : Thermal gravimetery (**TG**) and differential scanning calorimetry (**DSC**) for reduced Zn_2SnO_4, heated in air.

4.4 - General discussion :

4.4.1 - Compound formation :

From the results presented in this chapter it is clear that the optimum firing temperature to form zinc stannate was about 1280°C. The present work has also confirmed that the solid state chemical reaction between $1SnO_2 : 2ZnO$ starts relatively slowly at about 900°C to form Zn_2SnO_4; this result is, to some extent, in conflict with Tazaki et al (1951) [4.6], who concluded that zinc stannate could not be obtained below a temperature of 900°C. However, this would depend on the heating time, which in their case was much shorter than ours (60 min. as against 12 hours). The complete reaction of the compound without any additional phase was shown in the present sudy to be obtained when stoichiometric mixtures were heated at 1280°C for 12 hours as described in section (4.2.1).

These results which were confirmed by SEM, EDAX, and X-ray diffraction, are in close agreement with previously reported work [4.3,4.7,4.8], for example, Kostolov et al. (1958) [4.3] reported that zinc stannate could be formed from a mixture of zinc oxide and tin oxide at a temperature of 1300°C for 20 min. They also concluded that zinc oxide began to react with tin oxide at temperatures above 800°C. Similar findings were obtained by Filippova (1960) [4.2] (T = 1200°C), Shimada (1976) [4.9] (T = 1300°C), Zuyao (1987) [4.10] (T = 800°-1500°C), and Hashemi (1990) (T = 1280°C) (see section 1.4).

When firing was carried out at a higher temperature (T ≈ 1400°C) it was found that the compound was rich in SnO_2, this possibly caused by preferential evaporation of zinc oxide from the sample surface leaving it deficient in Zn as shown in the photograph figure (4.5) and by the EDAX results in figure (4.6). This result is in agreement with Glot and Nadzhafzade (1991) [4.11], who found SnO_2 residue in their samples when fired at higher sintering temperatures (T ≈ 1520°C).

Heating rate was found to affect the surface morphology of the sample, and of the heating rates tried (60°C h^{-1} ≤ rate ≤ 600°C h^{-1}), the best was found to be 60°C h^{-1} (5°C min^{-1}) which gave samples with fewer and smaller pores. In addition, the peak height ratios of Sn and Zn in EDAX spectra were comparable to those obtained from homogenous mixtures of the constituent ZnO and SnO_2 powders,(i.e. indicating better stoichiometry), in agreement with Hashemi (1990) [4.7]. Generally heating rate did not appear to affect the structure, as observed in the XRD patterns of powdered samples fired with different heating rates. The pores in all sets of samples appeared to be slightly rich in zinc, as shown in figure (4.7), again in agreement with results in [4.2,4.3,4.7]. The pores are assumed to be created as a result of the evaporation of ZnO, at points where SnO_2 was not available for reaction, possibly because of incomplete mixing, as suggested by Hashemi et al. [4.7]. The mean grain size (determined from area counts assuming spherical grains) varied from ~ 5.5μm diameter when the heating rate was 600°C h^{-1} to ~ 8μm diameter when the lower heating rate of 60°C h^{-1} was used.

The as-fired compound was white in colour and highly resistive ($\rho \geq 10^9$ Ω cm), though not a complete insulator, since it was possible to observe the surface morphology in the SEM without the need for gold coating.

4.4.2 - Sintering :

Sintering is a term commonly used to describe coalescence of solid powder particles at elevated temperatures and comprises three principal stages, neckgrowth (joining of particles together), densification (with the formation of interconnecting pore channels) followed by spheroidal shaping and isolation of pores as described by Thummler (1967) [4.12]. These stages of sintering result in bonding together of particles and ultimately, to the removal of internal porosity, causing external shrinkage and the achievement of desirable physical properties. The major importance of sintering processes in the formation of ceramics and in powder metallurgy, has made

these processes the subject of considerable research effort [4.12-4.14]. The sintering mechanisms by which particles may unite are described in section (2.2).

During the normal processing of ceramics, crystalline or non crystalline powders are compacted and then fired at a temperature sufficient to form the desired compound, where during the sintering process changes may occur initially because of decomposition or phase transformation in some of the phases present. There are many aspects of concern, but the major changes which may occur are in grain size, pore shape, pore size, and pore number.

In the present case the reaction was thought to take place mainly by solid state chemical reaction as mentioned in section (4.4.1). In this study which was concerned with the best way to understand and then interpret the sintering mechanism the important variables of concern were grain growth, densification of the single phase system and finally multiphase processes [4.15a].

The diffusion sintering mechanism is considered one of the major sintering mechanisms in single-phase ceramics, e.g. magnetic and ferroelectric ceramics [4.16], Such diffusion involves the movement of atoms and the counter movement of lattice vacancies, and is known to be strongly affected by temperature and ambient atmosphere. As discussed earlier (section 2.2.1), the difference in free energy or chemical potential between the neck area and the surface of the particle provides a driving force which causes the transfer of material by the fastest means available. If the vapour pressures are low this may occur more readily by solid state processes.

In the present case, zinc can diffuse into SnO_2 in three ways, interstitially, substitutionally or through vacancies. It is generally believed, that there is a relatively large concentration of interstitial zinc ions, Zn_i, in ZnO that are free to diffuse through the lattice. SnO_2 exists in a metal [4.15b] in which Sn ions occupy only half the available octahedral sites. There are generally large concentrations of O in SnO_2 (especially at high temperatures where equilibrium vacancy concentrations are high) and the requirements for electrical neutrality result in a combination of Sn vacancies

together with mixed Sn valence states (Sn^{2+}, Sn^{4+})[4.15b]. There are therefore, many sites, both interstitial and substitutional, for the in-diffusing Zn to occupy.

Both the concentration of Zn_i ions and their mobility are strongly dependant on the temperature [4.16b]. Our experience suggests that it is only above a certain temperature (1000°C) that these processes are sufficiently rapid to take place in the timescale of the experiment (12 hours).

In addition to solid-state diffusion it is possible that an evaporation-recondensation mechanism may have been important. In this mechanism, material transfer occurs as a result of the differences in surface curvature and consequently the differences in vapour pressure at various parts of the system (see section 2.2.1). When two adjacent particles in the powder compact are just beginning to sinter. The surfaces of the particles have a positive radius of curvature so that the vapour pressures are somewhat larger than would be observed for a flat surface. However, just at the junction between the particles, there is a neck with a small negative radius of curvature and a vapour pressure an order of magnitude lower than that for the particle itself. Then material can be transferred into the neck area as result of the vapour pressure differences between the neck and the particle surfaces.

As pointed out above, the pores were found by EDAX to be rich in zinc and this would be consistent with an evaporation-condensation sintering process. This may be understood in terms of the evaporation of zinc at points where Sn was not available for chemical reaction due to incomplete mixing, as discussed previously. On cooling, the zinc vapour would condense on the walls of the pores leading to the observed Zn-rich surfaces. If this interpretation is correct, then it can be taken as evidence that zinc vapourisation was occurring, and if this was so, then sintering by evaporation-recondensation would also been expected to have taken place.

The size and shape of pores were found to be dependant on the heating rates (see figures 4.3,4.4). In particular, heating rates that were too fast led to a higher incidence of pores that were comparable in size to the grains. This was probably due

to the zinc evaporating away from the surface, before it had time to react with the tin oxide. When the heating rate was less rapid, zinc loss was reduced because the temperature throughout the sample was more uniform. Thus material sintered with heating rate ≤ 5°C min.$^{-1}$ displayed lower concentrations of pores with a smaller mean size. This effect was more pronounced on the surface where zinc loss was greater. In the sample bulk, pore densities were lower, and smaller since the zinc was effectively trapped and prevented from escaping. This was true even when the highest sintering temperatures were used and when zinc loss from the surface was significant, indicating, that grain growth was sufficiently rapid in the bulk to prevent pore formation there even at the highest temperatures.

4.4.3 - Reduction behaviour:

As-fired Zn_2SnO_4 samples were insulating and were white in colour, with an electrical conductivity of the order of 10^{-9} Ω^{-1} cm^{-1}, On the other hand, samples fired in a reducing atmosphere were electrically conductive having conductivities of the order of ≈ 10^2 Ω^{-1} cm^{-1}, (The electrical properties will be discussed in more detail in the next chapter). As reported earlier, the reduction also led to change in colour from white to black. It is clear through figure (4.9) that the colour was beginning to change at a reducing temperature of 370°C and was eventually complete when the temperature was 430°C (for a heating time of 14 hours). Heating in a reducing ambient should lead to a preferential loss of oxygen from the Zn_2SnO_4. The resulting loss of stoichiometry in the compound would result in conversion of the tin from the tetravalent to the divalent state in order to preserve charge neutrality ($O^{2-} \rightarrow V_o^{\cdot\cdot}$, $Sn^{4+} \rightarrow Sn^{2+}$). Divalent tin compounds are generally black and the observed colour change is a good indication that this is what had happened. The associated oxygen vacancies will act as donor centres [4.17], resulting in the observed decrease in the resistivity. The reduction process can be represented formally as [4.18]: $Zn_2^{2+}Sn^{4+}O_4 - xO \rightarrow Zn_2^{2+} + Sn_{1-x}^{4+}Sn_x^{2+}O_{4-x}$

Clearly if oxygen loss is too great, then the compound will start to decompose to its metallic constituents as was observed when reduction temperatures ≥ 500°C were used. It was found that the oxygen loss ratio (in mol.) varies from 0.024 to 0.204 as the reduction heating temperature was increased from 350°C to 500°C with an activation energy for the process of Ea = 82.4 KJ mol^{-1}. It is worth noting, that the density of O_2 vacancies will be very large and it is therefore not surprising that the conductivity could be increased by many orders of magnitude as a result.

4.5 - Summary :

In summary zinc stannate was prepared from the solid state reaction of ZnO and SnO_2 powders using oxides of the highest commercially available purity. The compound began to form at 900°C, but the x-ray diffraction spectra showed that monophase compound formation could not be achieved at firing temperatures below 1280°C (12 hours with a heating rate of 5°C min^{-1}). This was also found to be the optimum formation temperature from the thermal analysis measurements.

Exceeding the optimum sintering temperature resulted in the decomposition of the compound as revealed by SEM which showed that the surface began to be Sn-rich at 1300°C. The material disappeared completely at about 1500°C. The sintering mechanism was thought to be primarily due to an evaporation - recondensation process involving the zinc.

The zinc stannate compound was white in colour, and well sintered pellets were strong and difficult to break, and electrically insulating. After suitable heating treatment in a reducing atmosphere, the colour changed from white to grey/black and the conductivity increased dramatically to about 10^{-2} Ω^{-1} cm^{-1}. However, heating the sample in reducing atmosphere at too high a temperature led to reduction of some of the surface material to the metallic state. This was shown by EDAX where some tin metallic droplets were obseved on the surface of samples reduced at high temperature (T ≥ 500°C), while the surface beneath the droplets was found to be rich in zinc.

Weight loss measurements indicated that the activation energy of reduction was 82.4 kJ mol^{-1}, which is thought to be sufficiently large to ensure the stability of the reduced compound (i.e. the reduced sample will not re-oxidise in air at room temperature).

TG/DSC studies for a refired, reduced sample implied that the re-oxidation of samples which had been previously reduced at 440°C would take place at 500°C.

4.6 - References

[4.1] - Sumitomo Electric Industries, Kokai Tokkyo Koho, **JP 83 35**, 71, (1983).

[4.2] - Filippova N. A., Savina E. V. and Korosteleva V. A., Russian J. Inorg. Chem. **5**, 691 (1960).

[4.3] - Kostolov V. V., Morachevskaya V. S. and Gipronikel. Nonferrous Metals (Moscow), **31**, 39 (1958).

[4.4] - Hashemi T., Hogarth C. A. and Golestani-Fard F., J. Mater. Sci. **23**, 2645 (1988).

[4.5] - Frevel L. K., Industrial and Engineering Chemistry, Vol. **14**, 687, (1942).

[4.6] - Tazaki H. and Kuwabara, J. Scie. Hiroshima Univ., **15**, 133, (1951).

[4.7] - Hashemi T., Al-Allak H.M., Illingsworth J., Brinkman A.W. and Woods J.,J. Mater. Sci. Lett., **9**, 776, (1990).

[4.8] - Huang S., Sumita S., Morinaga K. and Ynagase T, Nippon Kogyo Kaishi, 100(1162), 1145,(1984).

[4.9] - Shimada S., Kodaira K and Matsushita, Japan. Chem. Lett., pp 235 (1976).

[4.10] - Zuyao C., Ying J., Zude Z. and Yitai Q., J. China Univ. Sci. Technol.**17**, 343, (1987).

[4.11] - Glot A. B., Proshkin Y. N. and Nadzhafzade A. M., "Ceramics Today - Tomorrow's Ceramic", Elsevier Science Publishers B. V., Amsterdam,(1991).

[4.12] - Thummler F. and Thomma W., Mater. Rev., **12**, 69 (1967).

[4.13] - Coble R. L. and Burke J. E., Prog. Ceram. Sci., **3**, 197 (1963).

[4.14] - Aller A. J.,Ceram. Ind. J., 39 (1986).

[4.15] - a) Kingery W.D., Bowen H. K. and Uhlmann D. R. "Introduction to ceramics 2nd ed." (A Wiley-Interscience (1976). New York). b) - ibid p64. c)- ibid p485

[4.16] - a) Van Vlack L.H.,"Physical Ceramics for Engineers" (Addison-Wesley, New York (1964). b)ibid p 94.

[4.17] - Jian L., Vizkelethy G. and Mayer J. W., Appl. Phys. Lett. **58 (12)**,1344, (1991).

[4.18] - Illingswoth J., Hashemi T., Al-Shahrani A. and Brinkman A W., Brit. Ceram. Proc. 49, Special Ceramics, London, 241, 9,(1990)

CHAPTER V

ELECTRICAL MEASUREMENTS OF UNDOPED MATERIAL :

5.1 - Introduction :

As mentioned in chapter IV, as - fired Zn_2SnO_4 usually had a very high resistivity and it was not possible, therefore, to make electrical measurements without first treating the compound in some way.The conductivity could be changed from 10^{-9} Ω^{-1} cm^{-1} for as fired samples, to $\sim$ $1x10^{-2}$ Ω^{-1} cm^{-1}, by the reducing treatment in H_2 / N_2 ambient already described in chapter IV. This chapter therefore will be primarily concerned with investigations of the electrical characteristics of such undoped reduced samples. The intention is to know and understand more about the conductivity behaviour, and mechanisms.

Both transport (R-T & Hall) and dielectric (a.c. impedance) measurements were carried out, to try and determine current transport mechanisms in the bulk. The behaviour of the contacts was tested by (I-V) measurements, to ensure there was no barrier between the contact and the sample. This would show as a variation in resistance with applied voltage. In principle, transport measurements enable the carrier density to be determined and the scattering mechanisms to be studied. The a.c. impedance measurements provide information on the influence of the grain boundaries on current transport.

5.2 - Sample preparation and contacts :

Measurements were carried out on Zn_2SnO_4 pellets that had been sintered at 1280°C for 12 hours and then annealed at 440°C for 14 hours in H_2/N_2 (25% : 75%) ambient. In addition some reduced samples were re-fired in air at 600°C for 12 hours, in order to increase the resistivity to $\sim$ 200 Ω cm. This was necessary for the a.c. impedance measurements, where the reduced samples were too conducting. Generally

the pellets were polished with alumina powder down to a grit size of about 1μm, and then etched in 1(HF) : 1(HNO_3) : 4(CH_3COOH) to remove any surface damage, as well as metallic residues. Ohmic contacts were then obtained using an In/Ga alloy. Both In and Ga are relatively low work function metals and should give barrier - free low resistance contacts to an n-type semiconducting material such as Zn_2SnO_4. (The n-type nature of zinc stannate was revealed using Seebeck effect, and Hall voltage measurements).

A series of current - voltage measurements were made to confirm that the contacts were ohmic and were not limiting the current. In order to minimise any self - heating effects, the measurements were made using voltage pulses of short duration. A known resistance was connected in series with the sample, and the voltage across the resistance was measured, using a digital storage oscilloscope, and used to calculate the current through the sample. Further details about the measurements have been described earlier in chapter III. Every sample was observed to give ohmic behaviour, as shown in figure (5.1). This is a typical plot of ℓog R_s versus applied voltage U, for an un-doped sample, reduced normally then re-fired in free air at 600°C for 12 hours.

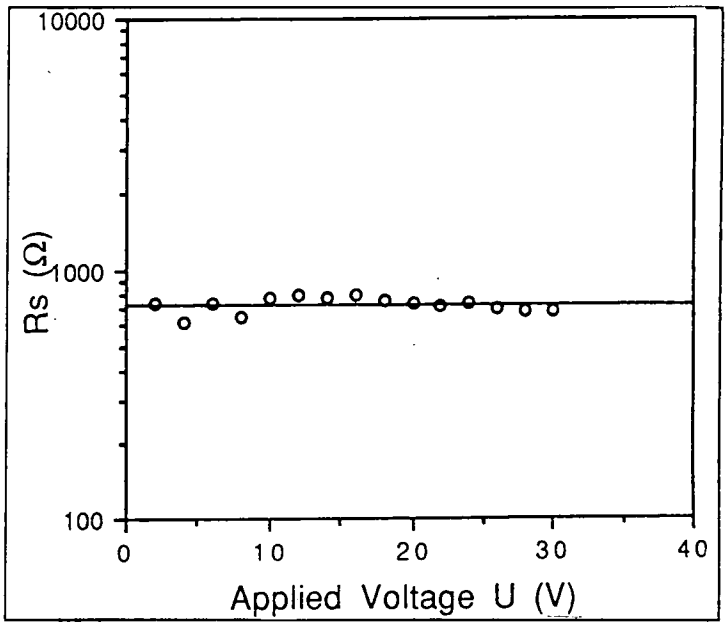

Figure (5.1) : Normalised resistance versus applied voltage.

5.3 - D.C. Transport measurements :

5.3.1 - Conductivity - Temperature characteristics :

A typical series of plots of conductivity versus temperature, between 77K and 300K, are shown in figure (5.2), for samples annealed at different temperatures from 420°C to 450°C, in 25% H_2 / 75% N_2 gas, for 12 hours as described in chapter IV. Plotting $\ell n(\rho)$ (where ρ is the sample resistivity) at particular temperatures versus reciprocal *annealing* temperature gave the graphs in figure (5.3), which were used in an attempt to estimate the activation energy for the annealing processes. It was found that the slopes decreased with increasing measurement temperature from 6.44 x 10^{+4} Ω cm K, at 80K to 3.23 x 10^{+4} Ω cm K, at 280K. This suggested that either the resistivity was not

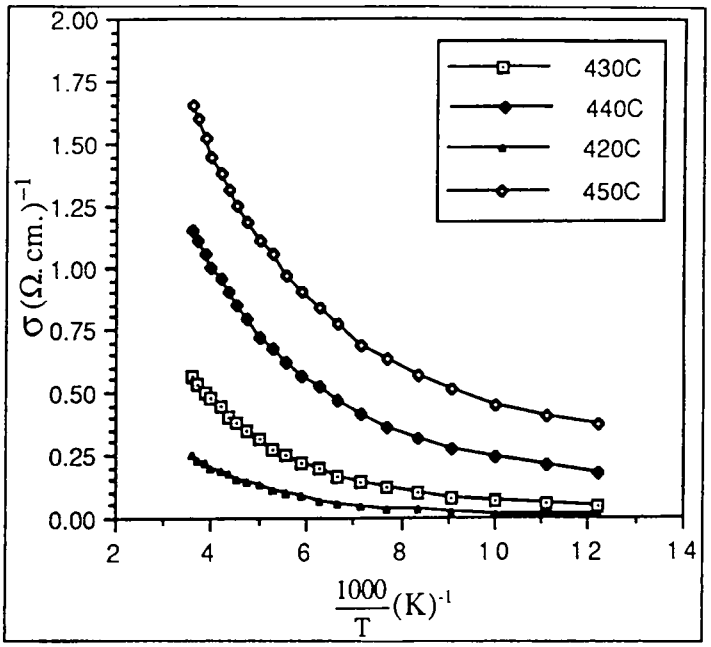

Figure (5.2) : Conductivity versus 1/T from 77K to room temperature, for samples annealed in the temperature range 420°C to 450°C.

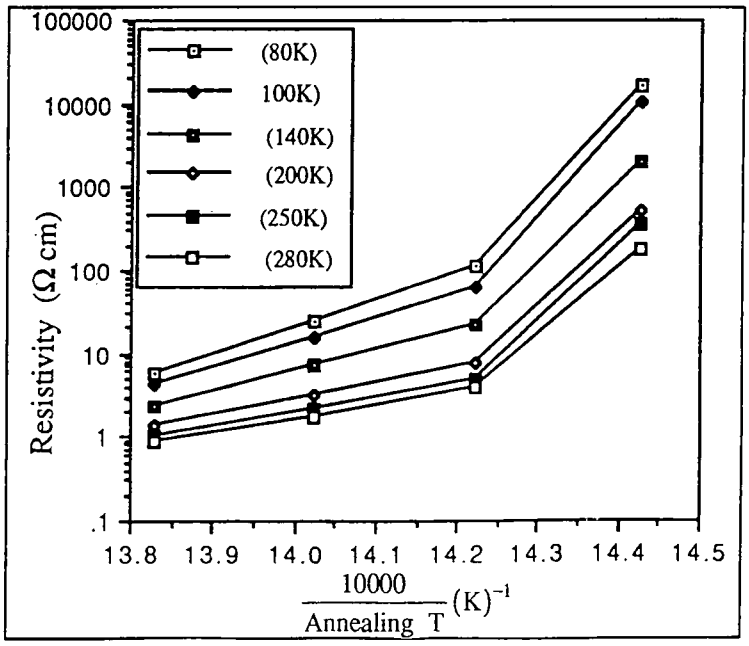

Figure (5.3) : Resistivity versus reciprocal annealing temperature.

directly proportional to the carrier density or that the creation of donors (i.e. Oxygen vacancies) through the annealing process was not a simple thermally activated process. There was, also, a change in the slope of the resistivity - temperature characteristics at high annealing temperature, which may have been due to the onset of reduction of the material to the metallic state.

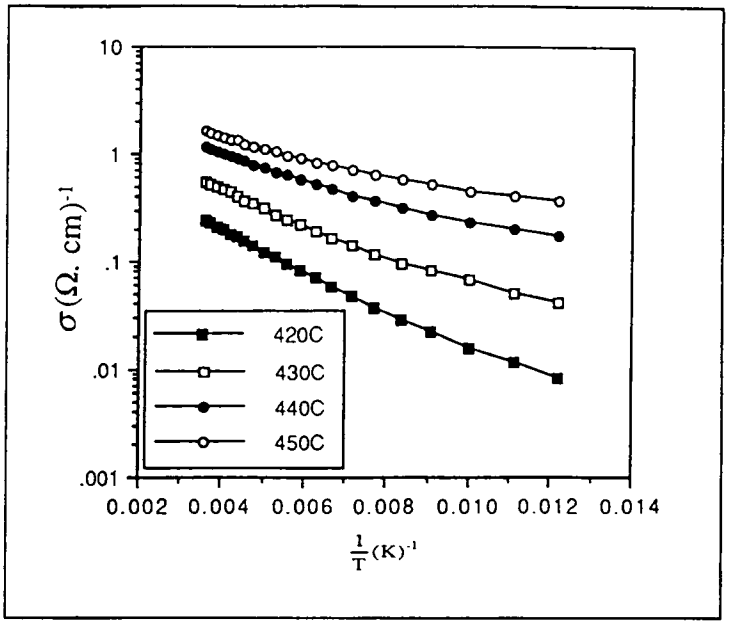

Figure (5.4) : Log σ versus 1/T, for samples annealed at different temperatures (as labelled in the graph).

It can also be seen from figure (5.2) that the conductivity increased with increasing measurement temperature, which is typical of semiconductor behaviour. However, when plotted on ℓn σ_{DC} versus 1/T axes the data were found to lie on a concave curve (rather than a straight line), showing that the conductivity was not of the simple activated form $\sigma \propto \exp[-\varepsilon_a/kT]$ (see figure (5.4)). The curvature

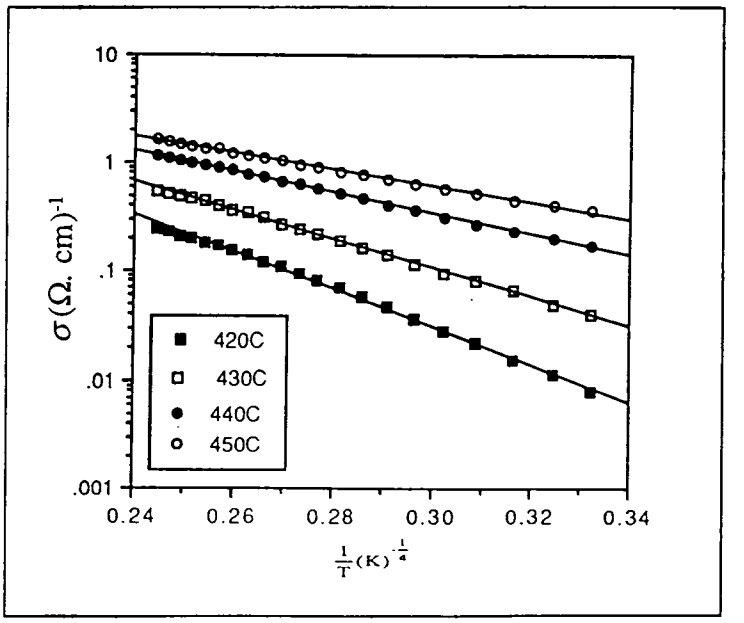

Figure (5.5) : Log σ versus $(1/T)^{1/4}$, for samples annealed at different temperatures (as labelled in the graph).

found suggested that, instead, a fit to the formula :

$$\sigma = \sigma_o \exp\left[-\left(\frac{T}{T_o}\right)\right]^{\gamma} \qquad (5.1)$$

With $\gamma<1$ was more appropriate.

In order to throw more light on the mechanism of conduction a series of curves were plotted using different values of γ from 0 to 1, so as to determine the best value. It was found that $\gamma = 1/4$ gave the best straight line fit to equation (5.1). This can be seen from figure (5.5), where the data in this figure were replotted as $\ell n\ \sigma$ versus $(1/T)^{1/4}$. This relationship will be discussed more fully later, but is typical of "hopping" behaviour.

5.3.2 - Hall measurements:

Samples used for this measurements were similar to those used for the conductivity measurements, (as described in section 5.3.1). A typical plot of Hall coefficient R_H, versus temperature for a typical reduced sample can be seen in figure (5.6), and shows that the variation in R_H was not large. Replotting the data as ℓog n versus temperature (i.e. assuming $R_H = \frac{1}{q\,n}$) in figure (5.7), shows that the carrier concentration increased a little with increasing temperature from $\sim$ 3 x 10^{17} cm^{-3} at 80K to $\sim$ 9 x

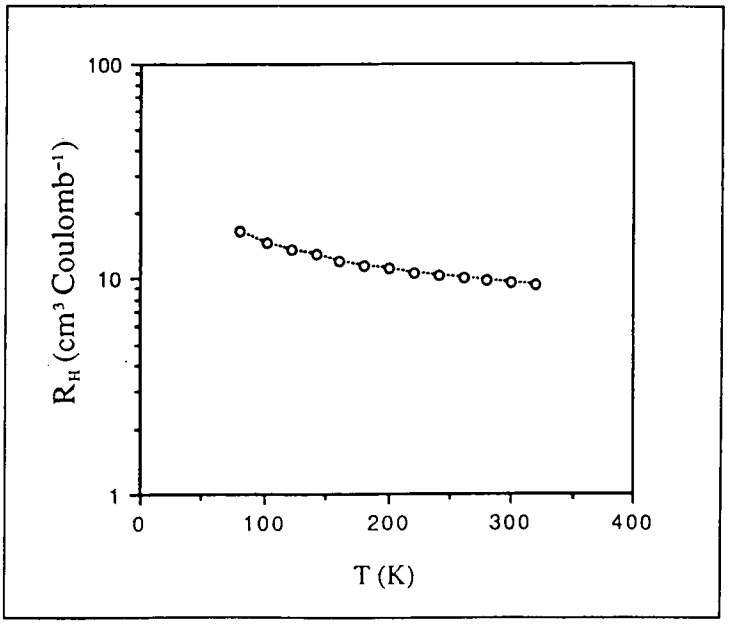

Figure (5.6) : Hall coefficient (R_H) versus temperature.

10^{17} cm^{-3} at 300K. When plotted on ℓn(n) versus 1/T axes, no evidence of the usual thermally activated carrier behaviour of the concentration of n was found (i.e. straight lines were not obtained).

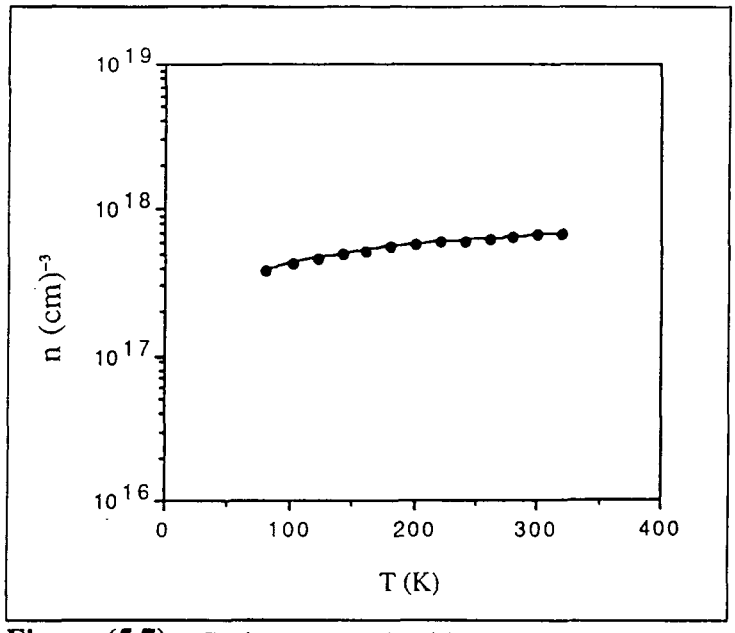

Figure (5.7) : Carrier concentration (n) versus temperature.

5.3.3 - Discussion:

As pointed out in section (5.3.1) the conductivity did not vary with temperature in a simple thermally activated way, but was more characteristic of "hopping" between localized states [5.1-5.3].

The movement of electrons in complex polycrystalline oxides is often associated with localized states in the energy gap [5.1], with electrons moving directly between localised states rather than via the conduction band. This localized state conduction can take place in three different ways, as has been described by Roberts, Apsley, and Munn (1980) [5.4]. First, they may be thermally activated over the potential barrier separating the two states. However, the barrier height is usually of the same order as the energy separating the localised states from the extended states, thus if the temperature is sufficiently high, extended state conduction will be the more favoured process. Secondly, carriers may tunnel through the potential barrier to

neighbouring states and thirdly carrier transport may take place by a combination of activation and tunnelling. This thermally assisted tunnelling has been dubbed "hopping" [5.4], and is an important feature of conduction in some oxide compounds. Hopping conduction should not be confused with the Pool effect [5.4], where conduction takes place by emission from the states to the conduction band. Here, conduction is directly from state - to - state.

Hopping or localized state conductivity is normally associated with amorphous material [5.5],[5.6-5.16], but XRD showed that our material was crystalline [chapter IV]. This implies that the energy required for localized state conduction, $\sigma(1/T^{1/4})$, was less than required for band conduction, $\sigma(1/T)$. Zn_2SnO_4 is a wide gap material, as may be deduced from its colour, which is white in the unreduced state. Although the reduced material was dark grey, this did not imply a change to a narrow gap phase, since the XRD results (chapter IV) clearly showed no such phase change was occurring. The colour change may be, instead, taken to indicate the creation of a high density of localized states in the gap by the reduction process (Oxygen vacancies, [5.17]). Such a high concentration of states is necessary for the electron to be able to transfer from state to state, since the states must be close to each other if the probability for hopping to occur is to be significant. In addition the Hall data showed that, although the carrier concentration was relatively high ($\sim 10^{17}$ cm^{-3}) there was little variation with temperature (80K - 300K), as one would expect for localized state conduction [5.4].

If the mean distance between nearest neighbour states is $\langle \Re nn \rangle$, then the probability at low field for hopping is given by exp $(-\langle \Re nn \rangle)$ [5.4], and the conductivity is therefore given by

$$\sigma = \sigma o \exp [-\langle \Re nn \rangle] \qquad (5.2)$$

The number of empty states $N(\Re)$ which lie within the range $\langle \Re nn \rangle$, is given by the integral

$$N(\Re) = \int\int_{\Re=constant} N(E)(1-f(E))4\pi\Re^2 dRdE \qquad (5.3)$$

where $f(E)$ is the Fermi Dirac function. If N(E) is constant and equal to N_f (the state density at the Fermi level), then it can be shown that [5.4]:

$$\langle \Re_{nn} \rangle \sim \left(\frac{24\,\alpha^3}{N_f \pi\, KT}\right)^{\frac{1}{4}} = \left(\frac{T_o}{T}\right)^{\frac{1}{4}} \qquad (5.4)$$

where $T_o = \left(\frac{24\alpha^3}{N_f \pi\, k}\right)$ is a characteristic temperature for hopping in the material , and

α may be regarded as the inverse Bohr radius of the localized states. Equation (5.4) is generally known as the Mott $T^{1/4}$ law of Variable Range Hopping (VRH)[5.3]. The conductivity is then given by :

$$\sigma = \sigma o \exp\ [\ -(To/T)^{1/4}\ ] \qquad (5.5)$$

where σo is a constant, hence the use of $(1/T)^{1/4}$ as the horizontal axis in figure ((5.5)

Analysis of the pre-exponential term, σo, shows that it is given by :

$$\sigma o = A\ q^2\ \alpha\ \nu\ \langle \Re nn \rangle^{-n}/kT \qquad (5.6)$$

Where A is a constant, ν is the frequency at which the electron attempts to leave the state, and n is an integer (either 2 or 3) [5.4].

Substituting for $\langle \Re nn \rangle$ by $-(To/T)^{1/4}$, the conductivity may be written :

$$\sigma = (A\ q^2\ \alpha\ \nu\ [To/T]^{-n/4}/kT)\ \exp\ [-To/T]^{1/4} \qquad (5.7)$$

Taking n = 3 [5.4] for bulk samples :

$$\sigma = (A\ q^2\ \alpha\ \nu\ To^{3/4}/k)/T^{1/4}\ \exp\ [-To/T]^{1/4} \qquad (5.8)$$

This suggests that a graph of $\ell n\ (\sigma T^{1/4})$ versus $(1/T)^{1/4}$ should give a straight line with slope = $(To)^{1/4}$, and intercept $\sigma o' = (A\ q^2\ \alpha\ \nu\ To^{3/4}/k)$.

Replotting the data of figure (5.5) on $\ell n\ (\sigma T^{1/4})$ versus $(1/T)^{1/4}$ axes gives a series of straight lines as shown in figure (5.8), confirming that hopping was the main transport mechanism.

The values of To and σo obtained from figure (5.8) have been listed in table (5.1). It may be noted that To depends inversely on the state density, N*f*, from equation (5.4). If it may be assumed that N*f* is generated by the reduction treatment, then one may speculate that N*f* is related to the reducing temperature by an equation of the form :

$N_f = N_{fo}\exp\left(\frac{-Ea}{kT_k}\right)$ substitution in To (equation 5.4) gives :

$T_o = \left(\frac{24\alpha^3}{N_{fo}\,\pi\,k}\right).\exp\left(\frac{Ea}{kT_k}\right)$ and a graph of ℓn (To) versus reciprocal annealing temperature should yield a straight line with positive slope, as can be seen in figure (5.9). From the slope of this straight line an activation energy of 395 kJ mole^{-1} is obtained. This rather high value may be compared with the activation energy of 82.4 kJ mole^{-1} obtained earlier for the reduction process from weight loss measurements (chapter IV), and suggests that N*f* is not directly related to the reduction process. The origin of the states associated with hopping mechanism is not known, however it may well be the case that more than one state is involved in the transport process.

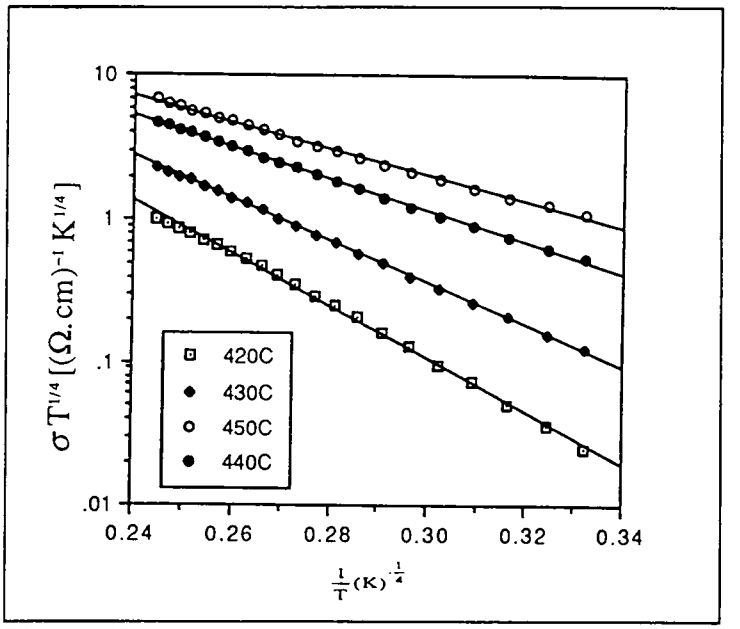

Figure (5.8) : ℓog $\sigma T^{1/4}$ versus $(1/T)^{1/4}$.

The carrier mobility in hopping conduction is dependant on the range ⟨ℜnn⟩ and thus on the applied voltage. Consequently, the standard relationship between σ,

n and μ :

$$\sigma = q \mu n \qquad (5.9)$$

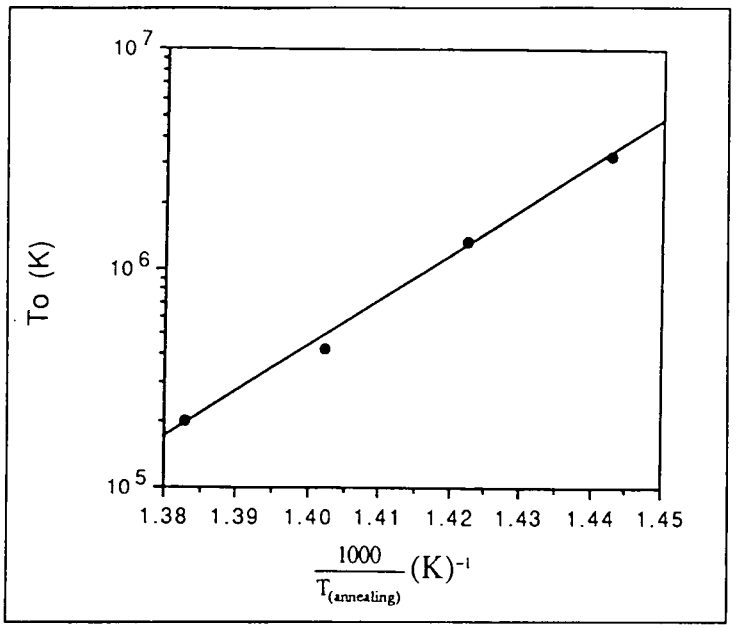

Figure (5.9) : T_o versus the reciprocal of the reducing temperature ($1/T_R$).

will not strictly apply. However, one may define an effective mobility, μ_{eff}, defined in the same way as :

$$\mu_{eff} = R_H \sigma \qquad (5.10)$$

which for a relatively constant R_H, will essentially follow the temperature dependence of σ, i.e. :

$$\mu_{eff} = \mu o \exp (To/T)^{1/4} \qquad (5.11)$$

Figure (5.10) shows a graph of ℓog (μ_{eff}) versus $(1/T)^{1/4}$ for a typical annealed sample (at 440°C for 12 hours, in 25%H_2 / 75%N_2 gas). The mobility values are low, $1 < \mu_{eff} < 14$ cm^2 v^{-1} sec^{-1} over the temperature range, 80K ≤ T ≤ 300K. In addition, the data display a good straight line relationship, i.e. ℓn (μ_{eff}) ∝ $(1/T)^{1/4}$. Both the low value and the $(1/T)^{1/4}$ dependence are consistent with hopping and provide additional evidence that localized states conduction was the dominant conduction mechanism [5.18],[5.3]. In fact, the effective mobility should become limited by percolation at

higher temperatures as the states become saturated. There is some evidence for the onset of saturation from figure (5.10) at the higher temperatures, where some small bending of the characteristic may be seen.

Hopping conduction has been reported in transition metal oxide ceramics [5.1]. In these materials electron transfer is thought to take place between ions of the same type, but which differ by unity in their oxidation state. Clearly, this is likely to occur readily in transition metal ceramics oxides such as NiO, where electron transfer from Ni^{2+} to Ni^{3+} ions on equivalent sites would constitute the conduction mechanism. In the present case the lattice contains Sn^{2+} and Sn^{4+} ions which in principle, could account for such a mechanism. However, in the case of tin the transition involves valency change of two ($Sn^{2+} \leftrightarrow Sn^{+4}$) and it is difficult to associate this with a hopping process in Zn_2SnO_4 in any simple way.

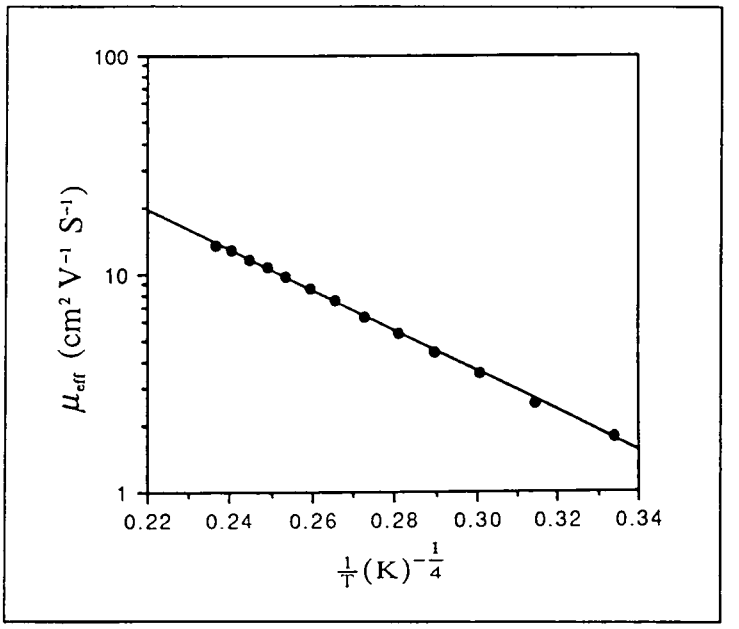

Figure (5.10) : Carrier mobility versus $(1/T)^{1/4}$.

5.4 - A.C. impedance measurements :

5.4.1 - Experimental results of a.c. impedance plots :

A.c. impedance plots were taken within the audio and radio frequency ranges (10 KHz $\leq f \leq$ 4 MHz) at room temperature. The real (R_s) and imaginary (X_s) parts of the impedance were calculated and plotted in the form of a complex impedance diagram (R_s verses X_s), as described in chapter II. It was found that reduced samples

were too conducting to make this kind of study and so the reduced samples were re - oxidised by heating in air at 600°C for 12 hours. As described earlier in chapter III, these plots enable the separation of the different contributions (e.g. grain boundary, and bulk resistance) to the resistance from the position of the low and high frequency intercepts etc [5.19-5.22].

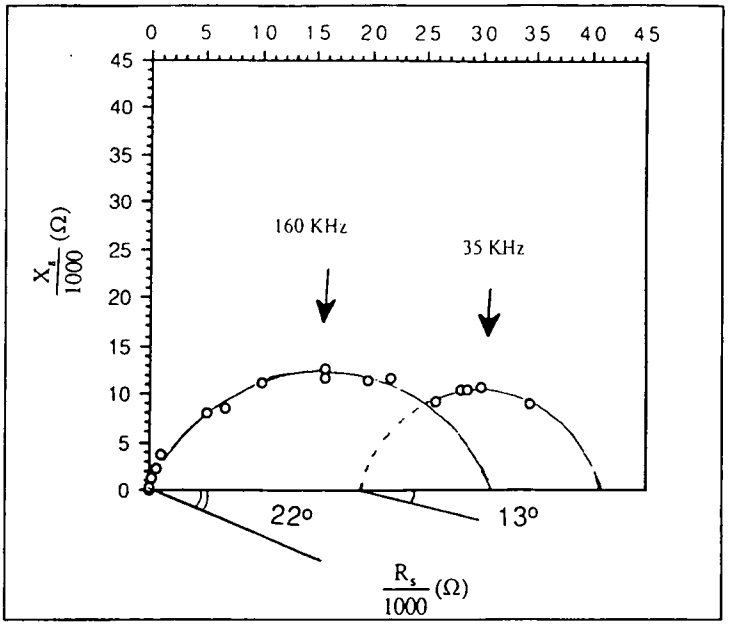

Figure (5.11) : A.c. impedance plot for a sample reoxidised in air (600°C for 12 hours), after reduction.

Figure (5.11) shows a typical complex impedance diagram for a re-oxidised sample. It was found that the high frequency intercept of the curve on the R_s axis for this sample was effectively zero, while the low frequency intercept was 4 x 10^5 Ω. The points displayed some scatter, but were best fitted by assuming two interpenetrating semi-circles as

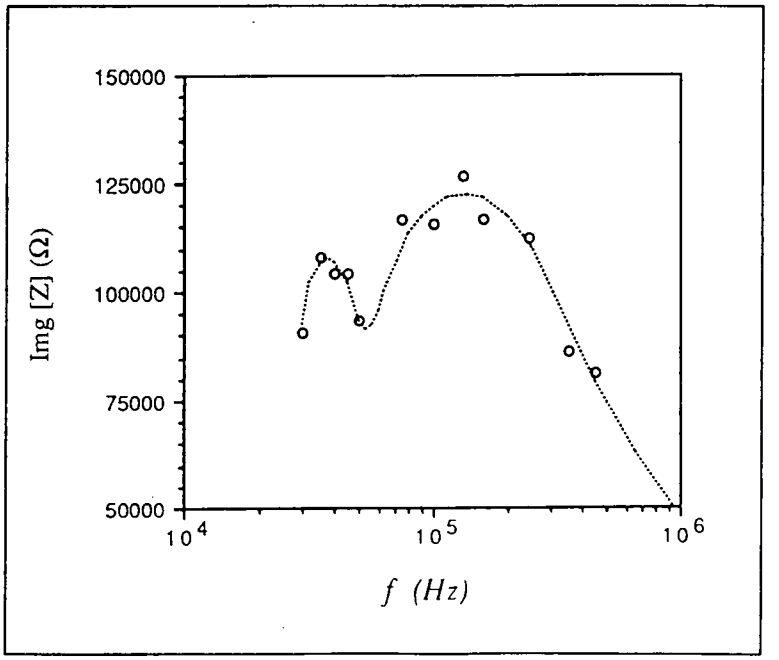

Figure (5.12) : The variation of the imaginary part of the impedance with frequency.

indicated in figure (5.11). The variation of the reactance, X_s, with frequency is given in figure (5.12), from which the maxima in the reactance are found to occur at 160 KHz and 35 KHz, with corresponding values of X_s of 1.28 x 10^5 Ω and 1.15 x 10^5 Ω respectively.

5.4.2 - Discussion :

The principle of impedance analysis is based on the fact that the physical processes which take place during charge transport through a solid or liquid system are conveniently represented by analogous electrical circuits with appropriate combinations of resistive and capacitive elements. Measurement of impedance over a wide range of frequency has been most successful in qualitative, as well as quantitative determination of these equivalent circuit parameters which provide a much better insight into the mechanisms of charge transport [5.19-5.24].

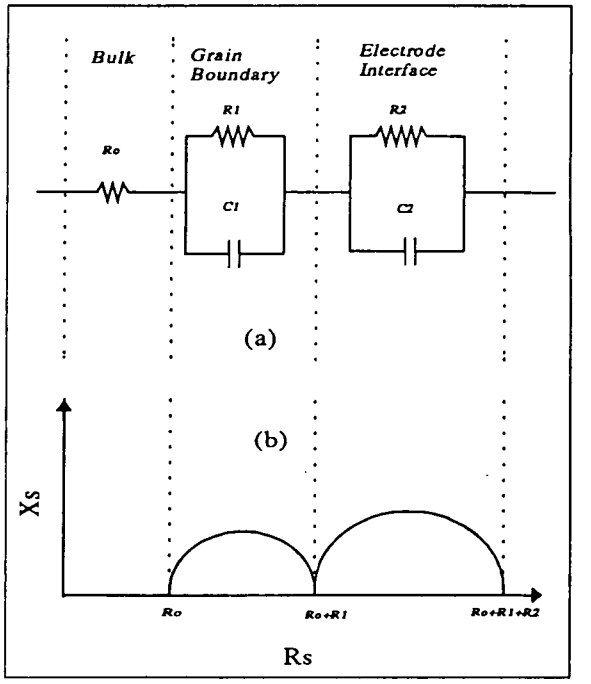

Figure (5.13) : Schematic equivalent circuit (a) and corresponding impedance plot (b) for electrical transport through a ploycrystalline solid.

The plot of the imaginary part (Xs) of the total impedance against the real part (Rs) as parametric function of frequency shows distinctive features characterizing specific combinations of the equivalent circuit elements. In general, each parallel R - C combination gives rise to a semicircular arc in the complex impedance plot, while a pure capacitance is represented by a vertical line. A series of semicircular arcs usually indicate a series combination of a number of lumped R - C circuit elements, each of which corresponds to a particular arc in the characteristic and

in turn to a distinct physical process having a significantly different relaxation time from the others [5.19-5.21,5.25]. Usually, three different processes take place during charge transport through a polycrystalline solid : (i) bulk conduction, or in other words intra-grain conduction, (ii) conduction across the grain boundary (inter-grain conduction) and (iii) transport across the electrode-specimen interface [5.23]. Each of these processes may be represented by independent R - C combinations and depending on the relative values of their relaxation times and on the magnitude of the three effects, they may give rise to up to three semicircles. In this context, our results, figure (5.11) may be interpreted as two semicircles.

From the diagram in figure (5.13), the following equation for the total series impedance can be deduced, from the individual equivalent R-C components :

$$Z = R_o + \sum_i Z(p)_i \qquad (5.12)$$

where $$\frac{1}{Z(p)_i} = \frac{1}{R_i} + j\omega C_i \Rightarrow Z(p)_i = \frac{R_i}{(1+j\omega C_i R_i)} \qquad (5.13)$$

Multiplying (5.13) by it's conjugate (1-j ω C_i R_i) :

$$Z(p)_i = \frac{R_i(1-j\omega C_i R_i)}{(1+\omega^2 C_i^2 R_i^2)} \qquad (5.14)$$

Substituting from (5.14) into (5.12) for a two component system :

$$Z_s = R_o + \frac{R_1}{(1+j\omega C_1 R_1)} + \frac{R_2}{1+(j\omega C_2 R_2)} = R_o + \frac{R_1(1-j\omega C_1 R_1)}{1+(\omega C_1 R_1)^2} + \frac{R_2(1-j\omega C_2 R_2)}{1+(\omega C_2 R_2)^2} \qquad (5.15)$$

By separating the complex parts, equation (5.15) becomes :

$$Z_s = R_s + jX_s \qquad (5.16)$$

$$Z_s = \left[R_o + \frac{R_1}{1+\omega^2\tau_1^2} + \frac{R_2}{1+\omega^2\tau_2^2}\right] - j\omega\left[\frac{R_1\tau_1}{1+\omega^2\tau_1^2} + \frac{R_2\tau_2}{1+\omega^2\tau_2^2}\right] \qquad (5.17)$$

where $\tau_1 = C_1 R_1$; $\tau_2 = C_2 R_2$.

From equation (5.17), the following may be deduced :

a) when $\omega = 0$, $X_s = 0$ & $Z_s = R_s = R_0 + R_1 + R_2$

b) $\omega \rightarrow \infty$ then $Z_s \rightarrow R_0$.

From these two results, it was found that $R_0 + R_1 + R_2$ for our sample was equal to $4.1 \times 10^5\ \Omega$, and from the high frequency region $R_0 \rightarrow$ zero, suggesting that there was no frequency independent component of conduction in the material. This may be interpreted as indicating that the grain bulk was depleted of free carriers (which would not display any frequency dependence). This would be consistent with the hopping mechanism suggested by the d.c. results (section 5.3). If the grain bulk is depleted. (i.e. no free carriers) then the only conduction process is the hopping mechanism between localized states. Such a hopping process has a natural time constant associated with it (i.e. it has an equivalent resistance - capacitance product related to the mean hopping time).

It can be seen that the relationship between X_s and R_s goes through two maxima, (from two semicircles) which means two relaxation times can be deduced through the following analysis :

From equation (5.17) the reactance is given by :

$$X_s = \omega \left[\frac{\tau_1 R_1}{(1+\omega^2\tau_1^2)} + \frac{\tau_2 R_2}{(1+\omega^2\tau_2^2)} \right] \qquad (5.18)$$

The semicircles will be well separated, if the maximum value of the two terms in the square brackets maybe distinguished. Thus one semicircle dominates when

$$\frac{\tau_1 R_1}{1+\omega^2\tau_1^2} \gg \frac{\tau_2 R_2}{1+\omega^2\tau_2^2} \qquad (5.19)$$

in which case we may ignore the second term of (5.18). Then the maximum, X_{s1}, will be at ω_{o1} which can be deduced from the following equations :

$$X_s \propto \frac{\tau_1 R_1 \omega}{1+\omega^2\tau_1^2} \Rightarrow \frac{dX_s}{d\omega} \propto \frac{\tau_1 R_1(1+\omega^2\tau_1^2)-2\tau_1^3 R_1\omega^2}{(1+\omega^2\tau_1^2)^2} \qquad (5.20)$$

for a maximum, $dX_s/d\omega = 0$, and this will occur when the numerator = 0, $\omega = \omega_o$,

$$\therefore \tau_1 R_1(1+\omega_{o1}^2\tau_1^2) = 2\omega_{o1}^2 R_1\tau_1^3 \qquad (5.21)$$

$$\text{from (5.21)} : \omega_{o1}^2 = \frac{1}{\tau_1^2} \Rightarrow \omega_{o1} = \frac{1}{\tau_1} \qquad (5.22)$$

Back substitution for ω to obtain the value of $X_s = X_{s1}$

$$X_{s1} = \omega_{o1}\left[\frac{\tau_1 R_1}{1+\omega_{o1}^2\tau_1^2}\right] = \frac{1}{\tau_1}\left[\frac{\tau_1 R_1}{(1+1)}\right] = \frac{R_1}{2}, \therefore R_1 = 2X_{s1} \qquad (5.23)$$

Hence $R_1 = 2X_{s1}$. From figure(5.11), $X_{s1} = 1.25 \times 10^5\ \Omega$, at $\omega_{o1} = 165$ KHz and $R_1 = 2.5 \times 10^5\ \Omega$.

Similarly at lower frequencies when the second term in equation (5.18) is dominant $\omega \propto 1/\tau_o$, and $R_2 = 2X_{s2}$, again from figure (5.11), $X_{s2} = 1.1 \times 10^5\ \Omega$ at 35 KHz and $R_2 = 2.2 \times 10^5\ \Omega$.

C_1, C_2 can be determine from ω_{o1}, ω_{o2}, from the definition, equation 5.17 :

$C_1 = \frac{1}{\omega_{o1} R_1}$, from graph (5.11) : $C_1 = 3.86 \times 10^{-12}$ Farad $= 2.9 \times 10^{-8}$ F m^{-2} , $C_2 =$ 20.7×10^{-12} Farad $= 1.55 \times 10^{-7}$ F m^{-2}. The results are summarised in table (5.2). It is tempting to speculate that one of the semicircles is related to grain boundary depletion, in which case the associated depletion width W should be simply related to the capacitance by : $W = 2\varepsilon_s/C$.

However the capacitance values were too small and the corresponding widths as a result were too large to relate to the grains (> 10 μm). It is therefore not possible at this stage to associate either of the equivalent capacitances with grain boundary

depletion and the corresponding relaxation times are clearly related to more complex phenomena.

Table (5.1) : Values of σo, and To for samples reduced at different temperatures.

All samples were heated for 14 hours in H_2/N_2 atmosphere.			
No.	Reducing temperature	σo $(\Omega\ cm)^{-1}$	To (K)
1	420°C	0.36×10^5	32.5×10^5
2	430°C	1.00×10^5	13.5×10^5
3	440°C	0.24×10^4	4.2×10^5
4	450°C	0.12×10^4	2.0×10^5

Table (5.2) : Equivalent circuit parametrs from a.c. impedance measurements, for an undoped sample.

Parameter	Value	Parameter	Value
R_o	≈ Zero	ω_{o1}	1.01×10^6 Hz
R_1	$2.5 \times 10^5\ \Omega$	ω_{o2}	2.2×10^5 Hz
R_2	$2.2 \times 10^5\ \Omega$	C_1	29 nF m^{-2}
f_1	160 KHz	C_2	155 nF m^{-2}
f_2	35 KHz	ε_s	7.27×10^{-11} F m^{-1}

5.5 - Summary :

As-fired Zn_2SnO_4 is very resistive and it was not possible to make any electrical measurements, unless the sintered Zn_2SnO_4 pellets were refired in a reducing atmosphere (H_2/N_2 mixture at 450°C for 14 hours). The conductivity as a result of this treatment was changed from 10^{-9} Ω^{-1} cm^{-1} to 10^{-2} Ω^{-1} cm^{-1}. Dc conductivity, R-T, Hall, and dielectric (a.c. impedance) measurements were carried out on reduced samples (partially reduced samples for ac impedance measurements only). Ohmic contacts were obtained using In/Ga alloy and were tested for ohmic behaviour using pulsed current - voltage measurements.

Dc conductivity measurements revealed that the main carrier transportation mechanism was variable range hopping, where the temperature dependence of the conductivity varied as $\exp(To/T)^{1/4}$. This result was consistent with similar phenomena in other ceramics systems. Hall measurements showed that the carrier concentration was constant with temperature at about 10^{17} cm^{-3}. This would be expected for a ceramic where electron hopping was the main conduction process.

The mobility result was found to obey the same temperature dependence, $\exp(To/T)^{1/4}$, again as expected for a hopping mechanism phenomena.

A.c. impedance measurements gave two semicircles on the complex impedance plot indicating that there were two quite separate relaxation times ($\tau_1 = 6.25 \times 10^{-6}$ sec, $\tau_2 = 2.86 \times 10^{-5}$ sec) associated with the conduction. It was not possible to relate either to any particular mechanism (i.e grain boundary effects, hopping, etc.).

All of the experimental results and analysis showed a good degree of reproducibility and consistency between the different analytical methods.

5.6 - References

[5.1] - Moulson A. J. and Herbert J. M., "Electroceramics",(Chapman and Hall, London, (1990).

[5.2] - Seymour P., and Keller "Handbook on Semiconductors", **3** (1982).

[5.3] - Mott N. F. and Davis E.A.,"Electronic Processes in Non-crystalling Materials", p345, p36, (1979).

[5.4] - Roberts G. G., Apsley N., and Munn R. W., Phys. Rep., **60**, 59, p108, (1980).

[5.5] - Sheng P., Abeles B., and Arie Y., Phys. Rev. lett. **31**, 44(1973).

[5.6] - Shklovskii B. I., Efros A. L.,"Electronics Properties of Doped Semiconductors", Springer Verlag, Berlin, (1984).

[5.7] - Kostandinov I. Z. and Alexanderov B., Physica C, **201**, 126, (1992).

[5.8] - Kim J.J., Kim J. H. and Lee H. J.,Phys Rev B, **46**, 11709, (1992).

[5.9] - Greaves G.N.,J Non-crystalline Solids (1973).

[5.10] - Elliott S. R., Davis E. A., and Pitt G. D., Solid State Commun., **22**, 48, (1977).

[5.11] - Hauser J.J., Phys. Rev. B, **29**, 738 (1975).

[5.12] - Katsumoto S., Komori F., Sano N., and Kobayashi S., J. Phys. Soc. Japan, **58**, 2634 (1989).

[5.13] - Allgaier R. S., Bulletin of the American. Physical Society, Series II, **18**, 361 (1973).

[5.14] - Bottger H., and Bryksin V. V., (Review Article), Phys Stat Sol(b), **78**, 9 (1976).

[5.15] - Brenig W., Dohler G. H., and Heyzenav H., Phil. Mag., **27**, 1093 (1973).

[5.16] - Bloch A. N., Shante V. K., and Varma C. M., Phys Rev. Lett, **28**, 753, (1972).

[5.17] - Abeles B., Sheng P., Coutts M. D. and Aries Y., Adv. Phys., **24**, 407 (1975).

[5.18] - Orton J. W., and Powell M. J.,Rep. Prog. Phys., **43**, (1980).

[5.19] - Badwal S.P.S.,in Proc. Inter. Seminar. "Solid State Ionics Devices", ed. B. V. R. Chowdari and S. Radhakrisha (World Scientific. Singapore. 1988) p 165.{ as quoted in ref. 34}.

[5.20] - Reddy S. N., Chary A. S., Shahi K. and Chiranjivi T., J. Mater. Sci. : Mater. in Electronics **1**, 153-158, (1990).

[5.21] - Rao K. V., and Smakula A., J. Appl. Phys. **36**, 2031, (1965).

[5.22] - Kawashima R., and Hirai K., Phil. Mag., **58**, 663, (1988).

[5.23] - Basu R. N., and Maiti H. S., Trans. Indian Ceramic Soc., **45**, 140, (1986).

[5.24] - Anderson V. "Dielectrics", Spottiswoode and Ballantyne, London, (1964).

[5.25] - Jonscher A. K., J. Mater. Sci., **24**, 372, (1989).

CHAPTER VI

DOPED ZINC STANNATE (Zn_2SnO_4) :

6.1 - Introduction :

The use of dopants as a means of controlling the properties of a given material is well established both in semiconductors and ceramics. Small quantities of appropriate impurity are typically used to control the resistivity, mechanical or electrical behaviour of such materials. However, in a material [6.1-6.5], like zinc stannate which is relatively unresearched, such doping studies have not yet been carried out. There have been a few reports of research in Zn_2SnO_4, and these mostly concern room temperature microstructure [6.2-6.6]. No electrical characteristics, still less any theoretical studies have been undertaken on zinc stannate. A complete picture of the effects of dopant type or concentration, therefore, has not yet been established. The study described in this chapter has examined aspects of colour change, microstructure and electrical conductivity following donor dopant incorporation into polycrystalline zinc stannate, and in particular, has studied the effects of donor concentration on grain boundary characteristics, resistivity and complex impedance.

A number of doping trials were carried out with Zn_2SnO_4 in order to find ways of controlling the resistivity extrinsically. The intention was to try and dope substitutionally, with elements from groups III and V of the periodic table which, depending on whether they substituted for Zn or Sn in the host lattice, would act as donors or acceptors [6.1]. For example, if a Zn atom were replaced by an In atom, then the third valence electron on the In ion is only loosely bound to it, as a result only a small amount of energy (i. e. << KT at room temperature) would be required to break the bond and release the electron, which is then said to have been donated to the conduction band of the Zn_2SnO_4. Similar arguments may be applied for the other cases, e.g. a group V ion substituting for Sn^{4+} in the lattice etc.. Attempts were made to dope the Zn_2SnO_4 using Nb, Ta, V, In and Bi. The dopants were introduced in a variety of ways, from different precursors and at different stages in the processing.

Metal-semiconductor (M-S) diodes were also investigated. These allow voltage - dependant capacitance relationships to be investigated. Such measurements give estimates of net carrier donor density and provide an indication of interface state activity.

6.2 - Sample preparation :

Samples were prepared in a number of ways :

a)- by milling crushed pellets of zinc stannate, with powders of the relevant dopant in concentrations ranging from 0.01% - 10% M (M = Nb_2O_5 ,$InCl_3.3H_2O$, $TaCl_5$, In_2O_3) for 12 hours in a polyethylene mill using deionized water and agate media. After drying the mixture, pellets were pressed in the usual manner. Generally 5 samples of each composition were sintered in the muffle furnace, at 1280°C for 12 hours.

b)- by crushing pellets of zinc stannate with the dopant in a pestle and mortar, before pressing and sintering pallets as in (a).

c)- by pre-doping the SnO_2 or ZnO precursor powders and then pressing and firing to form sintered pellets (section (6.3))[6.7].

d)- doping with pure indium metal from the vapour phase.

With exception of, the indium doping (d), the as-fired samples were found to be too insulating for electrical measurements, thus the samples were usually reduced as described in chapter IV. Samples were polished slightly, to flatten their surfaces and electrodes of In/Ga alloy were applied. The resistivity of five nominally identical samples were measured as a function of temperature in a cryostat, between temperatures 77K and 300K as described in chapter III. An average resistivity was then calculated, together with the variation between samples, to check reproducibility between nominally identical samples. Thin samples ($\sim$ 1 mm thick) were prepared for the dielectric measurements (capacitance and impedance plots) in order to minimise

any effects of fringing on the electric field across the samples. In/Ga alloy was again used for the electrodes. The measured samples were also used for current - voltage measurements, enabling larger fields to be applied using a standard laboratory power supply. These measurements were carried out at room temperature.

6.3 - Direct Doping Methods :

6.3.1 - Nb_2O_5

Initially different amounts of Nb_2O_5 were added to the SnO_2+ZnO starting materials so as to give a range of Nb:Sn ratios (the amount of SnO_2 was reduced in proportion to ensure a constant (Sn+Nb):Zn ratio). Subsequently Nb_2O_5 was also added directly to Zn_2SnO_4, as this was found to be more reproducible. The powders were then mixed and pressed (2 Ton pressure) into 13 mm diameter pellets before firing at 1280°C (with a heating rate of 5°C min^{-1}) for 12 hours. Cooling was at the natural rate of the furnace.

6.3.2 - $TaCl_5$

In this case the $TaCl_5$ powder was added directly to Zn_2SnO_4 powder rather than to the precursor materials. The powders were mixed in acetone in order to improve homogeneity, and the resulting slurry was then dried for 6 hours in the usual way, and fired at 1280°C (with a heating rate of 5°C min^{-1}) for 12 hours.

6.3.3 - Ta_2O_5

This was a second attempt at doping with Ta, using the oxide rather than the chloride as the dopant precursor. The samples were prepared in an identical manner to that used for Ta_2Cl_5 doping, with the Ta_2O_5 added directly to the Zn_2SnO_4 powder.

6.3.4 - $InCl_3.3H_2O$

$InCl_3.3H_2O$ was added to the Zn_2SnO_4, and the powders mixed, dried and pressed and then fired. Due to the higher volatility of In, a two step heating regime was used in which there was an initial In in-diffusion stage at a temperature of 500°C before the temperature was raised to 1280°C in order to sinter the pellets. The firing profile is shown in figure (6.1).

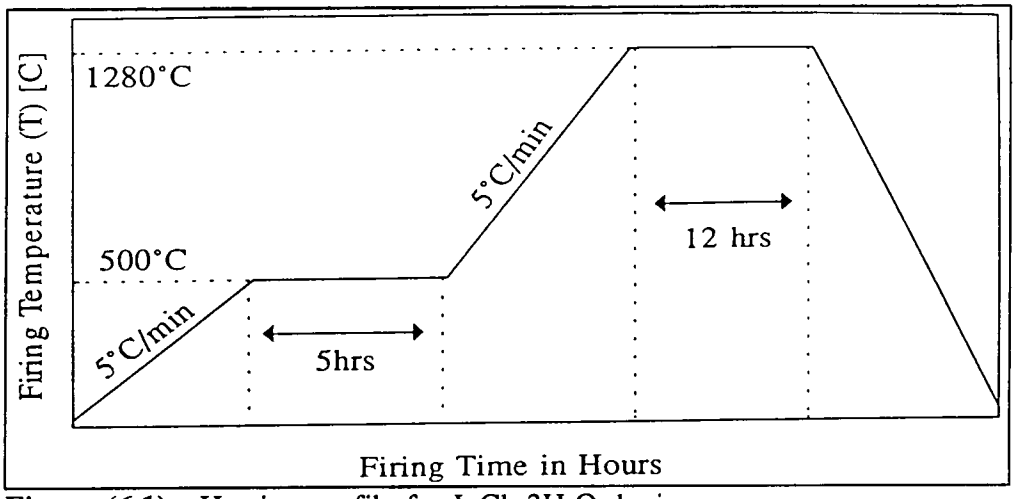

Figure (6.1) : Heating profile for $InCl_3.3H_2O$ doping.

6.4 - Pre-doping of Zn_2SnO_4 precursors :

6.4.1 - Pre-doping of SnO_2 with Nb_2O_5

An attempt was also made to pre-dope the SnO_2 starting material with Nb_2O_5. The SnO_2 was mixed in varying proportions with the Nb_2O_5, and then pressed into pellets and fired.

6.4.2 - Pre-doping ZnO with Nb_2O_5, In_2O_5 and Bi_2O_5

Similar pre-doping trials were carried out with the ZnO precursor. As with the SnO_2, the dopant was added to the ZnO powder which was then mixed, pressed and fired. The pre-doped ZnO was then used in three different mixtures:

a) - Nb-doped ZnO + Nb-doped SnO_2;

b) - Nb-doped ZnO + undoped SnO_2 + Nb_2O_5;

c) - Nb-doped ZnO + undoped SnO_2.

All three powder mixtures were pressed and fired for 12 hours at 1280°C in air, as usual.

6.5 - Indium doping (Vapour Phase Method) :

This method was an attempt to dope directly from the element. The indium dopant source and the Zn_2SnO_4 samples were placed in a sealed two chamber, evacuated (5 x 10^{-6} mbar) silica ampoule, which was then loaded into a two zone furnace such that the In and sample were at temperatures of 350°C, and 850°C respectively for 48 hours. The ampoule was removed from the furnace indium side first to allow the indium vapour to condense away from the sample.

6.6 - Characteristics of Ta and V Doped Zn_2SnO_4 :

The as-fired pellets, which were doped with $TaCl_5$, did not sinter well and crumbled easily, and were highly resistive. The samples which were doped with Ta_2O_5, were white in colour and resistive , but less crumbling than those doped with $TaCl_5$. Figure (6.2) shows the variation of resistivity with doping (Ta_2O_5) levels for *reduced* samples. Since the differences between the resistivity values were not

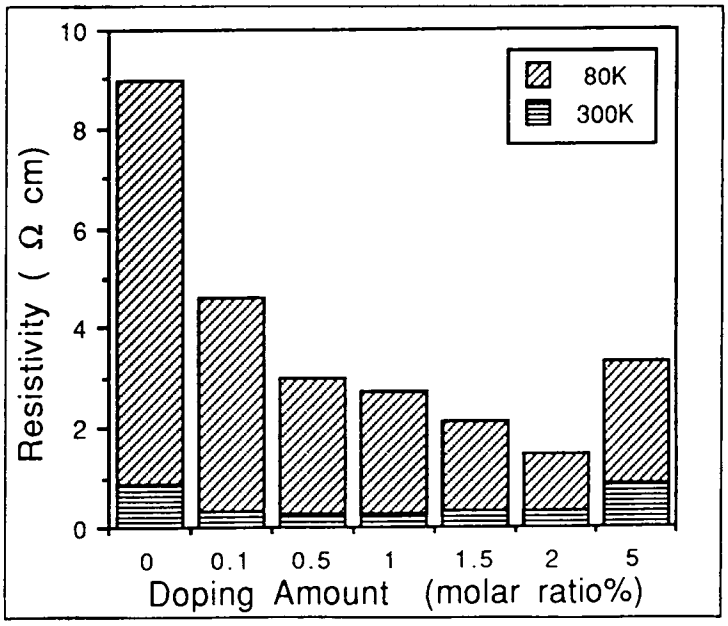

Figure (6.2) : Resistivity versus the doping level for Ta_2O_5-doped reduced samples.

large, with all the maximum values lying between 10 Ω cm and 1 Ω cm, then it may be assumed that the resistivity was not related to the doping, but to small differences in the reduction atmosphere process.

It was found that samples doped with V_2O_5 were very hard to break after sintering, and there was a colour change from pale to deep brown as the doping level was increased. However, all the as-fired samples were resistive, although they became conductive after the usual reduction treatment in H_2/N_2 atmosphere. This can be seen from figure (6.3). Examination in the SEM revealed the existence of a liquid second phase, which was increased by increasing the doping level of V_2O_5. The increase in the resistivity at high doping levels, specially at 1.5% level, was thought to be caused by the effects of this liquid phase, which might have caused effective separation of zinc stannate grains.

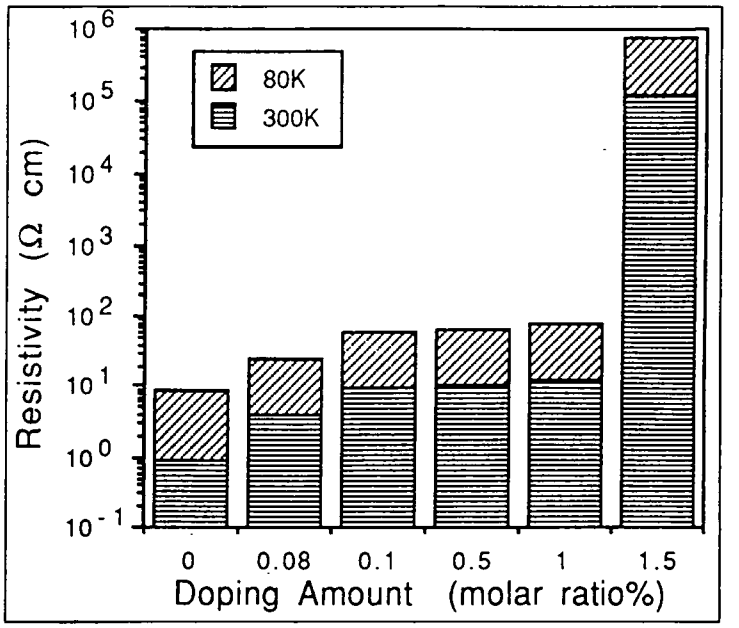

Figure (6.3) : Resistivity versus the doping level for V_2O_5-doped reduced samples.

6.7 - Characteristics of Nb_2O_5 Doped Zn_2SnO_4 :

6.7.1 - Structure :

As fired surfaces were examined in the Scanning Electron Microscope (SEM) to investigate their microstructure and any surface features (segregated second phase and impurities) were analyzed using the Energy Dispersive X-ray (EDAX) attachment

and x-ray diffraction. Average grain size was calculated using an area count method of at least 200 grains and assuming them to be cubic.

The as-fired surfaces of all Nb_2O_5 doped samples showed evidence of densification and grain growth during sintering. Samples containing the lowest amounts of dopant (< 0.1 at % Nb_2O_5) were white in colour and appeared shiny, suggesting the presence of a glassy (reflective) surface phase. Those containing between 0.2 and 5 at % Nb_2O_5 had surfaces covered with dark grey spots. The doped pellets were very hard, become harder when either the sintering temperature or the sintering time were increased. The pellets which were sintered at the highest temperature, 1350°C suffered shrinkage and displayed a concave surface.

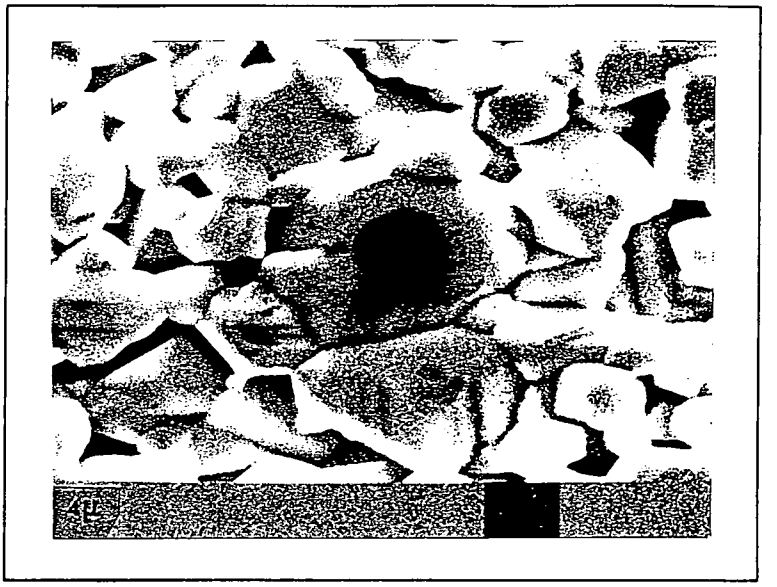

Figure (6.4) : Scanning electron micrograph of the surface of a Nb_2O_5-doped sample (0.1% Nb_2O_5).

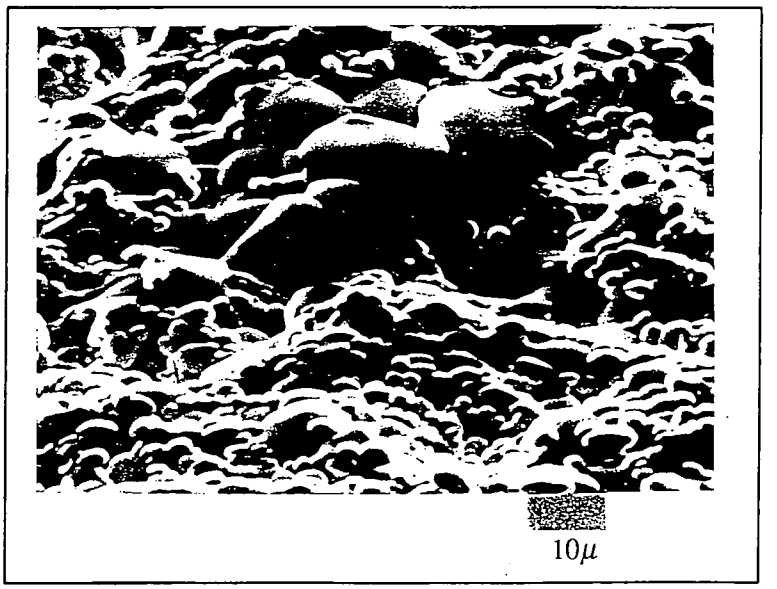

Figure (6.5) : Scanning electron micrograph of the surface of a more heavily doped Nb_2O_5-doped sample (5% Nb_2O_5).

The average grain size of samples

was found to decrease by approximately an order of magnitude from 12 to 3 μm, as the donor concentration was increased from 0.01 - 5 at % Nb_2O_5. Figure (6.4) shows a scanning electron micrograph of a sample containing 0.1% Nb_2O_5, where the grains were about 10 μm average size. Comparison between figure (6.4) and figure (6.5) shows that the grains become much more rounded in shape with a less homogeneous size distribution at higher doping levels. Additional features in the form of large irregular rounded shapes, as shown in figure (6.5), also appeared.

EDAX analysis revealed that the Zn and Sn relative intensities were the same as for undoped sintered pellets, although a niobium peak, appeared at high dopant levels ≥ 2 Nb_2O_5 at %, as can be seen from figure (6.6). X-ray diffraction spectra also showed three additional peaks, two of which were close to the position of the main peaks of niobium stannate ($Sn_2Nb_2O_7$). The third peak could not be identified (see table (6.1). This additional new phase suggested that there was a reaction between SnO_2, Nb_2O_5 forming an un-expected new phase.

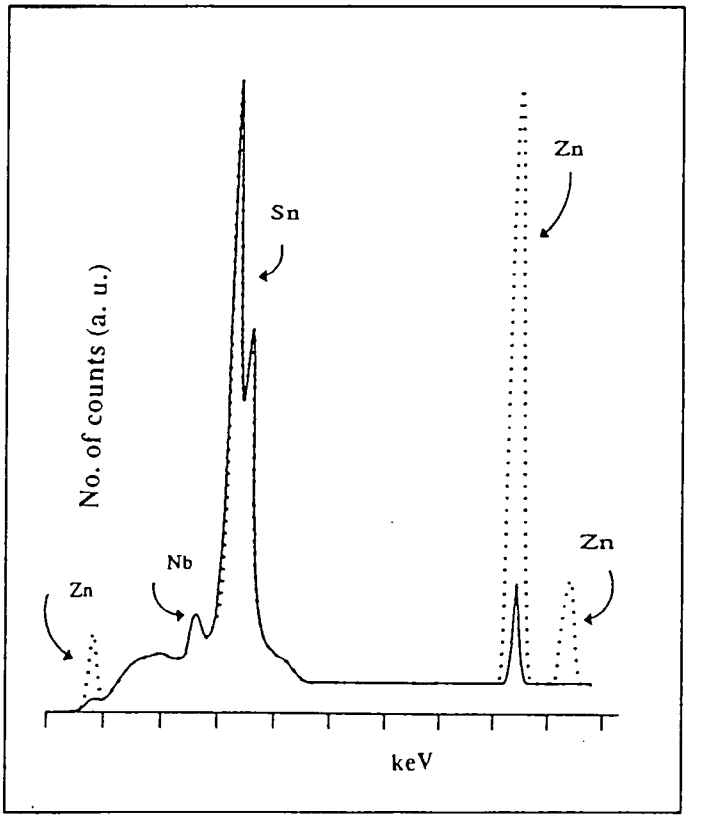

Figure (6.6) : EDAX spectrum for a Nb_2O_5-doped sample (2% Nb_2O_5). Dotted line; normal sintering : solid line; sintering temperature > 1350°C.

Table (6.1) : X-Ray Diffraction Data for additional peaks observed in Nb-doped Zn_2SnO_4 (> 5% Nb_2O_5).

No	2θ	d Å	h k l	Assignment
1	31.1	3.34	------	Unknown
2	34.1	3.05	2 2 0	Zn_2SnO_4 & $Sn_2Nb_2O_7$
3	39.5	2.64	------	$Sn_2Nb_2O_7$
Radiation CoKα with λ = 1.7902 Å, Fe filter				

6.7.2 - D.C. Transport measurements :

6.7.2a - Conductivity - Temperature characteristics :

The as-fired pellets were all highly resistive and only the most heavily doped ~ 5% Nb_2O_5 showed some change of colour (from white to grey). Consequently, electrical characteristics could only be measured on reduced samples. Figure (6.7) shows the variation of resistivity with doping level (for reduced samples) at temperatures of 80K and 300K. This clearly shows that when the doping level was increased above ~ 0.5% there was a corresponding increase in the

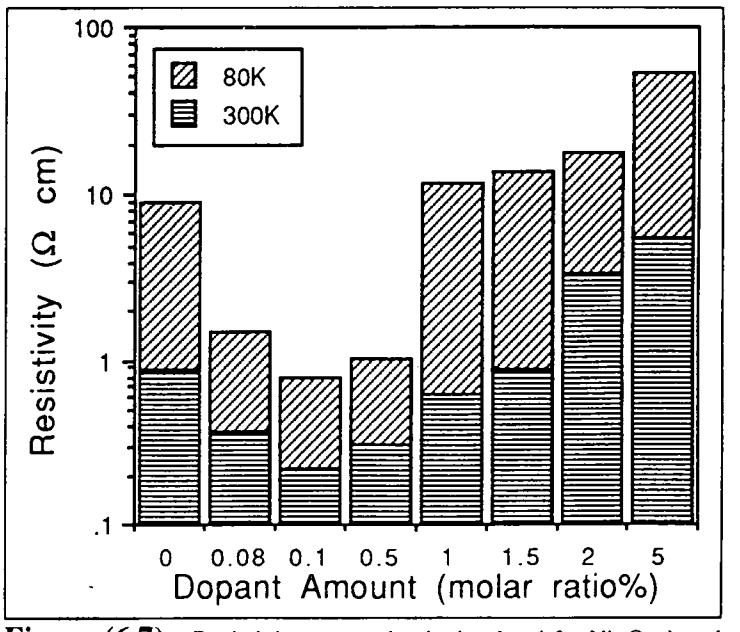

Figure (6.7) : Resistivity versus the doping level for Nb_2O_5-doped reduced samples.

resistivity. Whether this indicates that at very high levels of doping there was a marked increase in segregation to the grain boundaries, is not known, but it may also be related to the changes in grain shape observed in the SEM. In addition the Hall data showed that the carrier concentration was relatively high (about 10^{18} cm^{-3}), but with little variation with temperature (77K to 300K), this can be seen from figure (6.8). The carrier mobility revealed a linear variation when plotted on $\ell og(\mu)$ versus $(1/T)^{1/4}$, as can be seen from figure (6.9).

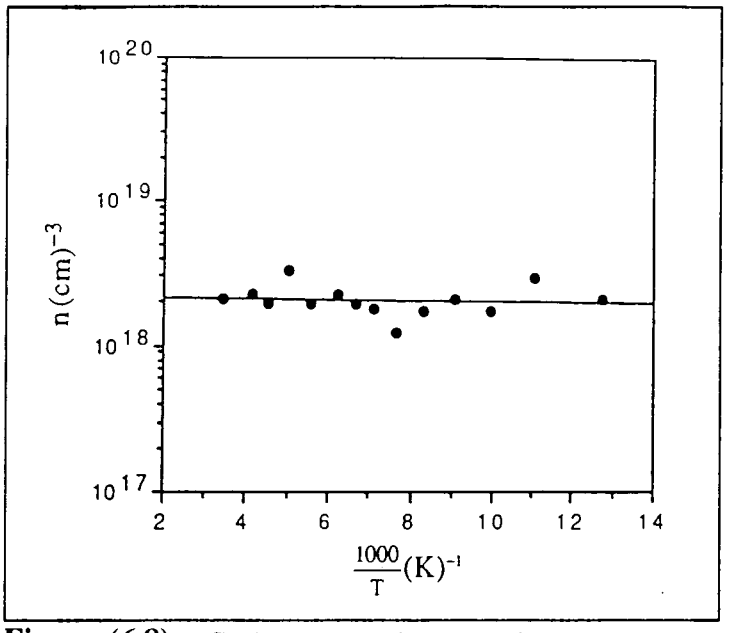

Figure (6.8) : Carrier concentration versus inverse temperature (0.5% Nb_2O_5).

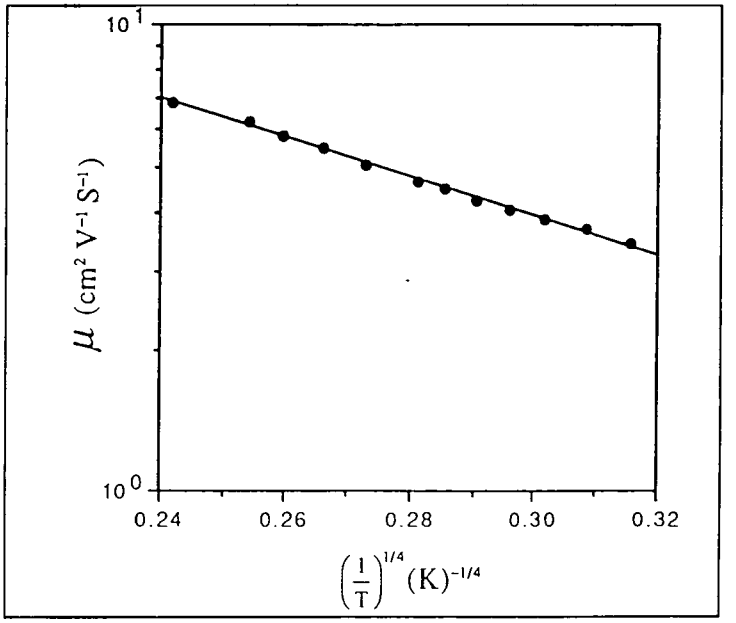

Figure (6.9) : Carrier mobility versus $(1/T)^{1/4}$ for (0.5% Nb_2O_5)-doped reduced samples.

A typical series of plots of conductivity versus temperature, between 77K and 300K, are shown in figure (6.10), for doped samples annealed under the same conditions, but with different levels of doping, from 0.01% Nb_2O_5 to 5%

Nb_2O_5.

It can be seen from figure (6.10) that the conductivity increased with increasing measurement temperature, which is typical of semiconductor behaviour. However, the data were found to lie on a concave curve (rather than a straight line) on a $\ln \sigma_{DC}$ versus 1/T plot, showing that the conductivity was not of the simple activated form

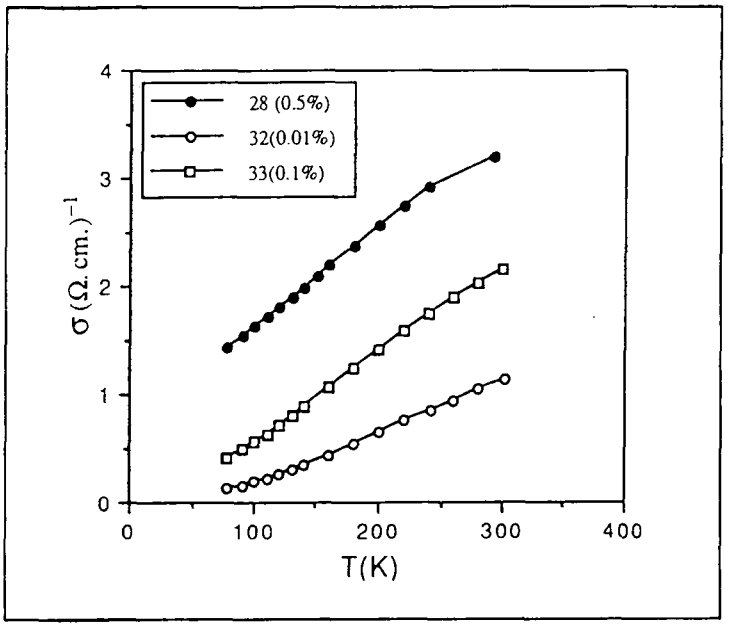

Figure (6.10) : Conductivity-Temperature characteristics for Nb_2O_5-doped reduced samples.

$$\sigma \propto \exp\left(\frac{-Ea}{kT}\right) \quad ...(6.1)$$

where E_a is the activation energy , and k is Boltzman constant (see figure (6.11)). The curvature found suggested that, instead, a fit to the formula:

$$\sigma = \sigma o \exp\left[-\left(\frac{T_o}{T}\right)\right]^{\gamma} \quad .(6.2)$$

With $\gamma < 1$ was more

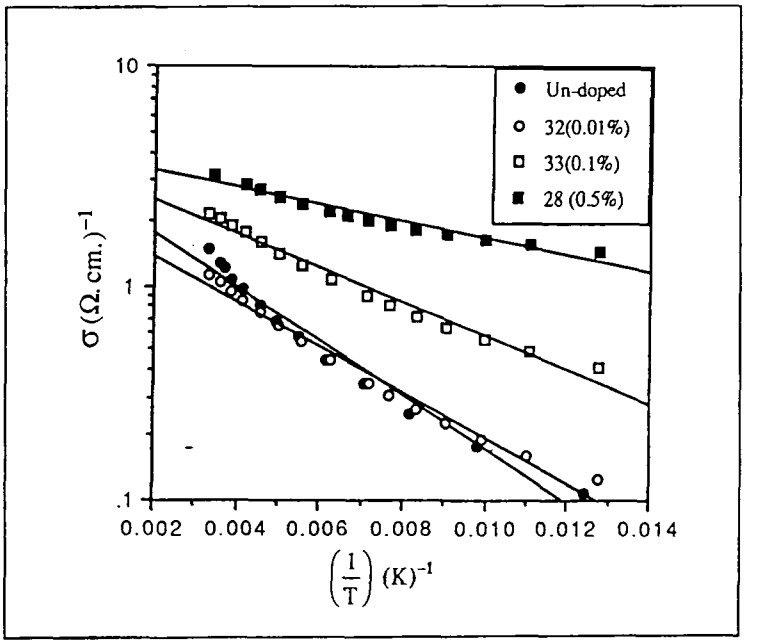

Figure (6.11) : Conductivity versus inverse temperature for Nb_2O_5-doped reduced samples of different doping levels.

appropriate. As in chapter V a series of curves were plotted using different values of γ from 0 to 1, so as to determine the best fit to the data. This showed γ = 1/4 gave the best straight line fit, suggesting Variable Range Hopping was the principal conduction mechanism (chapter V, equation (5.5)), as can be seen from figure (6.12), where the data are replotted as $\ell n\ \sigma T^{1/4}$ versus $1/T^{1/4}$. This relationship is typical of "hopping" behaviour [6.8]. Values of σo

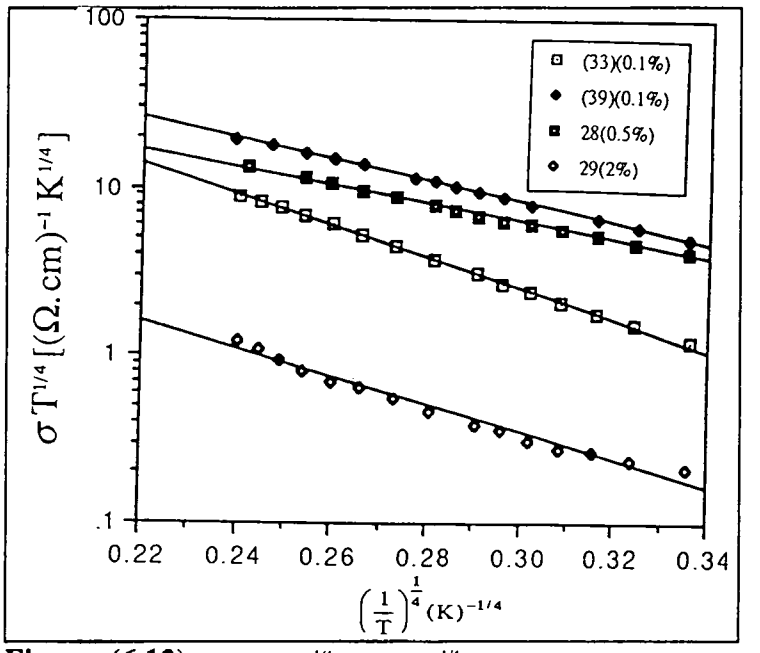

Figure (6.12) : ℓog ($\sigma T^{1/4}$) vs $(1/T)^{1/4}$ characteristics for Nb_2O_5-doped reduced samples of different doping levels.

Table (6.2) : Values of σo, and To for a few Nb_2O_5-doped samples.

All samples were heated for 14 hours in H_2/N_2 atmosphere.				
No.	Doping amount (Nb_2O_5)	σo	To	No
1	0	1.27×10^4	9.8×10^5	16
2	0.01	3.64×10^3	5.4×10^5	32
3	0.1	1.64×10^3	2.1×10^5	33
4	0.5	0.10×10^3	1.3×10^5	29
5	2	0.3×10^3	2.4×10^4	28

and To obtained for different Nb doped samples are listed in table (6.2). Both σo and To show a systematic reduction with increasing doping concentration from $\sigma o = 1.27 \times 10^4\ \Omega$, To = 9.8×10^5 K for un-doped material to $\sigma o = 0.3 \times 10^3\ \Omega$, To 2.4×10^4

for 2% Nb_2O_5 doping. The reasons for this apparent dependence are not clear, but may be related to changes in the reduction /oxidation process induced by the segregation of Nb to the grain boundaries. Hall carrier concentrations showed little variation with temperature, and a straight line dependence of log carrier mobility with $(1/T)^{1/4}$ (explained in detail in chapter V), also gave additional support for the hopping phenomena to be the dominant mechanism in this system. The hopping mechanism has been described fully already in chapter V.

6.7.2b - Discussion :

The effectiveness of Nb doping is difficult to assess, since it was still necessary to reduce the samples in order to make them conducting. Moreover, the fact that the transport mechanism in reduced, Nb-doped samples was the same as in undoped, reduced samples suggests that the Nb doping was not effective. However, the Nb doped, reduced samples were about an order of magnitude more conducting (for 0.5% doping) than the corresponding undoped samples, suggesting that the Nb had played some role in increasing conductivity. It seems unlikely that Nb has doped in the conventional substitutional way, since that would have resulted in a change in conductivity in the as-fired condition. It is possible that the Nb has doped amphoterically, resulting in highly compensated material, which would provide an explanation for the observed colour change. It is also possible that the Nb increased the efficiency of the reduction process in some way , and hence the factor of ten increase in the doped, reduced-state conductivity.

Finally, Nb_2O_5 has a high melting point (1485∓5°C) and would thus be difficult to incorporate into the Zn_2SnO_4 lattice at the normal usual temperature (1280°C). Some trials at higher temperatures were attempted, which produced a more homogenous colour change, but also resulted in the onset of decomposition of the Zn_2SnO_4 (see chapter IV).

6.7.3 - A.C. impedance measurements :

6.7.3a - Experimental results of a.c. impedance plots :

A.c. impedance plots were taken within the audio and radio frequency ranges (10 KHZ ≤ υ ≤ 4 MHZ) at room temperature. The real (R_s) and imaginary (X_s) parts of the impedance were calculated and plotted in the form of a complex impedance diagram (R_s verses X_s), as described in chapter III. As for the undoped samples, it was found that reduced samples were too conducting to make this kind of study and so the reduced samples were re - oxidised by heating in air at 600°C for 12 hours. A.c. impedance plots enable the separation of the different contributions (e.g. grain boundary [6.9], and bulk resistance) to the resistance from the position of the low and high frequency intercepts etc., as described earlier in chapter V.

Figure (6.13A) shows a typical complex impedance diagram for a re-oxidised

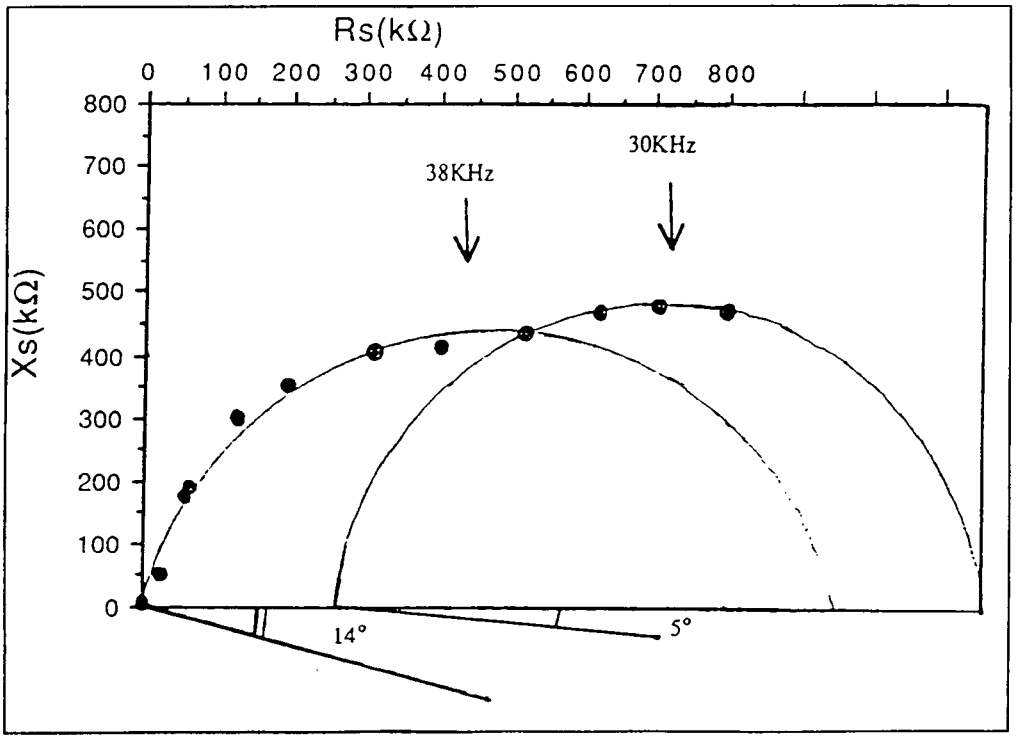

Figure (6.13A) : Room temperature a.c. impedance plot for 5% Nb_2O_5-doped sample.

doped sample (5% Nb_2O_5). It was found that the high frequency intercept of the curve

on the R_s axis for this sample was effectively zero, as observed for the undoped material in chapter V, while the low frequency intercept was ~ 11.3 x 10^6 Ω. The points displayed some scatter, but were best fitted by assuming two interpenetrating semi-circles as indicated in figure (6.13A). The variation of the reactance, X_s, with frequency showed that the maxima in the reactance occured at 38 KHz and 30 Khz, with corresponding values of X_s of 3.95 x 10^6 Ω and 4.8 x 10^5 Ω.

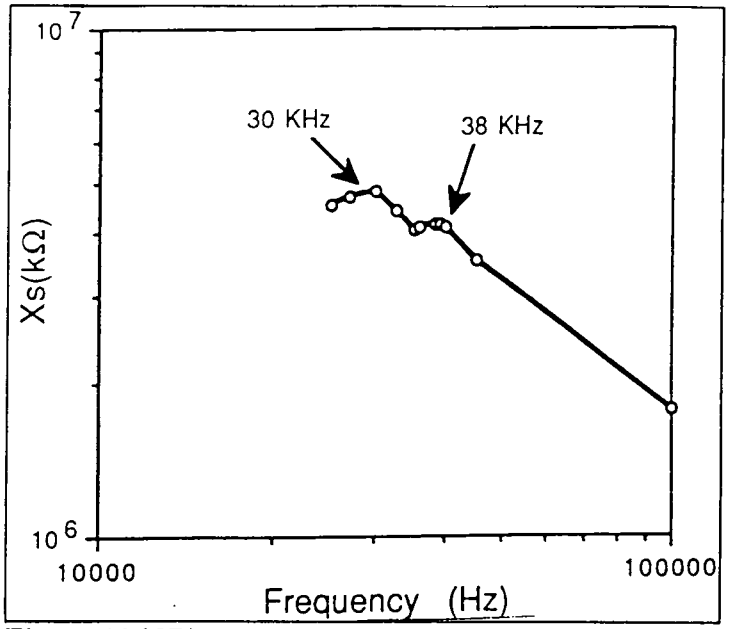

Figure (6.13B) : Reactance (Xs) versus frequency from impedance studies for 5% Nb_2O_5-doped sample.

Figure (6.14) shows the corresponding complex impedance plot for a less heavily doped sample (1% Nb_2O_5). The magnitude of the real and imaginary impedances were lower than for the more highly doped material, as expected from the

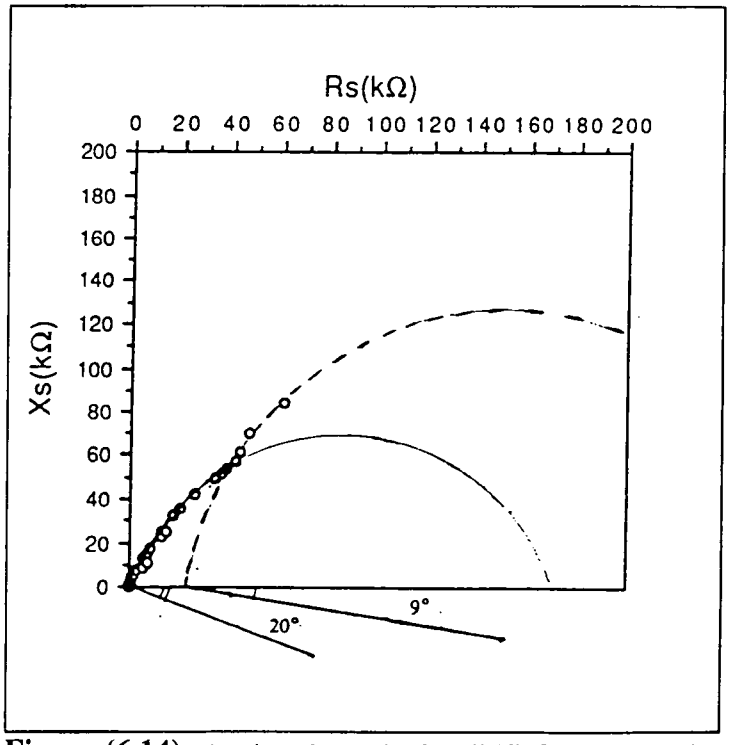

Figure (6.14) :A.c. impedance plot for 1% Nb_2O_5-doped sample.

d.c. conductivity measurements (figure (6.7)).

The data still appear to lie on two interpenetrating semi-circles but the degree of overlapping was greater preventing a more detailed analysis to be made. However, it is clear that the bulk resistance (Ro) was essentially zero as was the case for undoped and 5% Nb_2O_5 material.

6.7.3b - Discussion :

The interpretation of complex impedance diagrams was described in full, in chapter V. It was shown that the various physical processes governing charge transport may be represented by appropriate RC circuit elements, each of which gives rise to a semi circle in the impedance plot. The corresponding R and C values etc. for the data in figure (6.13A) are listed in table (6.3). Comparison with the corresponding values for undoped material (chapter V, table (5.2)) shows :

(i) The values of R_1 and R_2 were greater, for the doped material;

(ii) The value of f_1 was reduced from 160 KHz in the undoped sample to 38 KHz in the doped sample, see figure (6.13B);

(iii) The value of f_2 remained essentially unchanged with doping. That the resistance values for the doped material were higher is consistent with the results from the d.c. measurements, figure (6.7), which showed that the resistivity increased with doping level above about 0.5% Nb_2O_5. It would have been of interest to have compared a.c. impedance data for less heavily doped material, but as discussed above, it was not possible to analyze this data.

The reduction in the frequency f_1 with doping indicates that the underlying physical mechanism was sensitive to the doping level, whereas that associated with f_2 was apparently not affected. It is possible that f_2 is associated with the hopping process, since this was also apparently not dependant on doping. On the other hand the physical process associated with f_1 did appear to be dependent on doping. One possibility was that it was associated with grain boundary effects which would be

expected to change with doping.

Table (6.3) :A.c. impedance results for sample doped with 5% Nb_2O_5.

This data for sample was doped with 5% Nb_2O_5			
Parameters	Values	Parameters	Values
f_1	38 Khz	R_2	$9.6 \times 10^6\ \Omega$
f_2	30 Khz	X_{s1}	$3.95 \times 10^6\ \Omega$
ω_{o1}	2.39×10^5 Hz	X_{s2}	$4.8 \times 10^6\ \Omega$
ω_{o2}	1.89×10^5 Hz	C_1	3.99×10^{-9} F m^{-2}
R_o	~ zero	C_2	4.14×10^{-9} F m^{-2}
R_1	$7.9 \times 10^6\ \Omega$	ε_s	7.268×10^{-11} F m^{-1}

6.8 - Characteristics of In-doped Zn_2SnO_4 :

6.8.1 - Structure:

Some changes were observed to take place after doping with In from the vapour phase, which were outlined in section (6.5). The sample colour changed from white to dark grey, but SEM study failed to reveal any changes in the usual grain size average, which were ~ 1-15 μm in size.

The EDAX results, figure (6.15), did not show any presence of the In, and the intensities of the Zn and Sn peaks remained the same as un doped Zn_2SnO_4. This result may be due to the amount of indium in the zinc stannate compound, which was thought to be less than the level of detection of the EDAX instrument (1%). Furthermore the X-ray diffraction pattern did not indicate any additional phase, indicating that new compounds had not been formed. Peaks relating to In metal were also not found. Again it could be related to the small amount of indium in the Zn_2SnO_4.

6.8.2 - D.C. Transport Measurements :

It was found that the conductivity was increased with increasing temperature, showing semiconducting behaviour, but the mechanism was not simply activated. Figure (6.16) shows a plot of $\ln \sigma T^{1/4}$ versus $1/T^{1/4}$, showing the typical behaviour for hopping mechanism [6.8]. This result in consistent with the corresponding study of Nb_2O_5 doped (6.7.2a) and un doped samples.

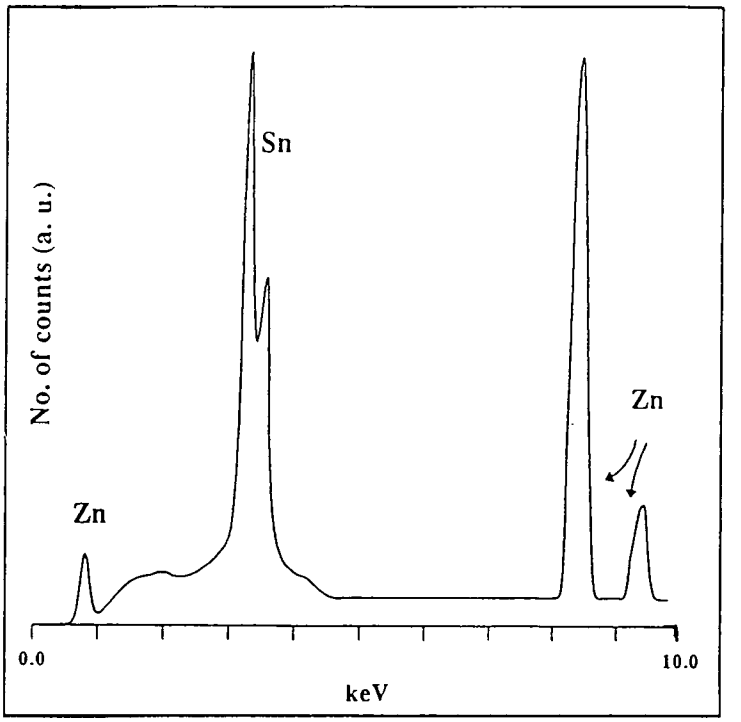

Figure (6.15) :EDAX spectrum for the general surface area of an In-doped sample.

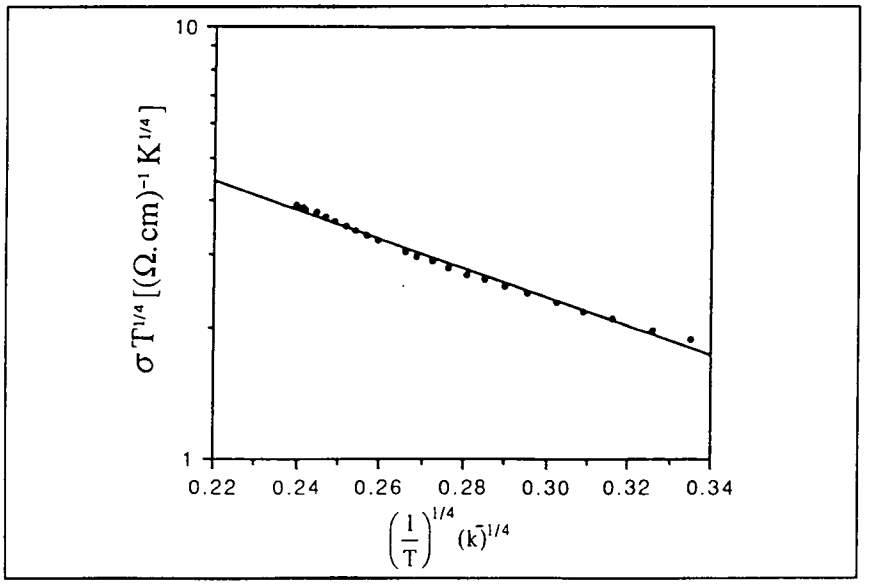

Figure (6.16) : Conductivity -Temperature characteristics for an In-doped sample.

6.8.3 - Au/Zn_2SnO_4:In/In.Ga Diode Characteristics :

6.8.3a - Au/Zn_2SnO_4:In/In.Ga. diode preparation:

Rectangular ($13 \times 5 \times 1.5$ mm^3) samples of Zn_2SnO_4 were cut, lapped, cleaned, and chemically etched in $1HF : 1HNO_3 : 4CH_3COOH$. They were then rinsed in methanol and blow dried in a steam of nitrogen. The samples were then doped with In from the vapour phase as outlined in section (6.5). In principle high work function metals, such as Au should make barrier contacts to n-type semiconductors, and gold was therefore used for the rectifying contact. The Au was deposited by vacuum evaporation at a pressure of 0.6×10^{-4} mbar. Ohmic back contacts were fabricated with an alloy of 2 : 1 indium : gallium.

6.8.3b - Au/Zn_2SnO_4:In/In.Ga. diode characteristics :

Au/Zn_2SnO_4 junctions were characterised using current - voltage and capacitance - voltage measurements. Both analysis techniques were carried out at temperatures in the range 77 - 300K in about 10K steps. It was hoped in this way, to obtain some data on doped material for the first time and to provide some indication of the efficiency of the doping process.

6.8.3c - Au/Zn_2SnO_4:In/In.Ga. Diode Performance :

Figure (6.17) shows the I-V characteristics of a typical Au/Zn_2SnO_4 diode at 77K and at room temperature. The characteristics were rectifying at both temperatures, although significant leakage was observed at reverse bias voltages greater than about -0.5 V figure (6.18). The forward bias characteristics show relatively little dependence on temperature (Figure 6.19) over the range 77K - 300K. The corresponding saturation current (Io) and ideality factors are listed in table (6.4). The ideality factor n was calculated from the slope of the $\ell n(I_f)$ versus 1/T

characteristics for V ≥ 0.12 volts. It is clear from figure (6.20) and table (6.4) that n changed with the temperature, decreasing with increasing temperature, with values of $4 \leq n \leq 15$ at a temperature range of $77K < T < 300K$.

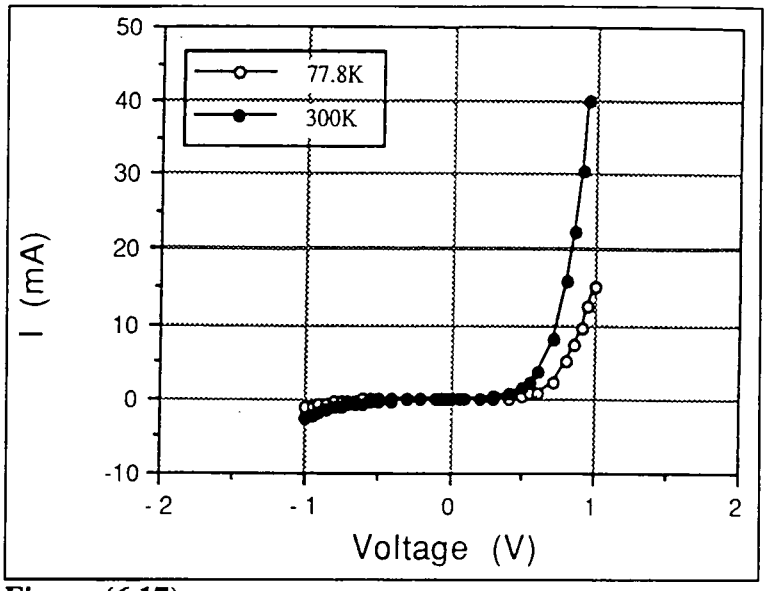

Figure (6.17) : I-V characteristics for a typical In-doped M.S. diodes.

Diode ideality factors have not hitherto been reported for (Au/Zn_2SnO_4-diodes), but these values indicate that transport across the junction was clearly not limited by emission over the metal - semiconductor barrier. A straight line relationship was not obtained when ℓn Io was plotted against reciprocal temperature (1/T), confirming the absence of thermal activation within the junction.

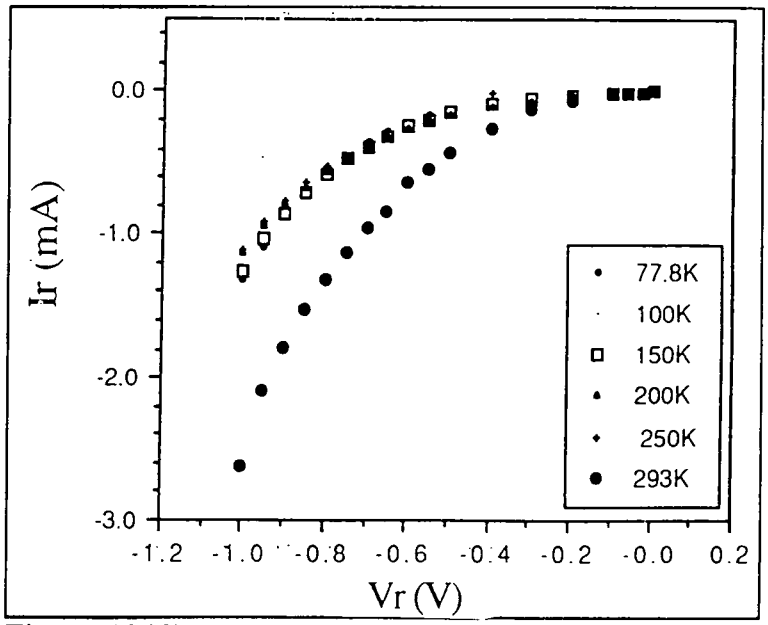

Figure (6.18) : I_r(reverse current)-V characteristics for a typical In-doped M.S. diode as a function of temperature.

The slopes of the Ln I versus V characteristics, however, were similar (see table (6.4)) and this would be consistent with a tunnelling mechanism described by an equation of the form [6.10,6.11]:

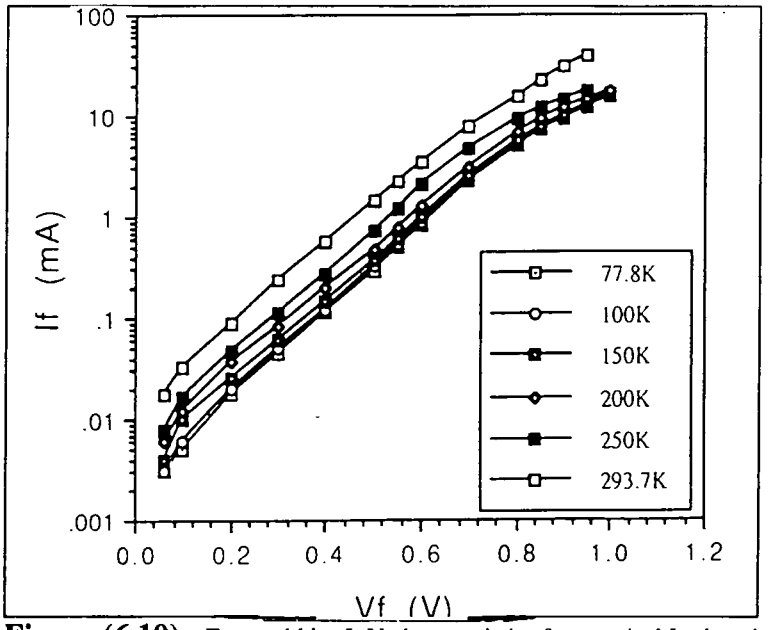

Figure (6.19) : Forward bias I_f-V characteristics for a typical In-doped M.S. diode as a function of temperature.

$$I_f = I_{oo}(T)\exp(BT)\exp(AV) \qquad (6.3)$$

In this case the intercept values C ≡ Io should show an exponential dependence on the temperature, and a graph of $\ln(I_O)$ versus T is shown in figure (6.21) and does show a reasonable straight line, although there is some scatter in the points. The slope (B) of the line is 0.01 K^{-1} which is comparable with values commonly observed in heterojunctions where

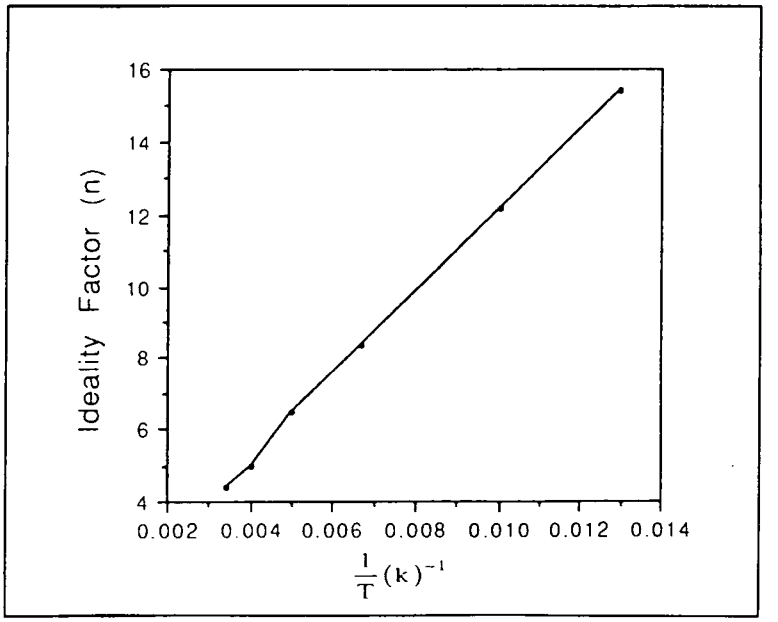

Figure (6.20) :Ideality factor (n) versus (1/T) for In-doped M.S diodes (V>0.12V).

transport is limited by some tunnelling - recombination mechanism [6.12].

Table (6.4) : Saturation currents and ideality factors for Au/Zn_2SnO_4:In/In.Ga diodes.

No.	T (K)	n	Slope (ln I vs. V)	Io μA
1	77	15.41	9.8	2.5
2	100	12.14	9.6	3.0
3	150	8.38	9.2	4.3
4	200	6.46	9.0	5.5
5	250	4.95	9.4	7.5
6	293	4.41	9.0	18.3

In practice, the probability for single step tunnelling is usually vanishing small in such a junction and it is usually necessary to develop a multistep tunnelling / recombination mechanism to describe the behaviour. This is, in reality a defect controlled junction where current transport occurs through interface / defect states, rather than by simple emission/ tunnelling processes. It is not,therefore surprising that this appear to be the case here, where bulk conductivity appeared to be dominated by hopping.

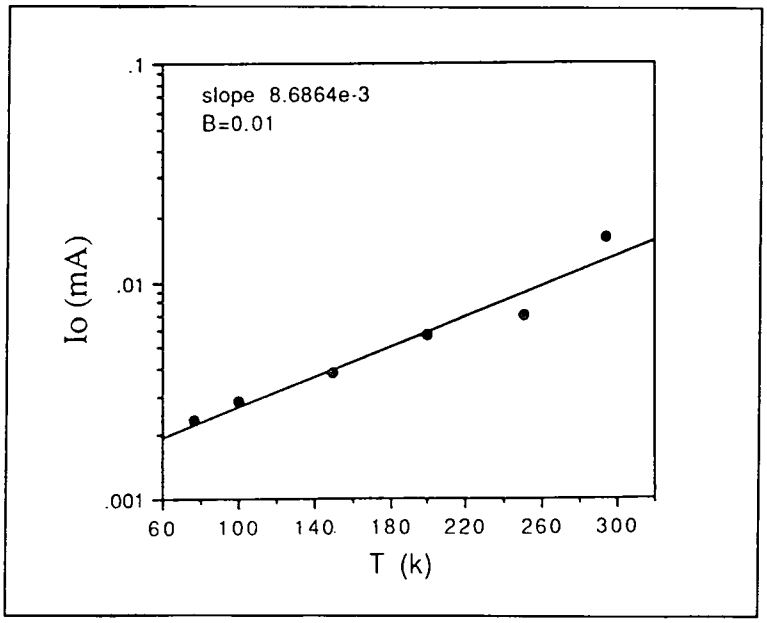

Figure (6.21) : A plot of Io with temperature for In-doped M.S diodes.

6.8.3d - C-V Characteristics :

Although transport across the junction was defect-controlled the C^{-2} (F^{-2} cm^4) versus V characteristics, displayed surprisingly good straight lines. Figure (6.22) shows a typical set of C^{-2} versus V characteristics for different temperatures. The net donor densities N_d were calculated from the slopes of the C^{-2} versus V curves in accordance with, the equation [6.13] :

$$\frac{d}{dV}\left(\frac{1}{C^2}\right) = \frac{2}{q\epsilon_s N_d} \qquad (6.4)$$

The values are listed in Table (6.5) and plotted in figure (6.23) as a function of temperature and show that N_d increased with increasing temperature, changing from 8 x 10^{13} cm^{-3} to 4.5 x 10^{14} cm^{-3} as the temperature was raised from 77K to 300K. The values of N_d are relatively low and suggest that the material was compensated. It should be remembered that these devices were sintered ceramics and not homogenous crystals and there will therefore be a higher degree of uncertainty in the measured values. From figure (6.23) the apparent activation energy was 17 meV which is small and would suggest total ionisation at room temperature.

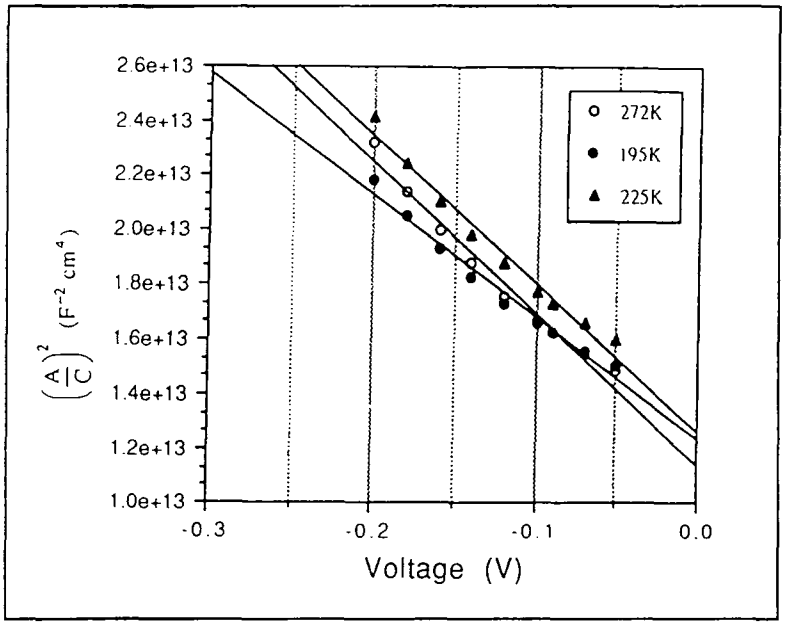

Figure (6.22) : The C^{-2} versus V curves for a Au/In-Zn_2SnO_4/In,Ga diode at different temperatures.

As the voltage tended to zero (figure (6.22)) the straight lines observed in C^{-2} versus

V plot became curved, possibly indicating interdiffusion at the junction or more

Table (6.5) : C-V data for In doped Zn_2SnO_4 diodes.

No.	T°K	$C_{v=0}$ F m^{-2}	N_d cm^{-3}	W cm	V_i v
1	80	4.28×10^{-7}	7.99×10^{13}	4.47×10^{-6}	0.45
2	100	3.45×10^{-7}	1.19×10^{14}	5.54×10^{-6}	0.46
3	120	3.23×10^{-7}	1.63×10^{14}	5.93×10^{-6}	0.38
4	148	2.72×10^{-7}	2.87×10^{14}	7.03×10^{-6}	0.31
5	195	2.62×10^{-7}	2.92×10^{14}	7.31×10^{-6}	0.27
6	225	2.77×10^{-7}	3.53×10^{14}	6.90×10^{-6}	0.23
7	245	2.72×10^{-7}	4.92×10^{14}	7.03×10^{-6}	0.17
8	272	2.89×10^{-7}	3.59×10^{14}	6.63×10^{-6}	0.21

probably a high density of surface states at the interface between the Au and the Zn_2SnO_4. Extrapolation of the straight line section of the C^{-2} versus V plot gave a value of the voltage intercept of (0.23 volt $\leq V_i \leq$ 0.445 volt) as listed in table (6.5). This is often taken as a measure of built-in voltage at the diode junction, although this value is sensitive to interface states [6.14]. The values in table (6.5) show that the extrapolated intercept values decreased with increasing temperature suggesting that interface states were active. The rate of change of the extrapolated intercept with temperature is not constant throughout the whole temperature range.

The depletion region width was inferred from the conventional formula [6.13] :

$$\left(\frac{C}{A}\right)_{(v=v_0)} = \left(\frac{\epsilon_s}{W_{(v_0)}}\right) \qquad (6.5)$$

The values of zero bias capacitance are listed in table (6.5) and varied significantly with temperature to give a corresponding range of depletion widths of 4.5×10^{-6} cm $\leq$ W $\leq 7.3 \times 10^{-6}$ cm which are very small, as would be expected.

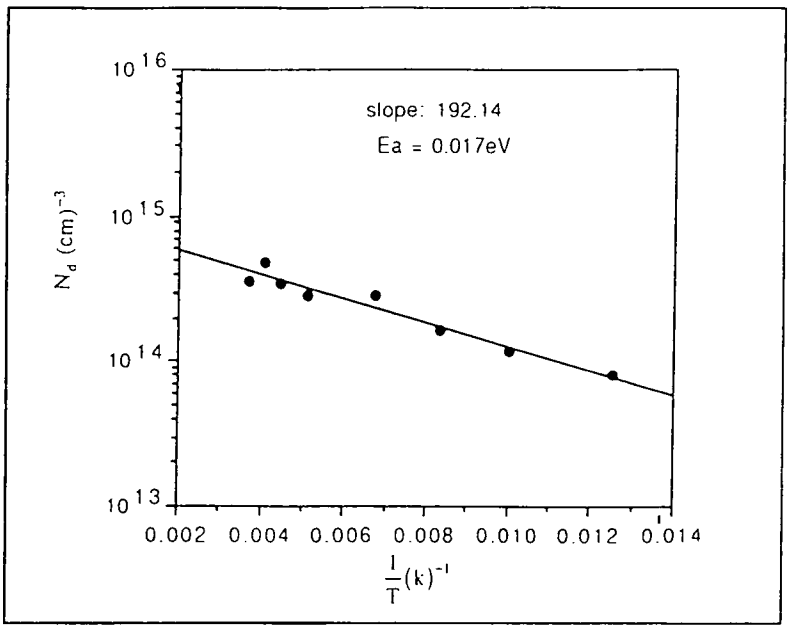

Figure (6.23) : Log N_d (from C-V study) versus 1/T for In-doped Zn_2SnO_4 diodes.

6.8.4 - Discussion :

Since the In doped Zn_2SnO_4 did not show any change in the structure, this may due to the low doping temperature, which was 350°C (see section (6.5)), considerably lower than the sintering temperature, which was 1280°C.

This type of doping was successful in terms of reducing the resistivity, since the resistivity changed from $\sim 10^6$ MΩ cm to ~ 3 Ω cm. This kind of reduction in the resistivity thought to be achieved by two ways, (i) by the indium, (ii) the effect of heating the sample in vacuum. The Indium was the most effective component in the process, because when comparison was made with samples heated in the same conditions without indium but in vacuum only, the samples still gave a relatively high resistivity (about 600 Ω cm).

6.9 - Summary :

The investigation of the effects of dopant type and dopant concentration, described in this chapter, have shown some changes in the resistivity and the colour. The most important data are summarised in table (6.6).

Additional peaks in the X-ray diffraction spectrum were not observed for In-doped and for low concentrations of Nb_2O_5, Ta_2O_5, V_2O_5, etc, implying monophase material. Some new peaks appeared in the XRD spectrum for samples that had been heavily doped with Nb_2O_5 and V_2O_5. The additional phase which observed in the Zn_2SnO_4 heavily doped with Nb_2O_5, was found to be close to $Sn_2Nb_2O_7$. However, it was not possible to identify the additional phases in the samples heavily doped with V_2O_5.

SEM examination showed almost the same results as for the undoped samples, and the average grain size was still the same (1-15 μm) for all types of doping, except for the V_2O_5 doped samples. Liquid phase sintering was observed to be the dominant sintering processes for V_2O_5-doped Zn_2SnO_4 samples. Since In-doped samples were not exposed to high temperatures, then SEM failed to indicate any change in the grain size.

EDAX studies confirmed the presence of Nb in heavily Nb_2O_5-doped samples, when the doping level began to exceed 1%, and the Nb peak in the EDAX spectrum became more intense as the Nb concentration was raised to 10% Nb_2O_5. A similar pattern was found with V_2O_5-doped samples as well. But since the amount of In was small, it was difficult to confirm its presence by EDAX, since the concentration was below detection limits.

Nb_2O_5-doping caused a colour change, going from white to a dark grey as the doping amount was increased, but the doping did not reduce the resistivity and the samples still displayed a high resistivity. Measurable electrical conductivity could not be obtained unless a reduction treatment was carried out. In this case, carrier mechanism was found to be variable range hopping, as described in chapter V for the

undoped material. This was further supported by some Hall coefficient measurements, which indicated a high carrier concentration ($\sim 10^{18}$ cm^{-3}) that was insensitive to the measurement temperature.

$TaCl_5$ was found to be of little use, since $TaCl_5$-doped samples failed to sinter after the usual firing procedures. This was not found to be the case with Ta_2O_5, although no significant change of colour or conductivity was observed in the Ta_2O_5-doped sample.

The In-doped samples showed a dramatic change in colour and resistivity, with the colour being changed from white to grey, and the resulting ceramic becoming conductive without further treatment (see table (6.5)).

In conclusion, it would appeared that only In was successful in reducing the resistivity of Zn_2SnO_4. Moreover, In doping was found to be stable even when heated to relatively high temperatures ($\sim$ 600°C) in an oxidising ambient (air). The change of colour observed with Nb-doping did indicate some reaction had occurred, but this did not produce the required reduction in resistivity.

Table (6.6) : Summary of doping characteristics.

Doping								
Type	Method	Electrical Conductivity (Ω cm)$^{-1}$						Structure
		Doping Mol Ratio						f.c.c. Inverse Spinel Type
		0%(Un-doped)		0.5%		1.5%		
		80°K	300°K	80°K	300°K	80°K	300°K	
Nb_2O_5	Mix.(i)	0.2	1.1	1.4	3.2	0.1	1.14	" + (iii)
Ta_2O_5	"			0.36	4	0.56	2.95	Mono-Phase
V_2O_5	"			0.02	0.1	2e-6	8e-6	" + (iv)
In	V.P.(ii)	80°K		300°K				Mono-Phase
		0.6		0.9				

(i) - Mixed Powders Of Dopant and Zn_2SnO_4.
(ii) - Vapour Phase Method.
(iii) - Additional phase, (possibly $Sn_2Nb_2O_7$).
(iv) - Additional un-known phase.

6.10 - References :

[6.1] - Koffyberg F.P. and Bento F.A., Appl. Phys. Lett., **37**, 320, (1980).

[6.2] - Sumitomo Aluminium Smelting, Kokai Tokkyo Koho, **JP 59-54, 954**, (1984).

[6.3] - Sumitomo Electric Industries, Kokai Tokkyo Koho, **JP 83-35, 71**, (1983).

[6.4] - Illingsworth J., Hashemi T., Al-Shahrani A. and Brinkman A.W., Brit. Ceram. Proc. 49., Special Ceramics **9**, London, (1990).

[6.5] - Glot A.B., Proshkin Y.N. and Nadzhafzade A.M.,"Ceramic Today-Tomorrow's Ceramic", Elsevier Science Publishers B.V., Amesterdam, (1991).

[6.6] - Zuyao C., Ying J., Zude Z. and Yitai Q., J. China Unv. Sci. Tech., **17**, 343, (1987).

[6.7] - Yamaguchi O., Maruyama N. and Hirota K., J. Mater. Sci. Lett., **10**, 445, (1991).

[6.8] - Roberts G. G., Apsley N., and Munn R. W., Phys. Rep., **60**, 59, p108,(1980).

[6.9] - Illingsworth J., Al-Allak H.M., Brinkman A.W. and Wood J., J. Appl. Phys., **67**, 2080, (1990).

[6.10] - Ou S.S., Stasfudd O.M. and Basol B.M., Sol. Stat. Electron., **27**, 21, (1984).

[6.11] - Ercelebi C., Brinkman A.W., Furlong T.S. and Wood J., J. Crystal. Growth, **101**, 162, (1990).

[6.12] - Brinkman A.W., Al-Allak H.M., Awan G.R., Brown P.D., Durose K., Ercelebi C.E., Simmons M.Y. and Woods J., Int. J. Solar Energy, **12**, 233, (1992).

[6.13] - Sze S.M.,"Physics of Semiconductor Devices", (Wiley - Interscience, New York, (1969)).

[6.14] - Rhoderick E.H. and Williams R.H.,"Metal-Semiconductor Contacts", (Oxford Science Publication, Oxford, (1988).

CHAPTER VII

ZINC STANNATE THIN FILM PREPARATION AND CHARACTERISATION

7.1 - Introduction :

Electroceramic thin films are currently used in a wide range of electronic and optical devices. Ceramic films are also used in electronic devices as mechanical supports, diffusion barriers, intermediate layers in epitaxial growth (buffer layers) and dielectric layers [7.1]. As in electronic applications, ceramic films in optical applications can also be either active or passive. Active ceramic films are being developed for non-linear optical devices, such as thin film lasers (e.g. Ti-doped sapphire) or electro-optic switches (e.g. lithium niobate) [7.1]. For these applications epitaxial , or highly oriented films are required. Indium-doped tin oxide is used widely as a transparent electrode and thin film electro-chromic ceramics are being developed for 'smart' windows. Passive films are used in reflective and antireflective coatings. Typical materials here are silica and titania in multilayer stacks of precise thickness and uniformity [7.1].

The increasing need for transparent conductive films in many applications has led to the development of materials with high performance, such as CdO-SnO_2 [7.2,7.3] and Al-doped ZnO films [7.4,7.5]. Enoki et al. [7.6] was the first to report (in 1992) the formation of SnO_2-ZnO thin films using rf sputtering from sintered oxide targets. They measured the electrical resistivity, and the transmission spectrum of such films in the 200 nm to 1100 nm wavelength region. No systematic study of Zn_2SnO_4 formed by electron beam evaporation has been found in the literature.

The initial plan for the research described in this chapter was simply to study the possibility of forming Zn_2SnO_4 thin films by electron beam evaporation. In the present chapter we will describe the formation of Zn_2SnO_4 thin films on cleaned glass and quartz substrates, and briefly outline the principles and technological feasibility of electron beam evaporation of sintered powders of zinc stannate. We report the

confirmation of Zn_2SnO_4 formation as a thin film using X-ray diffraction. EDAX was used to determine the composition. The thickness of each film was measured and a systematic investigation of the electrical and optical properties of as-deposited Zn_2SnO_4 thin films formed using substrate temperatures ranging from room temperature to 250°C.

7.2 - Experimental Procedure :

7.2.1 - Substrate Cleaning :

In most cases the substrates used were microscope slides, which are known to contain alkali ions (e.g. sodium) as revealed by ESCA. Diffusion of these ions into the film could be detrimental to film conductivity and could be a potential problem in applications requiring high conductivity. The diffusion between film and substrate is more likely at high temperature and hence deposition temperatures were restricted to below 250°C. The glass slides were cleaned rigorously in the following way :

(a) - Agitation in HNO_3 for 30 minutes. This leaches alkali ions from the substrate surface reducing the chances of alkali ion contamination in the deposited layers.

(b) - Reflux in trichloroethane. This acts to remove dirt and grease from the substrate surface.

(c) - Agitation in propan-2-o1 for 30 minutes. This acts to remove all materials used in the previous cleaning processes and leaves the substrate surface stain free and uniformly clear and smooth.

Between each cleaning treatment the substrate was washed in an ultrasonic bath of deionised water to avoid reaction between chemicals. Before fixing the substrate into the substrate holder, a nitrogen jet was used to remove any particles from the substrate surface.

7.2.2 - Electron Beam Evaporation :

Electron beam evaporation is one of the most commonly used evaporation techniques. An electron beam of sufficient intensity is emitted from a filament (cathode), accelerated and focused onto the target source (Zn_2SnO_4), which is used to heated at the site of incidence to the temperature required for evaporation. The method enables very high temperatures to be attained and evaporate materials which would otherwise be difficult to evaporate, especially ceramics which have high evaporation/ sublimation temperatures. More detail about the evaporator is given in chapter III.

The Zn_2SnO_4 samples to be used as evaporation sources were prepared by the sintering method described in chapter IV. The pellets were crushed using a mortar and pestle and placed in a small graphite crucible. Evaporation was carried out in an oil diffusion pumped system providing a vacuum of $\sim 10^{-6}$ mbar (base pressure).

The high temperatures are produced only at the point of electron beam focus. Ideally, this should be as near to the source surface as possible, hence it was necessary to modify the electron gun assembly so that it could move with respect to the Zn_2SnO_4 source, to allow the electron beam focus to be continuously adjusted during growth.

7.2.3 - Film Thickness Measurements:

The thickness of the films was measured using a Tencor Alphastep 200 Stylus profilometer. This required the formation of a step in the film across which the stylus of the profilometer could be drawn.

7.2.4 - Confirmation of Film Formation :

The crystal structure of the films was assessed by Reflection High Energy Electron Diffraction (RHEED) and X-Ray Diffraction (XRD). A comprehensive review of these techniques is available in [7.7,7.8].

XRD studies were carried out using a Philips diffractometer with a CoKα source and radiation with wavelength λ = 1.7902 Å. This technique was used to identify the material deposited, and to assess the degree of preferred order. The radiation penetrates films of up to a few microns thick, and the information obtained is an average of the entire film material. Only those planes parallel to the substrate contribute to diffraction intensities in an X-ray diffractometer (as opposed to a diffraction camera. This XRD is sensitive to any preferred orientation there may be in the layer. X-ray diffraction was also used to estimate the grain size from line broadening. Here the line width of a peak from a GaAs reference crystal is taken as being representative of the instrumentation broadening, on the assumption that GaAs is a near perfect crystal (infinitely thin line - in practice GaAs line widths are of a finite but very narrow width). It was assumed that line broadening due to lattice strain was absent. The relevant formulae are as follows :

$$\beta = \sqrt{B^2 - b^2} \qquad (7.1)$$

and

$$\psi = \frac{\lambda}{\beta \cos\theta} \qquad (7.2)$$

where β is the broadening factor, B is the full width half maximum (in radians) of the main peak in the spectra of Zn_2SnO_4 films, b is the instrmental broadening assumed to be the full width half maximum of the peak in the single crystal GaAs (i.e. reference). λ is the wavelength of the x-ray radiation, θ is the angle between the beam and the sample and ψ is the grain size.

7.2.5 - Electrical characterisation :

The resistivity of Zn_2SnO_4 films was generally measured using the Van der Pauw technique and for the more conducting samples the Hall coefficient, carrier concentration and mobility were also measured. (conductivity & Hall measurements

have been described in chapter III).

The resistivity and Hall measurements were made using an automated system, comprising an Archimedes computer, a constant current source, an overall controller, a magnet, a power supply and a cryostat. The sample was placed in the cryostat which could be evacuated down to $\sim 10^{-6}$ mbar and cooled to liquid nitrogen temperature.

7.2.6 - Optical Transmission Measurements :

Measurements of optical transmission were made using a Perkin - Elmer Lambda 19 UV/VIS/NIR spectrophotometer. This is a computer driven system capable of measuring transmission in the wavelength range 250 nm to 3.00 μm. The spectrophotometer is a double beam double monochromator type with a tungsten source for producing visible, near infrared, and a deuterium lamp for the ultra-violet radiation.

7.3 - Experimental Results :

7.3.1 - Film Deposition :

The film was deposited onto the glass slides using fine powders crushed from sintered pellets. Substrate heating was commenced after reaching desired vacuum, and the substrate was maintained at growth temperature for one hour before beginning the evaporation process. The e-beam source filament was also heated for at least half an hour before deposition.

After switching on the e-beam source, the shutter was left closed for 15 seconds to allow some outgassing of the source. When evaporation was complete, the shutter was closed and the e-beam source switched off. The substrate heater (when used) was then switched off and the substrate allowed to cool naturally to room temperature in vacuum.

Zn_2SnO_4 films were grown under a range of conditions, namely with and

without substrate heating, and using glass slides or quartz as substrate. Since as-deposited films tended to be fairly conductive, there was no need for annealing treatments as was the case for bulk materials, In fact, as the films had been deposited in vacuum, they were effectively already in the reduced state. The films which were produced at room temperature were silvery grey in colour and fairly opaque. Where a higher substrate temperature was used the films colour changed to a dark orange colour, and became more transparent.

Table (7.1) : Electron Beam Evaporating Conditions.

Filament	*Molybdenum*
Vacuum	*$\sim 10^{-6}$ mbar*
Substrate Heating Method	*Radiative*
Target-To-Substrate Spacing	*350mm*
Substrate	*Soda glass slides or Quartz*
Substrate Temperature	*RT (about 30°C) to 250°C*
Focusing Voltage	*$\sim$ 3kv*
Target Container	*Graphite*
Vacuum System	*Oil Diffusion Pump*

7.3.2 - Formation of Zn_2SnO_4 Thin Film Results and Discussion :

7.3.2a - X-Ray Diffraction :

Confirmation of the formation of the Zn_2SnO_4 compound as a thin film was obtained from X-ray diffraction spectra of as-evaporated films prepared by evaporating sintered powder of zinc stannate onto glass. Figure (7.1) shows the XRD spectrum for a film grown at room temperature. Four main peaks appear as can be seen from the XRD spectrum, see table (7.2), which illustrate a comparison with the x-ray diffraction pattern of sintered bulk material (see chapter IV), these peaks may be associated with Zn_2SnO_4. This spectrum was for films which were deposited onto glass substrates with temperature of T $\sim$ 30°C only (i.e. room temperature). XRD spectra could not be obtained from layers grown at higher temperature either because they were too thin or were not crystalline. Grain sizes were calculated from the x-ray

diffraction peak widths using the method outlined in section (7.2.4), and were in the range 20nm ≤ ψ ≤ 25 nm.

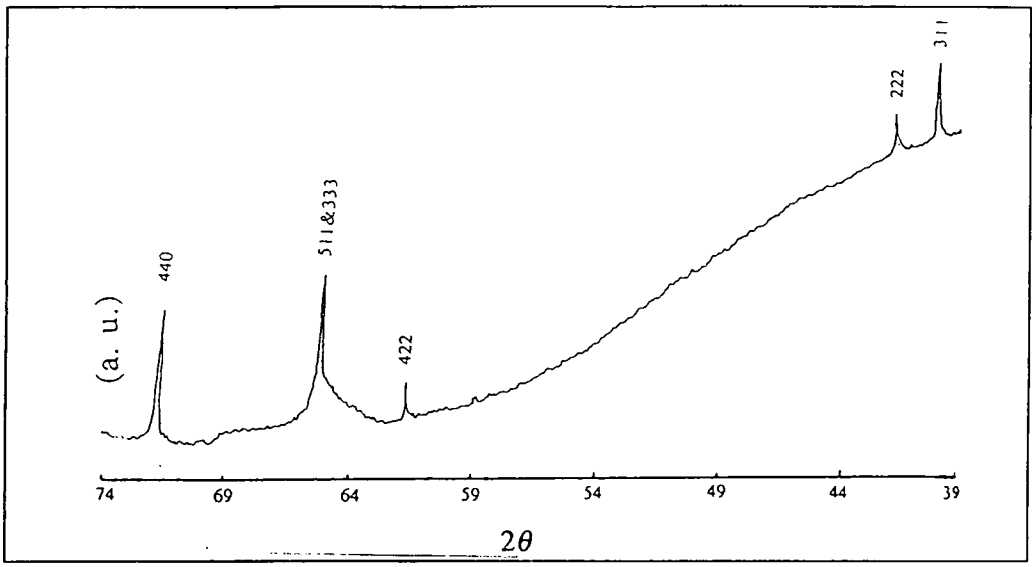

Figure (7.1) : X-ray diffractogram showing principal peaks of zinc stannate from a film grown at a substrate temperature of ~ 30°C.

Table (7.2): Summary of XRD Data for Zn_2SnO_4 thin film and bulk samples.

No.	h k l	2θ	d Å	
			Thin film	bulk
1	3 1 1	40.1	2.61	2.59
2	2 2 2	41.95	2.5	2.49
3	4 2 2	60.80	1.77	1.76
4	5 1 1 & 3 3 3	64.90	1.69	1.65
5	4 4 0	71.45	1.53	1.51
Lattice constant a = 8.65 ± 0.006 Å				
Rad. CoKα with λ = 1.7902 Å , Fe filter				

Note : 1) - Bulk 2ZnO : 1SnO_2 fired at 1280°C for 12 hours.
2) - Thin film was grown onto glass substrate temperature of ~ 25°C.

7.3.2b - Surface Structure by (RHEED) :

The surfaces of most of the films were examined in RHEED. Diffraction patterns could not be obtained from very thin film (thickness ≤ 50 nm) suggesting that they were probably amorphous or microcrystalline. This result was consistent with x-ray diffraction results. All the films showed complete semicircles, similar to those in figure (7.2) and figure (7.3), which show patterns taken from films grown onto glass substrates at room temperature and 200°C respectively. These patterns indicate that the films were polycrystalline, but with no strong preferred order. The increased 'spottiness' of the semicircles in the RHEED pattern from

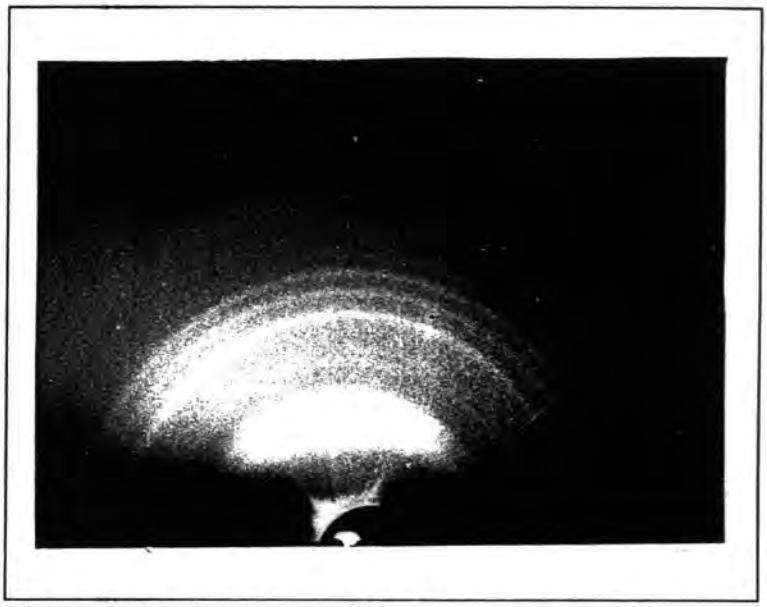

Figure (7.2) : RHEED pattern from a film grown at room temperature.

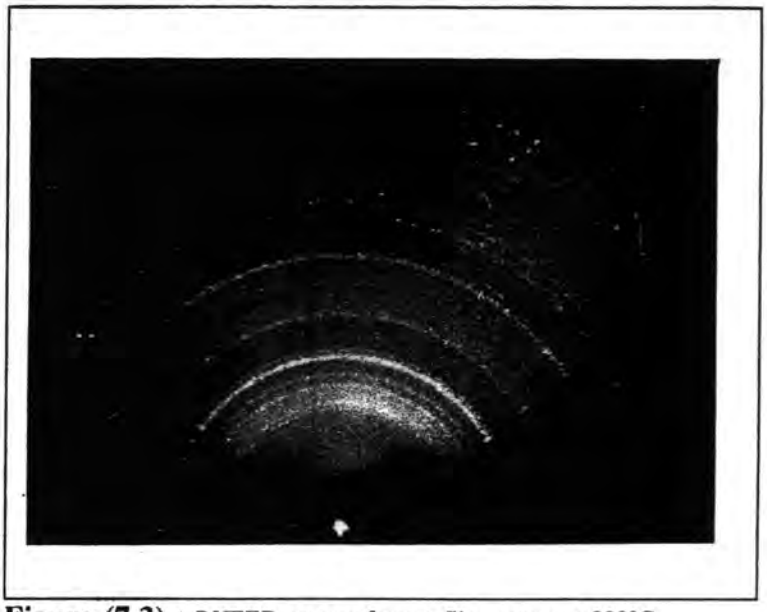

Figure (7.3) : RHEED pattern from a film grown at 200°C.

figure (7.3) (from a layer grown at 200°C) does suggest that grain size was larger in the films grown at higher temperature. The change in the relative brightness of the semicircles in figure (7.3) when compared with figure (7.2) may indicate the beginning of some preferred orientation. It is possible, that had the layer been grown at a higher temperature, it may have shown a more pronounced orientation.

7.3.2c - Microstructure characterisation (SEM, EDAX) :

Films were examined using a Cambridge Instruments S600 scanning electron microscope (SEM), in secondary electron emission mode. Figure (7.4) shows that the films were very flat and uniform. No evidence of cracks, grains, or second

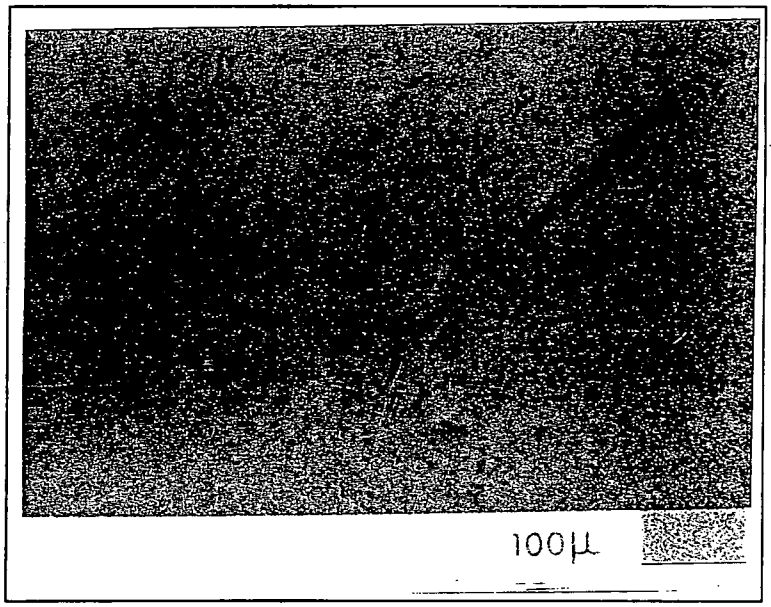

Figure (7.4) : Scanning Electron Micrograph of surface of a film grown at 200°C.

phases was found. In particular, there was no evidence for the formation of pinholes suggesting that film growth was continuous and that the layers were coherent. Elemental analysis of the layers by EDAX, figure (7.5) showed peaks due to Zn, Sn, and Si only. The Si peak, which was larger than expected, was probably due to the glass substrate. The Sn and Zn peaks were exactly the same as those found for bulk samples, and this result together with X-ray diffraction and RHEED results, further

confirms that the thin films were Zn_2SnO_4.

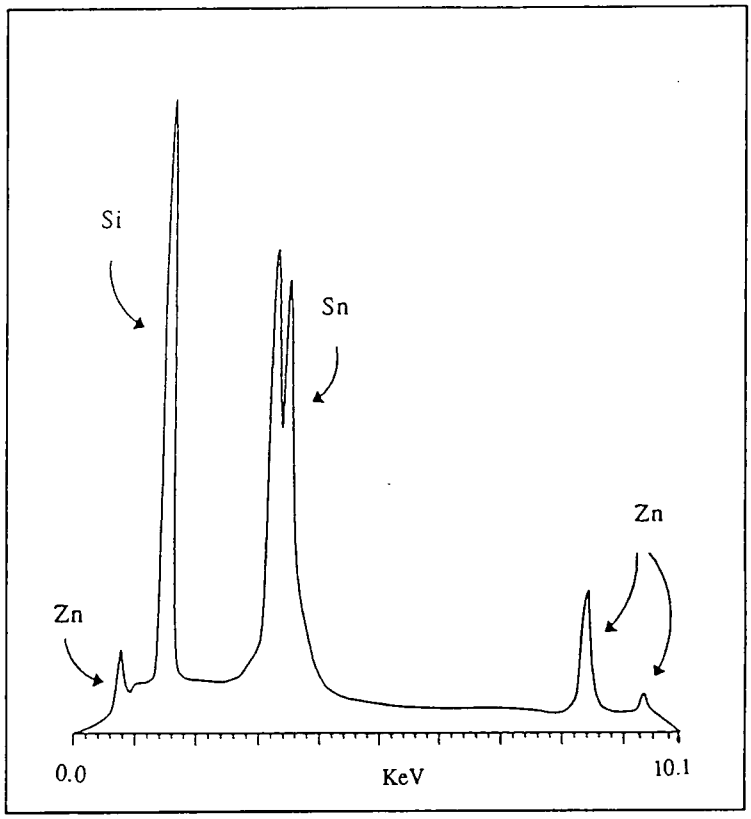

Figure (7.5) : EDAX spectrum of surface of a thin film of Zn_2SnO_4.

7.3.3 - Conductivity - Temperature Results and Discussion :

All of the films, involved in this study, were deposited onto glass substrates. The measurements were carried out using the Van Der Pauw configuration [7.9].

It was found that the conductivity - temperature characteristics of the films were broadly similar, independently of the substrate temperature during growth. Figure (7.6), shows the plot of conductivity versus reciprocal temperature between 77K and 300K for a thin film of Zn_2SnO_4 deposited onto a glass substrate, at a substrate temperature of 200°C. Figure (7.7) shows a similar plot obtained from a film deposited with a substrate temperature of $\sim$ room temperature, although the conductivity was a factor of 10 larger in this film.

In all cases the conductivity did not show a simple Arrhenius dependence, i.e. the conductivity did not obey the equation :

$$\sigma = \sigma o \exp(-\frac{Ea}{KT}) \quad ....(7.3)$$

where σ is the conductivity and Ea is an activation energy. Instead the relationship is better described by the $[1/T]^{1/4}$ dependence, seen for the bulk samples (chapter V) and characteristic of hopping as can be seen from figure (7.8). This conductivity - temperature dependence was essentially independant of thickness, and substrate temperature, see figures (7.8), figure (7.9). All films were found to obey the equation [7.10](for variable range hopping, see section 5.3.3):

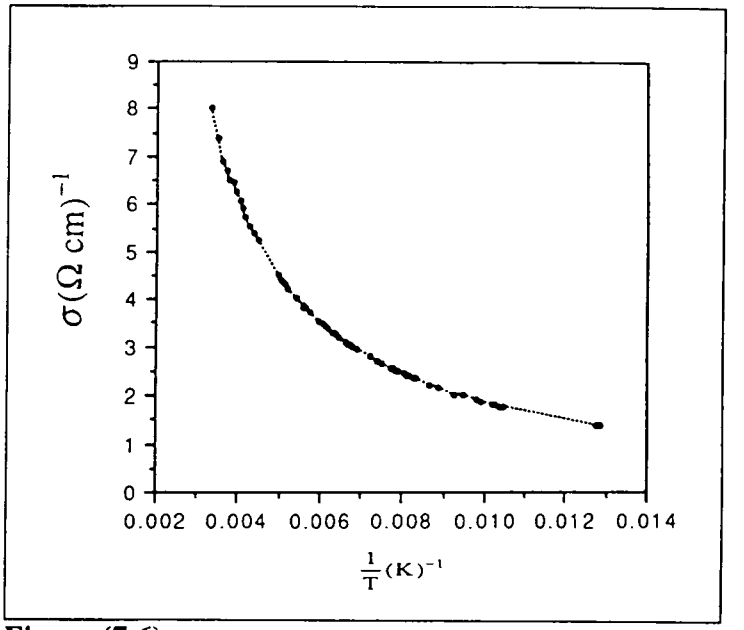

Figure (7.6) : Conductivity versus inverse temperature for a sample grown at 200°C.

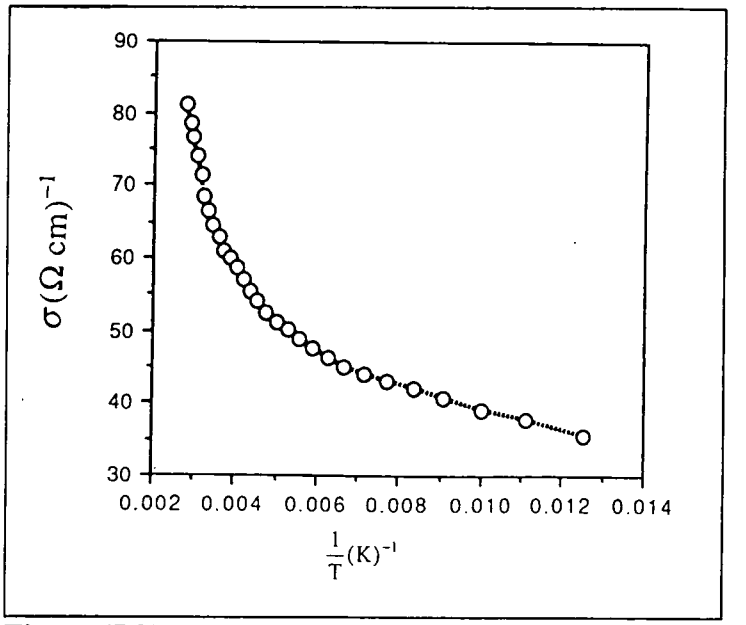

Figure (7.7) : Conductivity versus inverse temperature for a sample grown at room temperature.

$$\sigma = \left(\frac{Aq^2\alpha\nu To^{3/4}}{kT^{1/4}}\right)\exp\left[-\frac{To}{T}\right]^{1/4} \quad \text{.....(7.4)}$$

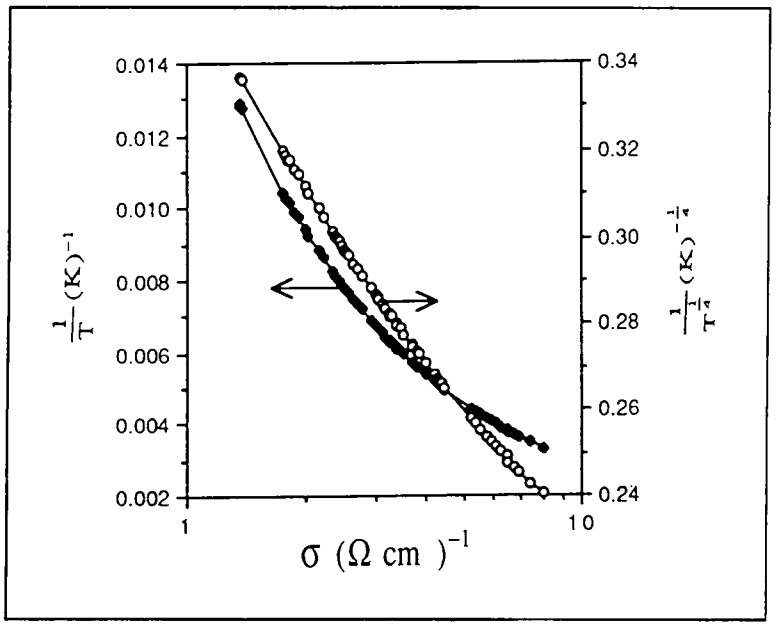

Figure (7.8) : Conductivity versus {(1/T) & $(1/T)^{1/4}$} for a film grown at 200°C.

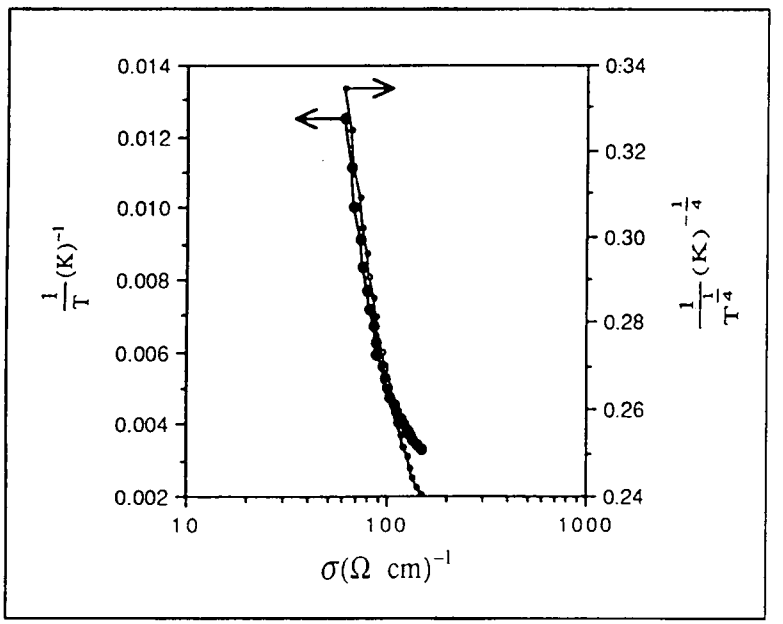

Figure (7.9) : Conductivity versus {(1/T) & $(1/T)^{1/4}$} for a film grown at room temperature.

Figure (7.10) shows the relation ℓog $\sigma T^{1/4}$ versus $(1/T)^{1/4}$, which is expected to give a straight line, from the equation (7.4), (see chapter V). Some values can be deduced from the straight line relationship between ℓn $\sigma T^{1/4}$ versus $(1/T)^{1/4}$. Values of To (from the slope) and σo (from the intercept) are given in Table (7.3).

This table shows that the To values increased with increasing substrate temperature. Suggests that To may be related to grain size, since this was shown by the RHEED studies to increase with increasing substrate temperature.

Similarly the decrease in σo values may be associated with grain size.

Although Hall measurements were attempted, the Hall voltages were very small making the measurements difficult, but indicating that the carrier concentrations were very high, ($n \sim 3 \times 10^{17}$ cm^{-3}). However the carrier concentrations were constant with temperature, as can be seen from figure (7.11). The mobility was very small $\mu_{eff} \ll 1$ (cm^2 V^{-1} s^{-1}). These results, high carrier concentration and low mobility, are consistent with a hopping mechanism.

Table (7.3) : Values of σo, To, and thickness for Zn_2SnO_4 thin films.

No.	Film No.	Substrate Temperature	Thickness (nm)	σo $(\Omega\ cm)^{-1}$	To (K)
1	3	200°C	230	5.43×10^3	2.22×10^5
2	95	~ 25°C	250	4.03×10^2	2.87×10^3
3	107	~ 30°C	150	1.18×10^4	2.58×10^4

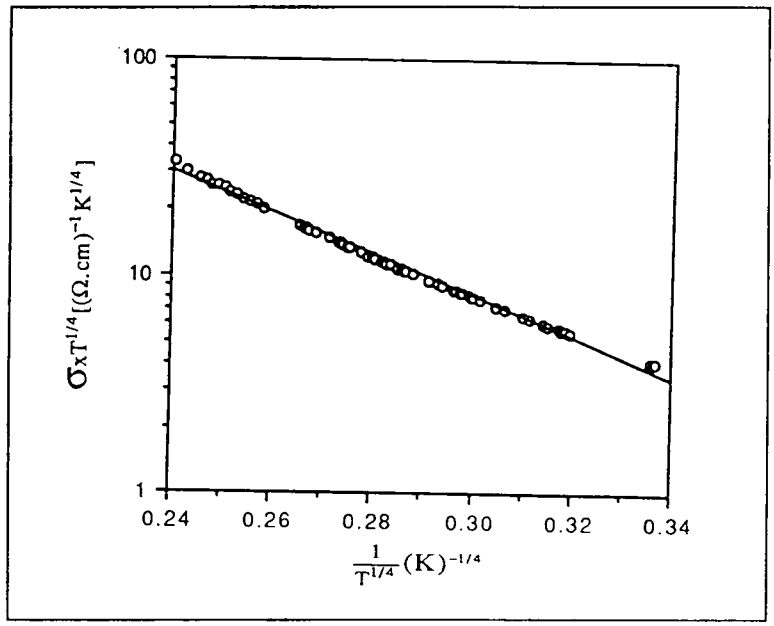

Figure (7.10) : {Conductivity × $T^{1/4}$ } versus $(1/T)^{1/4}$ for a film grown at room temperature.

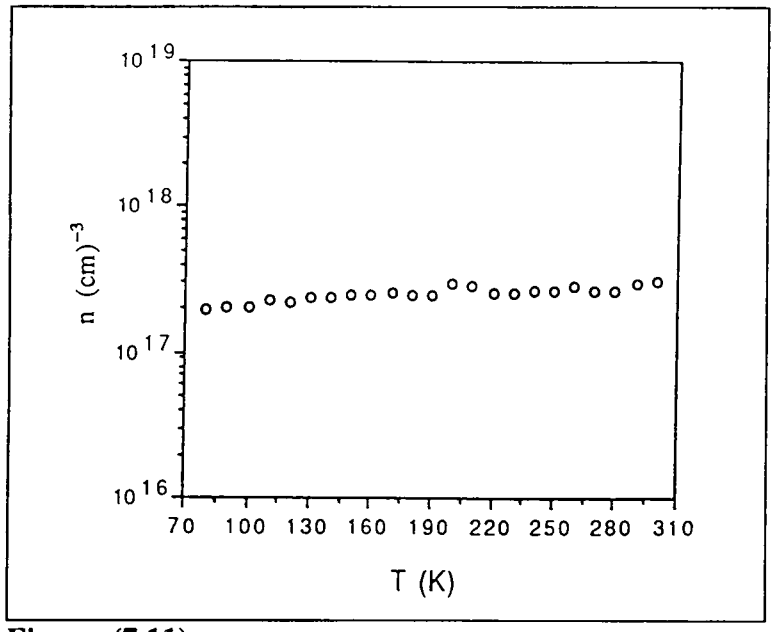

Figure (7.11) : Carrier concentrations versus temperature, for thin films of Zn_2SnO_4 grown at room temperature.

7.3.4 - Optical Transmission measurement results and discussion :

The optical transmission of the films was measured as a function of wavelength and used (see section 7.2.6) to obtain an estimate for the refractive index $n(\lambda)$, absorption coefficient $\alpha(\lambda)$, extinction coefficient $k(\lambda)$, and optical energy gap E_g.

The variation of transmittance T_α as a function of wavelength can be seen in figure (7.12) for three zinc stannate films grown at substrate temperatures of 50°C, 100°C and 200°C. The spectra show that the transmission T was significantly greater in the layer grown at 200°C, compared with layers grown at 100°C. However, there was little difference in the transmission of layers grown below 100°C. The transmission of layers grown at 200°C was very high, ($T \sim 88\%$) equivalent to that of other transparent conducting oxides such as ZnO, Zn_2SnO_4 or Cd_2SnO_4, over the

range of wavelength 1800nm ≤ λ ≤ 2500 nm [7.6]. These high values of transmissivity indicate that Zn_2SnO_4 might be useful for transparent electrodes if the electrical resistivity can be improved to the order of 10^{-4} Ω cm as has been reported by Enoki et al (1992) [7.6].

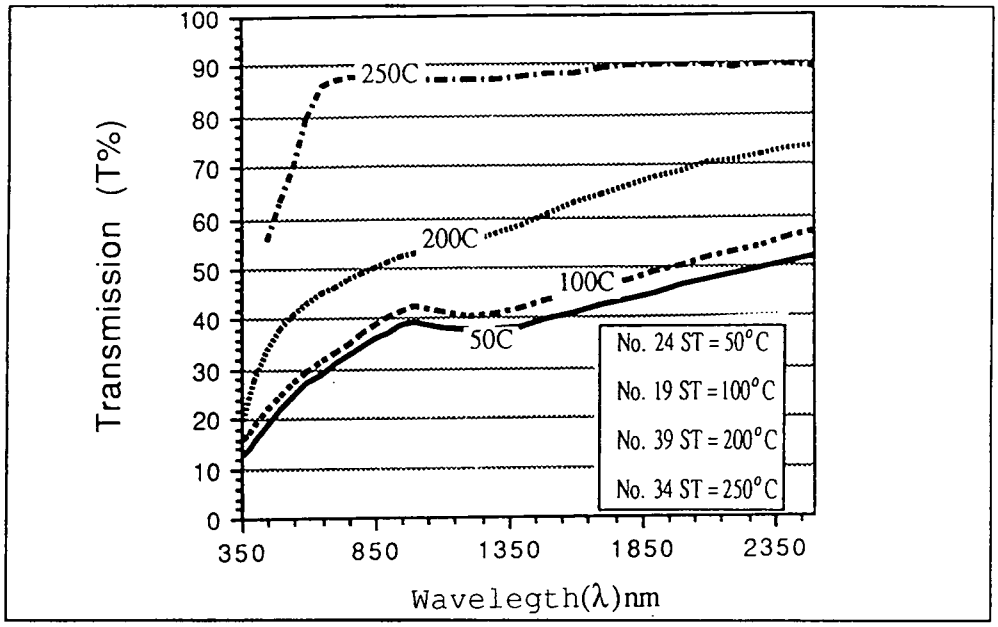

Figure (7.12) : Transmission (T%) versus wavelength (λ) for thin films of Zn_2SnO_4 grown at substrate temperatures between 50°C to 250°C.

Generally, the analysis of thin film transmission data is helped by the presence of interference fringes, which enable the optical constants to be determined more precisely. However, in the present case, there were no fringes and the analysis was based on the interference-free transmission, T_α, which is deduced from the interference equation [7.11,7.12] :

$$T = \frac{Ax}{B - Cx + Dx^2} \qquad (7.5)$$

where

$A = 16s(n^2+k^2)$

$B = [(n+1)^2+k^2][(n+1)(n+s^2)+k^2]$

$C = [(n^2-1+k^2)(n^2-s^2+k^2)-2k^2(s^2+1)]2\cos\phi - K[2(n^2-s^2+k^2)+(s^2+1)(n^2-1+k^2)]\sin\phi$

$D = [(n-1)^2 + k^2][(n-1)(n-s^2)+k^2]$

$\phi = 4\pi nd/\lambda$, $x = \exp(-\alpha d)$, $\alpha = 4\pi k/\lambda$ where s is the refractive index of the substrate, α is the absorption coefficient, d is the film thickness.

The equations, which were used to calculate all variables (n, k, α), in the transparent part of spectrum (α=0) are :

$$n = \{H+(H^2-s^2)^{1/2}\}^{1/2} \qquad (7.6)$$

$$H=\frac{4s^2}{(s^2+1)T_\alpha^2}-\frac{s^2+1}{1} \qquad (7.7)$$

Then α can be determined from the following equation :

$$T_\alpha=\frac{Ax}{[(B-Cx+Dx^2)(B+Cx+Dx^2)]^{1/2}}$$

.....(7 . 8)

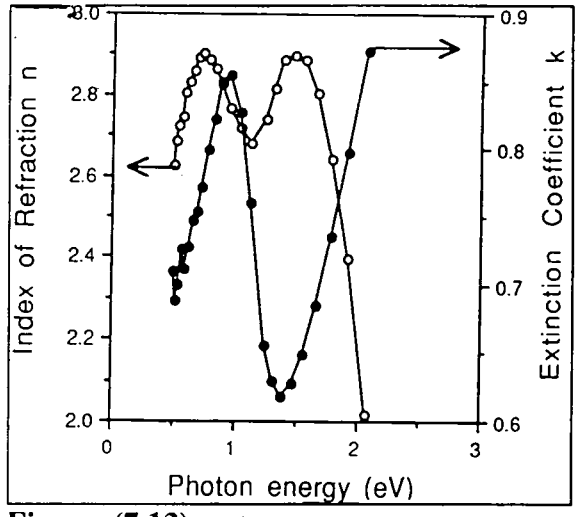

Figure (7.13) : Optical constants versus photon energy for a film grown at 50°C.

While the above works well when there is no absorption, it cannot be used to calculate n and x independently in the cut off region where there is strong absorption. From this region of the spectrum values of n were estimated by extrapolation from the values calculated in the transmitting part of the spectrum. The values of x can then be calculated using the formula for very large α ($x << 1$), in the form [7.12]:

$T_0 \approx Ax/B$ or

$$x\approx\frac{(n+1)^3(n+s^2)}{16n^2s}T_o \qquad (7.9)$$

Details of the derivation can be seen reference [7.12].

Figure (7.13), figure (7.14) and figure (7.15) show the n and k characteristics

of these layers grown at substrate temperatures of 50, 100, and 200°C respectively, all these characteristics show the presence of two peaks in the spectral dependence of n, at photon energies of ~ 0.8 and 1.6 eV with a minimum at ~ 1.2 eV. Interestingly the low energy peak decreased as the substrate temperature was increased. The k characteristics showed similar behaviour with a low energy peak at ~ 0.95 eV, a minimum at ~ 1.4 eV followed by a monotonic increase up to 2.5 eV (the limit of measurement range). The low energy peak increased in magnitude with decreasing substrate temperature. However the minimum decreased with decreasing substrate temperature making the "double peak" shape much more apparent. The variation in the values of k at photon energies of ~ 0.8 eV (i.e. vicinity of low energy peak) with substrate temperature is shown in figure (7.16) and demonstrates a systematic reduction as substrate temperature was increased. Clearly the film transparency was increased significantly at low photon energy as the substrate temperature approached ~ 200°C. The changes in the shape of the n and k characteristics suggest that true thin film formation did not take place until the growth temperature reached ~ 150°C. The XRD results, however, indicated that

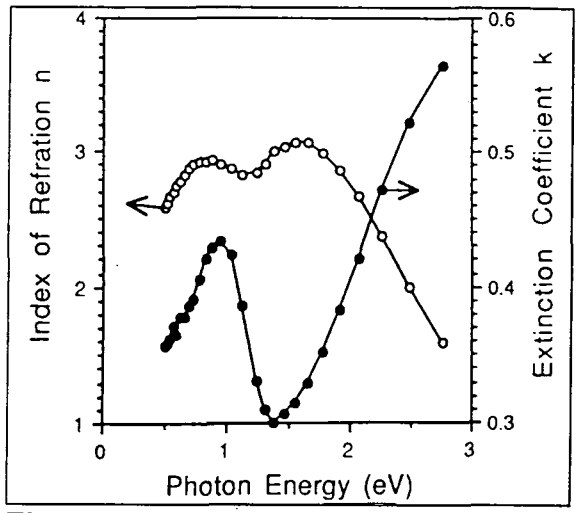

Figure (7.14) : Optical constants versus photon energy for a film grown at 100°C.

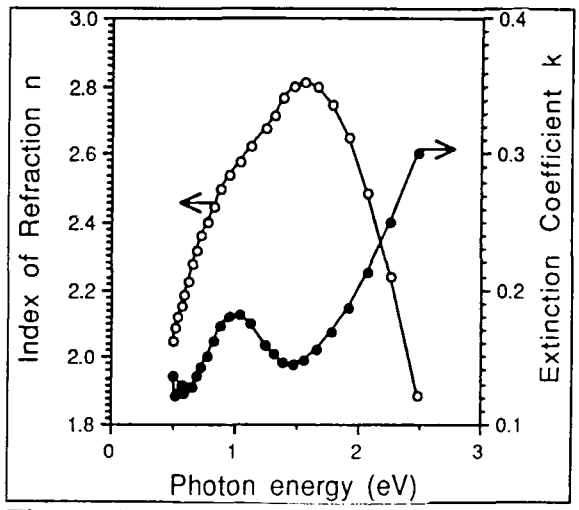

Figure (7.15) : Optical constants versus photon energy for a film grown at 200°C.

the low temperature film were Zn_2SnO_4 and the implication in that the film grown at lower temperature were in effect "powder films". Such films show greater effects due to scattering, which would tend to increase apparent k-values, as seen here.

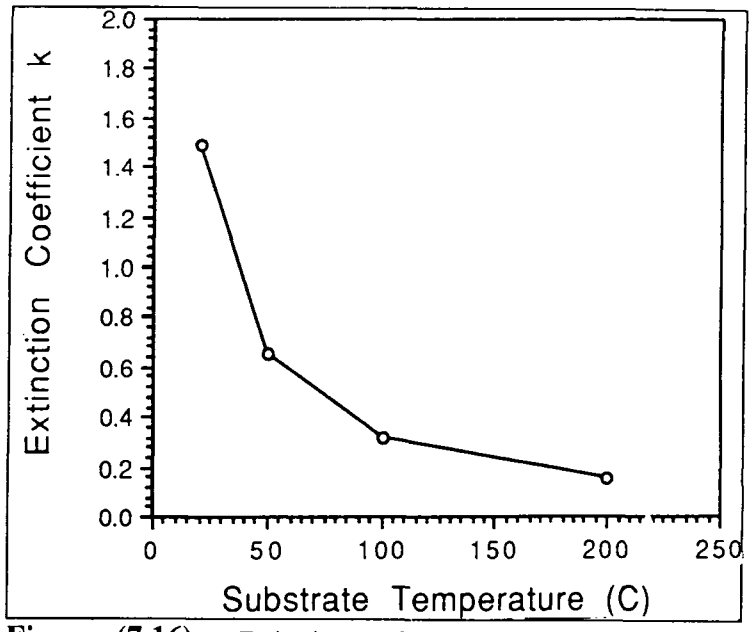

Figure (7.16) : Extinction coefficient (k) versus the substrate temperature for thin films of Zn_2SnO_4.

The results in the

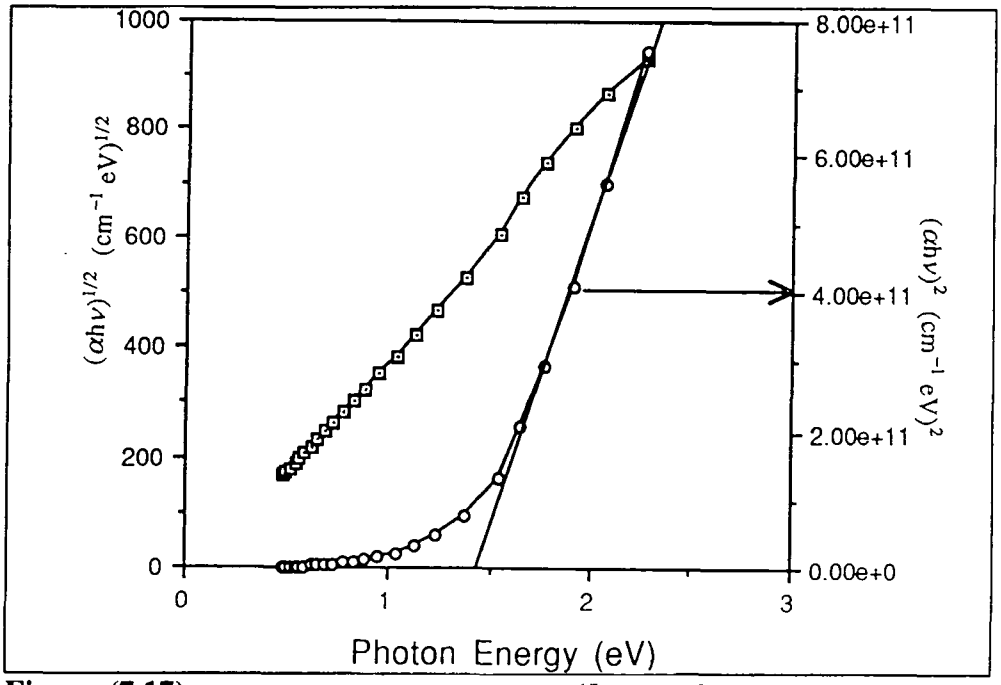

Figure (7.17) : Photon energy (hν) versus [$(\alpha h\nu)^{1/2}$ & $(\alpha h\nu)^2$] for a film grown at room temperature.

absorption region were analyzed using the relation :

$\alpha h\nu = A(h\nu - Eg)^{1/2}$ for direct band gap semiconductor behaviour [7.13,7.14] and

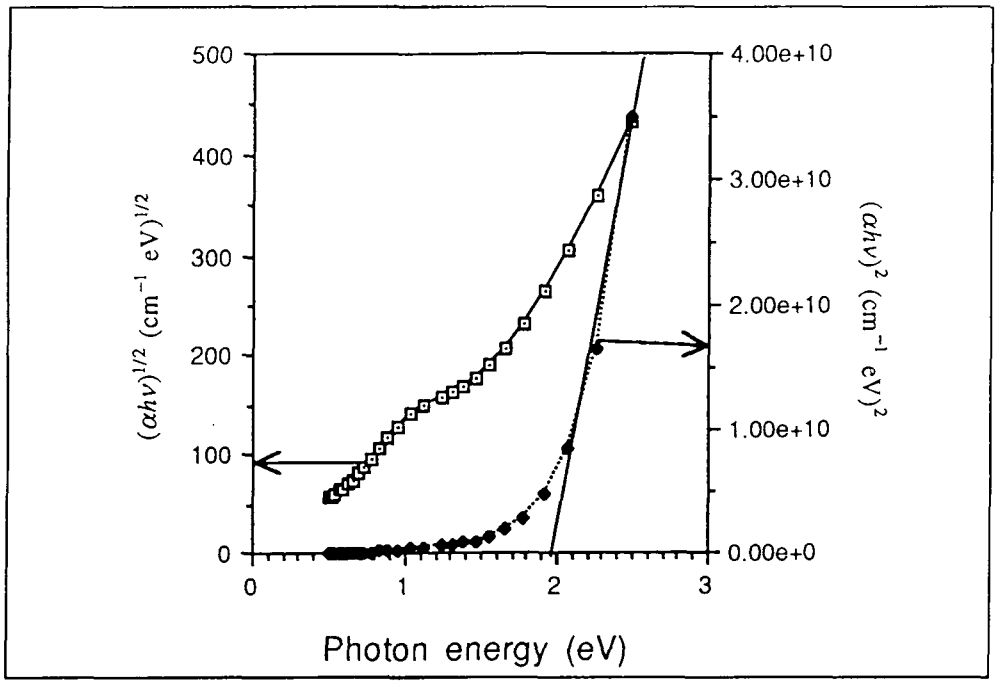

Figure (7.18) : Photon energy (hν) versus [$(\alpha h\nu)^{1/2}$ & $(\alpha h\nu)^2$] for a film grown at 200°C.

for indirect gap semiconductor behaviour using $\alpha h\nu = A(h\nu - E_g)^2$ [7.15]. Typical plots of $(\alpha h\nu)^2$ and $(\alpha h\upsilon)$ versus hν are shown in figure (7.17)(for a layer grown at a room temperature), and figure (7.18)(for a layer grown at 200°C), revealed the linear increase in $(\alpha h\nu)^2$ with hν beyond a certain photon energy 1.45 eV ≤ Eg ≤ 1.95 eV. The values of optical band gap Eg were estimated

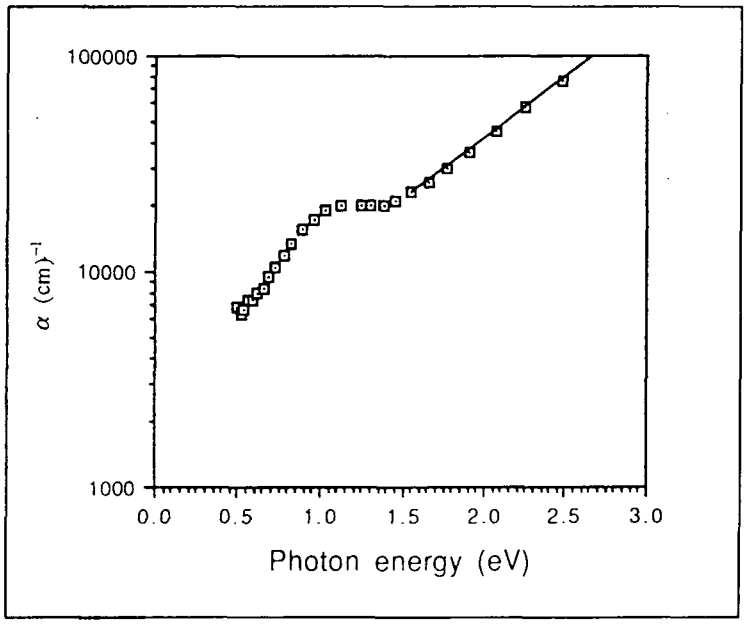

Figure (7.19) : Absorption coefficient versus photon energy for film grown at 200°C.

from the intercepts of the straight lines on the energy axis and are listed in table (7.4) for several layers grown at different substrate temperatures. Layers grown at temperatures greater than $\sim$ 100°C appear to have a direct energy gap of 1.95 eV. Layers grown below this temperature give a range of values suggesting that the k-values were being affected by scattering. It is also probable that the low temperature material may not have been fully homogenous. In the absorption tail region (800nm - 250nm), the variation of α versus hv for the polycrystalline films is similar in nature, and follows the Urbach relation given by :

$$\alpha = \alpha_o \exp\left[\frac{-B(h\nu_o - h\nu)}{KT}\right] \qquad (7.10)$$

where B is constant, and typical plots of $\ell og(\alpha)$ versus hv are shown in figure (7.19).

Table (7.4) : Values of energy gap, substrate temperature, and extinction coefficient for selected films.

Films No	Energy Gap Eg (eV)		Substrate Temp. (C)	Thickness (nm)	Extin. Coeff. k**
	Dirct	Indirect			
39	1.95	0.9	200	100	0.148
19	1.95	0.79	100	85	0.314
24	1.6	0.89	50	50	0.649
95	1.45	0.1	RT	250	1.49

** at λ = 800 nm.

A distinct linear variation is shown. The presence of an Urbach-type absorption tail and the steep increase in absorption beyond hv in figure (7.19) are generally observed for direct band gap compound semiconductor [7.13], [7.16], (Eg and k data are illustrated in table (7.4)).

7.4 - Summary :

The Zn_2SnO_4 thin films were prepared by Electron Beam Evaporation method using Zn_2SnO_4 sintered powder as an evaporant source material. The thin films were deposited on glass and quartz substrates with substrate temperatures (ST) 25°C ≤ ST ≤ 250°C.

Zn_2SnO_4-thin film formation was confirmed using XRD, where the main peaks in the spectra from the thin films were found to be comparable with those of bulk Zn_2SnO_4 (chapter IV). The calculated grain size, estimated from the XRD spectra was in the range of (20 nm to 25 nm). It was found to be difficult to obtain XRD spectra from films deposited at substrate temperatures of 200°C, this may related to the thickness of the films, which were generally thinner than for films grown at lower temperatures.

Surface structure studies by RHEED indicated that the films were polycrystalline, but with no strong preferred order. The semicircles in the RHEED for films deposited at a substrate temperature of 200°C were both brighter and more spotty in character than those at room temperatures, possibly suggesting that the higher substrate temperatures resulted in a larger grain size.

SEM showed flat and uniform thin films, with no cracks, grains, or second phase being apparent. There was no pinhole formation through the film growth, indicating that the film growth was continuous and uniform. Elemental analysis of the film by EDAX showed peaks due to Zn, and Sn which were nearly identical to those found for bulk samples. This result was taken as a further confirmation (with XRD and RHEED) that the thin films were Zn_2SnO_4.

Conductivity - Temperature characteristics revealed that the conduction mechanism was again variable range hopping, with the conductivity showing the typical $(1/T)^{1/4}$ temerature dependence. This result was supported by Hall coefficient measurements, which gave high carrier concentration (10^{18} cm^{-3}) and low mobilities ($\sim$ 1 cm^2 V^{-1} sec^{-1}), consistent with a hopping mechanism.

Measurements of optical transmission through the thin films as a function of wavelength were carried out. The transmission was increased significantly by increasing the substrate temperature. The high transmissivity of films grown at a substrate temperature of 200°C ($\sim$ 88%) could be useful for transparent electrodes. The change in the shape of the n, and k characteristics suggested that true thin film formation did not take place until the growth temperature reached $\sim$ 150°C. The optical energy gap appeared to be direct in films grown at high substrate temperature, with a value of 1.95 eV. Films grown below this temperature gave a range of values suggesting that the k-values were being affected by scattering. There is nothing reported in the literature relating the type of transition across the band gap for this material.

7.5 - References:

[7.1] - Atkinson A. and Moseley P.T., Appl. Surf. Sci. 65/66, 212-219, (1993).

[7.2] - Nozik A.J., Phys. Rev. **B6**, 453, (1972).

[7.3] - Miyata N.,Miyaki K.,Koga K. and Fukushima T., J. Electrochem. Soc. **127**, 918, (1980).

[7.4] - Minami T., Nanto H. and Tanaka S., Japan. J. Appl. Phys. **23** L280 (1984).

[7.5] - Minami T., Tanaka S., Mouri T. and Ogawa N., Thin Solid Films **193/194**, 721, (1990).

[7.6] - Enoki H., Nakayama T. and Echigoya J., Phys. Stat. Sol. (a)**129**, 181, (1992).

[7.7] - Russell G.J., Prog. Cryst. Growth Charact., **5**, 291 (1983).

[7.8] - Cullity B.D., Elements of X-Ray Diffraction, Wesley, London, (1979).

[7.9] - Van der Pauw L.J., Philips Res.Repts, **13**, 1-9, (1958).

[7.10] - Roberts G. G., Apsley N. and Munn R. W., Phy. Rep., **60**, 59-150, (1980).

[7.11] - Fouad S. S., El-Fazary M.H. and El-Shazly A.A., J. Mater. Sci., **26**, 5843, (1991).

[7.12] - Swanepoel R., J. Phys. E. Sci. Instrum., **16**, 1214, (1983).

[7.13] - Rao D. R. and Islam R., Thin Solid Films, **224**, 191, (1993).

[7.14] - Bihri H., Messaoudi C., Sayah D., Boyer A. and Abd-Lefdil, Phys. Stat. Sol. **(a)129**, 193, (1992).

[7.15] - Sharma K. C., Sharma R. P. and Garg J. C., J. Phys. D: Appl. Phys. **25**, 1019, (1992).

[7.16] - Mullins J. T., Clifton P. A., Brown P. D., Hall D. O. and Brinkman A. W., Mater. Res. Soc. Symp. Proc., **161**, 357, (1990).

CHAPTER VIII

SUMMARY AND SUGGESTIONS FOR FUTURE WORK

The work in this thesis has been principally concerned with the preparation and characterisation of Zn_2SnO_4. The experimental results have included the assessment of structure and the measurement of d.c. and a.c. electrical characteristics, of bulk Zn_2SnO_4 samples, both doped and un-doped, and thin films. The work forms a broad spectrum of research, on which a wide variety of future studies can be based. Of particular interest would be the work with thin films, which has importance for electrochromic displays, and with the development of this material for use as electrodes in secondary cells.

The principal conclusions reached from each of the different parts of this thesis are summarised below :

1 - The formation of monophase Zn_2SnO_4 is strongly dependant on the proportions of ZnO and SnO_2 used and the firing regime. The best molar ratio of these two oxides [8.1,8.2] was found to be $2ZnO:1SnO_2$, while for sintered monophase Zn_2SnO_4 [8.1,8.3,8.4], the optimum sintering temperature range was $1000 < T < 1300°C$. Above this temperature range EDAX revealed that decomposition of the Zn_2SnO_4 took place, while below a temperature of $\sim$ 900°C, the material was not single phase.

The formation of the compound was confirmed by X-ray diffraction, which indicated that the material was monophase in accordance with previous work [8.1,8.3,8.5]. Thermal analysis studies of TG, DTG, and DSC, gave additional evidence to support these conclusions.

The sintering mechanism was thought to be a solid state reaction through an evaporation - recondensation phenomena involving zinc [8.3,8.6]. Detailed EDAX analysis suggested that grain growth was occuring through the evaporation and

subsequent condensation of zinc, as has been suggested by others [8.3].

2 - The as-fired sintered samples were white in colour and electrically insulating ($\sigma = 10^{-9}\ \Omega^{-1}\ cm^{-1}$), but after heating in a reducing atmosphere (at $\sim$ 450°C in 25%H_2 /75%N_2 mixture gas for 14 hours with a heating rate of 10°C min^{-1}), the colour changed to dark grey and the sample became conductive ($\sigma = 10^{-2}\ \Omega^{-1}\ cm^{-1}$).

Thermal analysis studies for typical reduced samples, revealed that reoxidation did not take place until the temperature had reached $\sim$ 600°C, which gives an indication of the stability of the reduction process. Stable characteristics from reduced material should be obtainable up to temperatures of about 500°C. Moreover X-ray diffraction and EDAX studies failed to indicate any changes in the phase of Zn_2SnO_4 as a result of the reduction processes.

3 - D.c. conductivity, Resistance-Temperature (R-T), Hall coefficient, and a.c. impedance measurements were obtained for undoped reduced, and partially reduced samples. These measurements enabled assessment of carrier concentration, carrier mobility and the transport mechanism to be made.

D.c conductivity measurements showed a temperature dependence of conductivity of the form $\exp(To/T)^{1/4}$, indicating that the carrier transport mechanism was probably variable range hopping [8.7]. The carrier concentration was found to be $10^{17}\ cm^{-3}$ and essentially independent of temperature. The mobility was generally low and was found to follow the same temperature dependence, even though measured separately from the conductivity. These last two results from Hall measurements may be taken as additional evidence for the carrier hopping mechanism.

When plotted on the complex plane, the a.c. measurements gave two semicircles, indicating the existence of at least two relaxation times ($\tau_1 = 6 \times 10^{-6}$ sec, $\tau_2 = 3 \times 10^{-5}$ sec). This may be associated with the conduction process, but it was difficult to relate either relaxation time to any particular mechanism, and it was not

possible to separate the effects of grain boundary from hopping as had been hoped. This is clearly one area where more study is required.

4 - Several attempts were made to dope the Zn_2SnO_4 using different procedures and dopants. The methods can be summarised as follows : (i) adding the desired dopant in oxide form directly to the mixture of ZnO and SnO_2 before firing to obtain the Zn_2SnO_4, (ii) adding the desired dopant to previously compounded Zn_2SnO_4 powder and then firing, (iii) doping from the vapour phase by heating Zn_2SnO_4 in the vapour of the dopant, this method was attempted with In only.

The dopant materials used in processes (i) and (ii) were Nb_2O_5, $TaCl_5$, Ta_2O_5, $InCl_3.3H_2O$, and V_2O_5. However, despite extensive trials none of these dopants was effective in reducing the resistivity, although some changes of colour and sintering behavour were observed, as can be seen in table (8.1).

Table (8.1) : General Observations on Doped-Samples Using Mixed Powder Methods.

Dopant material	Conductivity $(\Omega\ cm)^{-1}$ at Room Temperature *	Colour of Sintered Samples	General Observations	Additional Phases
Nb_2O_5	1.14	Dark Grey Spots	Very Hard to Break	$Sn_2Nb_2O_7$
$TaCl_5$	--------	Yellow Powder	Poor Sintering	None
Ta_2O_5	2.95	White	None	None
$InCl_3.3H_2O$	0.04	,,	''	None
V_2O_5	8×10^{-6}	Dark Brown	Liquid Phase Sintering	Un-Identified Phase

* Measured for 1.5 mol% after reduction.

The largest observed change in colour was found in the V_2O_5-doped samples, where SEM observations revealed the presence of some second phase material,

suggesting that liquid phase sintering had occured in these samples, rather than the evaporation -recondensation process thought to occur normally. It was not possible to identify this additional phase, but it may have been the main reason why the resistivity increased with increasing amounts of dopant, the implication being that the second phase resulted in separation of the grains and therefore poor grain-to-grain contact.

The effectiveness of the Nb_2O_5 doping was difficult to assess, as it was impossible to make electrical measurements without some additional reduction process. However, the reduced 0.5% Nb_2O_5 doped-samples were more than one order of magnitude more conductive than the corresponding undoped samples. This can be taken along with the observed colour change, as an indication that Nb had had some effect, though its exact role was not clear. In principle, Nb should act as a conventional substitutional dopant, and the poor efficiancy of Nb doping could be related to the high melting point of Nb_2O_5. As with the V_2O_5 doping the resistance increased with dopant concentration for dopant levels above 0.5% Nb_2O_5, which may again be related to the formation of some second phase ($Sn_2Nb_2O_7$) in the more highly doped material.

Complex impedance measurements revealed the same general pattern as the d.c. conductivity results, with resistivity increasing with doping level above 0.5% Nb_2O_5. The locus of the impedance on the complex plane took the form of two semi-circles i.e. two characteristic relaxation rates, indicating similar behaviour to the undoped material. Interestingly, one of the characteristic frequency was the same as one found for the undoped material. It is tempting to speculate that this freuency may be related to the hopping mechanism, since this is a shared phenomena between doped and un-doped samples

Doping with Indium from the vapour phase achieved a reduction in resistivity, from insulating to about 100 (Ω cm). There was also a colour change, from white to dark grey, but no evidance for any change in the structure or of any new phase was observed. This could be due to the low doping temperature, which the sample was

exposed to (350°C).

Since In-doped samples were confirmed to be n-type, Au/In-Zn_2SnO_4/In.Ga diodes were fabricated and used to provide estimates for the carrier concentration, and depletion width. The diodes were characterised using I-V, and C-V measurements at various temperatures. Since carrier transport was still variable range hopping (from d.c. conductivity measurements) it was not clear to what extent conventional diode analysis was applicable, especially where the ideality factor varied with temperature and gave large values (see table (8.2)), indicating that the normal diode mechanisms were probably not operating.

Analysis of the C-V measurements gave estimates of the depletion widths and net ionised donor densities, which were small, as can be seen from table (8.2). This could be related to the effect of interface states on contact capacitance, which can exercise a controlling influence on the C-V characteristics. Moreover, the complex ploycrystalline structure and the effect of the grain boundaries may be playing a part in this as well.

Table (8.2) : Summary of Au/In-Zn_2SnO_4/In.Ga diode parameters.

I-V			C-V			
T(K)	n	Io(mA)	$C_{v=0}$ F m^{-2}	N_d cm^{-3}	W cm	V_i(V)
77°	15.4	2.5	4.3×10^{-7}	8×10^{13}	4.5×10^{-6}	0.45
300°	4.4	18.3	3.59×10^{-7}	3.6×10^{14}	6.6×10^{-6}	0.21

5 - Zn_2SnO_4 thin films were prepared by electron beam evaporation on cleaned glass and quartz substrates. Film formation was confirmed using RHEED, X-ray diffraction and EDAX. A systematic investigation of the electrical and optical properties of-as grown Zn_2SnO_4 thin films was undertaken as a function of substrate temperature from room temperature to $\sim$ 250°C.

Surface structure by RHEED showed that all the thin films were

polycrystalline, without any preferred order. The grain size increased with substrate temperature, as indicated by the increasing spottiness of the RHEED pattern.

The d.c. conductivity measurements were dependent on the measurement temperature, and displayed a similar exp $(To/T)^{1/4}$ relationship to that found for bulk material. In other words, the carrier transport mechanism was also variable range hopping. The collective results from Hall coefficient and mobility dependence were consistent with variable range hopping [8.7].

The optical studies revealed that the transmission was increased as the substrate temperature increased. Apparent energy gap values varied as substrate temperatures were varied from room temperature to 250°C; 1.45 (at room temperature) eV $\leq$ Eg $\leq$ 1.95 (at 250°C) eV, using direct energy gap analysis.

Future Work :

In order to prepare Zn_2SnO_4 in monophase form by solid state reaction, precise knowledge of the formation and thermal stability of these compounds is essential. To gain this information, further study should be made of the reaction by X-ray diffractometry and thermal analysis. Additional information concerning the zinc stannate can be gained from recently-developed analytical techniques such as ESCA [8.8].

It would be worth investigating the use of hot pressing, since this may control internal voiding in the samples, decreasing the porosity, and possibly enhancing grain growth, with a consequential improvement in contacts between the grains. As a result of this the electrical resistivity would decrease. A further interesting option would be to carry out the hot pressing in vacuum, where the effects of oxidation could be controlled. The use of sintering aids to promote grain growth should also be investigated.

More detailed study of doping should be undertaken specially In-doping from

the vapour phase. This needs to be related more definitively to the observed changes in the colour and the electrical characteristics of the resulting samples. It is important to determine the specific doping molar ratio of indium required to give particular characteristics and to establish the temperature / time relationships for the doping process.

In the case of the thin film work, systematic study is required to clarify the effects of substrate temperature, particularly higher temperatures (which were not available in the present study). The use of more accurate temperature sensors to detect variation in substrate temperature and the use of film thickness monitors to control layer thickness would be a significant improvement.

In conclusion the present study has demonstrated that sintered Zn_2SnO_4 can be produced from the reaction of SnO_2 and ZnO powders. It has shown that the electrical properties of Zn_2SnO_4, can be controlled by the state of oxidation /reduction, and to a lesser extent by doping (particularly with In). The carrier transport properties appear to be limited by variable range hopping between localised states in most cases.

Finally, this work has demonstrate that thin, polycrystalline films of Zn_2SnO_4 can be deposited on glass by the electron beam evaporation of Zn_2SnO_4 powder and that these films are conducting.

References :

[8.1] - Filippova N. A., Savina E. V. and Korosteleva V. A. Russian J., Inorg Chem, Vol.**5**, No.7, 691 (1960).

[8.2] - Hung S., Sumita S., Morinaga K. and Ynagase T, Nippon Kogyo Kaishi, 100(1162), 1145,(1984).

[8.3] - Hashemi T., Al-Allak H.M., Illingsworth J., Brinkman A.W. and Woods J., J. Mater. Sci. Lett., **9**, 776, (1990).

[8.4] - Tylor N. W., Z. Physikal. Chem., **9**, 241, (1930).

[8.5] - Illingsworth J., Hashemi T., Al-Shahrani A. and Brinkman A. W., Brit. Ceram. Proc. 49, Special Ceramics **9**, London, (1990).

[8.6] - Kingery W.D., Bowen H.K. and Uhlmann D.R."Introduction. to Ceramics", John Wiley & Sons, New York, (1976).

[8.7] - Roberts G. G., Apsley N., and Munn R. W., Physics Reports (Review Section of Physics Letters), **60**, 59-150, pp108,(1980).

[8.8] - Golestani-Fard F., Hashemi T.; and Hogarth C. A.; and J. Mater. Sci **18**, 3679, (1983).